
Spatiotemporal Change Detection Based on Persistent Scatterer Interferometry
– A Case Study of Monitoring Urban Area

A thesis accepted by the Faculty of Aerospace Engineering and Geodesy of the
University of Stuttgart in partial fulfilment of the requirements for the degree of
Doctor of Engineering Sciences (Dr.-Ing.)

by

Chia-Hsiang Yang

born in Kaohsiung, Taiwan

main referee: Prof. Dr.-Ing. Uwe Sörgel

co referee: Prof. Dr.-Ing. Xiaoxiang Zhu

Date of defence: 2019.05.10

Institute for Photogrammetry

University of Stuttgart

2019

Abstract

Persistent scatterer interferometry (PSI) detects strong, stable, and coherent radar signals throughout a time series of SAR images. Such persistent signals are reflected from so-called persistent scatterer (PS) points on ground. A set of PS attributes such as temporal coherence, deformation velocity, and topography height can be derived for scene monitoring. In practice, PSI works well on built-up cities because the regular and stationary substructures of buildings ensure high PS density. In case of standard PSI processing, these PS points must maintain presence during the whole acquisition period of a set of SAR images. For this reason, the so-called semi-PS points cannot be identified because they disappeared or emerged during this period due to big changes like construction. We thus regard them as change points.

Based on PSI, we propose a spatiotemporal analysis to detect positions and occurrence times of change points. Our technique first extracts PS points from a SAR image stack. Afterwards, this image stack is divided into several subsets by a series of break dates (an interval between two successive image acquisitions). These image subsets are used as inputs in PSI processing to derive temporal coherence images sorted by time. We introduce change indices calculated from these temporal coherences. A sequence of change indices for each non-PS point quantify its probability of being a change point at different times. Using these change indices, change points are identified by a global, automatic, and statistical-based method. Thereafter, the disappearance or emergence date of each change point is detected from the break dates based on the temporal variation in its change index sequence. Finally, the PS and change points along with the events' dates are integrated for further analysis.

In this study, we use simulated and real data tests to validate and evaluate our approach. The simulation results show that the overall detection accuracy (confusion matrix) of PS and change points is 99% and all of the producer's and user's accuracies are better than 99%. The correlation coefficient of 0.999 between the estimated and reference times indicates a considerably high accuracy for change time detection. Our real data test using TerraSAR-X images successfully recognizes the steady, disappearing, and emerging buildings in Berlin, Germany, within 2013. The spatiotemporal information are consistent with the ground truth. We also discuss monitoring of five study areas of different urban characteristics: intensive constructions, business district, sport facility, traffic infrastructure, and single building. Finally, we compare our technique with two conventional methods to demonstrate the improvement.

Kurzfassung

Persistent Scatterer Interferometry (PSI) nutzt starke, stabile und kohärente Radarsignale für die Auswertung von Zeitreihen in SAR-Bildern. Solche zeitlich stabilen Signale werden durch Reflexionen von sogenannten Persistent Scatterer (PS) Punkten auf der Erdoberfläche erzeugt. Für Monitoringanwendungen kann von diesen PS-Punkten ein Satz von PS-Attributen, z. B. zeitliche Kohärenz, Bewegungsgeschwindigkeit und Topographiehöhe abgeleitet werden. PSI funktioniert gut in bebauten Städten, da die regelmäßigen Strukturen an Gebäuden eine hohe PS-Dichte mit sich bringen. Die PS müssen während der gesamten Akquisitionsperiode von SAR-Bildern vorhanden sein. Auf sogenannte Semi-PS-Punkte trifft dies nicht zu: Diese sind im Allgemeinen nicht nutzbar, da sie während der Beobachtungsperiode aufgrund von großen Änderungen wie Gebäudekonstruktion oder -abriss auftreten oder verschwinden. Solche Punkte werden als Veränderungspunkte bezeichnet.

Basierend auf PSI wird in dieser Arbeit eine raumzeitliche Analyse vorgeschlagen, um die Positionen und Auftretenszeiten von Veränderungspunkten zu ermitteln. Dazu werden zuerst PS-Punkte aus einem SAR-Bildstapel extrahiert. Der Bildstapel wird dann durch einen Satz von Ereignis-Tagen in mehrere Teilmengen unterteilt (ein Intervall zwischen zwei aufeinanderfolgenden Bildaufnahmen). PSI wird sodann auf die Bilduntergruppen angewandt, um eine Reihe zeitlicher Kohärenzbilder abzuleiten. Aus den Kohärenzbildern wiederum werden Änderungsindizes berechnet. Eine Sequenz von Änderungsindizes für jeden Nicht-PS-Punkt quantifiziert die Wahrscheinlichkeit, zu verschiedenen Zeiten ein Änderungspunkt zu sein. Alle Änderungsindizes werden verwendet, um Änderungspunkte durch eine globale, automatische und statistisch basierte Methode zu identifizieren. Aus den Ereignis-Tagen wird danach der Zeitpunkt des Verschwindens oder Auftretens jedes Änderungspunkts erfasst, basierend auf der zeitlichen Variation in seiner Änderungsindexsequenz. Schließlich werden die PS- und die Änderungspunkte zusammen mit den Zeitpunkten der Ereignisse zur weiteren Analyse integriert.

Zur Validierung und Bewertung des Ansatzes werden Tests mit simulierten und realen Daten durchgeführt. Die Simulation zeigt, dass die aus der Konfusionsmatrix ermittelte Gesamtdetektionsgenauigkeit der PS- und der Änderungspunkte 99% beträgt und die Hersteller- sowie Anwender-Genauigkeiten besser als 99% sind. Die Mittelwerte der Zeitpunkte der geschätzten Ereignisse wurden mit den Referenzdaten verglichen. Es ergibt sich ein Korrelationskoeffizient von 0.999, was bedeutet, dass die

vorgestellte Methode Ereignis-Zeitpunkte mit einer sehr hohen Genauigkeit erkennen kann. Beim Test mit realen Daten (TerraSAR-X Bilder von Berlin, Deutschland, 2013) werden erfolgreich vielerlei verschwindende und entstehende Gebäudeteile erkannt. Die ermittelten Zeitpunkte und Positionen der Veränderungen stimmen mit den tatsächlichen Gegebenheiten überein. In der Arbeit werden darüber hinaus auch städtebauliche Anwendungen anhand folgender fünf Beispiele untersucht: (i) Ableiten des Baufortschritts, Entwicklung von (ii) Geschäftsvierteln, (iii) Sportanlagen, (iv) Verkehrsinfrastrukturen sowie (v) einzelner Gebäude. Schließlich demonstriert der Vergleich der vorgestellten Technik mit zwei konventionellen Methoden die Verbesserungen, die durch den neuen Ansatz erzielt werden.

Contents

Abstract.....	2
Kurzfassung	3
Contents	5
1. Introduction.....	7
1.1. Motivation and objective	7
1.2. State of the art of PSI.....	9
1.2.1. Methodology development.....	9
1.2.2. Techniques for urban monitoring	13
1.2.3. Bottom line	14
1.3. State of the art of change detection	14
1.3.1. Common approaches	14
1.3.2. Amplitude-based semi-PS detection.....	15
1.3.3. Bottom line	15
1.4. Summary.....	16
1.5. Dissertation structure	16
2. Fundamentals of SAR interferometry	17
2.1 Development.....	17
2.2 SAR imaging	17
2.3 InSAR and DInSAR	19
2.4 PSI	23
2.5 Semi-PS detection.....	25
3. Methodology.....	26
3.1 Basic concept.....	26
3.2 Single-break-date scheme.....	26
3.3 Change index	29
3.4 Change detection	30
3.5 Limitations.....	32
3.6 Multi-break-date scheme	32
3.7 Spatial error filtering	35
4. Simulated data test	37
4.1 Simulation procedure.....	37
4.2 Simulated data	38
4.3 Accuracy assessment	42
5. Real data test.....	45
5.1 Data.....	45

5.2	PS extraction.....	48
5.3	Single-break-date result.....	51
5.4	Multi-break-date result	54
5.5	Urban applications.....	60
5.6	Optimal selection of temporal coherence threshold	66
5.7	Comparison with ratio change detection	70
5.8	Comparison with amplitude-based semi-PS method.....	72
5.9	Computational requirements.....	73
6.	Conclusions.....	74
6.1	Summaries	74
6.2	Future works	77
	Bibliography	78
	Acknowledgement	89
	List of acronyms	90
	List of symbols.....	91

1. Introduction

1.1. Motivation and objective

The continuous rise in population and economic growth has led to global urbanization along with frequent building changes, i.e., erection and destruction. Monitoring such big changes is important for city management, urban planning, updating of cadastral maps, etc. (Gamba, 2013; Marin et al., 2015). Remote sensing offers a cost-effective mapping of large areas compared with the conventional field surveys. Spaceborne synthetic aperture radar (SAR) sensors provide radar images, which are captured rapidly over vast areas at fine spatiotemporal resolution. For instance, TerraSAR-X operating in Stripmap mode provides a new image of about 3 m resolution over a scene size of $50 \text{ km} \times 30 \text{ km}$ every 11 days. The spatial resolution can be increased up to 20 cm when Staring Spotlight mode operates (Mittermayer et al., 2014). In addition, active SAR sensors are weather independent and have a day-and-night vision ability, which guarantees to acquire images with a high temporal density. These characteristics make SAR suitable for monitoring events.

Many approaches using multi-temporal SAR images have been proposed for urban monitoring. Among them, persistent scatterer interferometry (PSI) (Costantini et al., 2008; Crosetto et al., 2005, 2016; Ferretti et al., 2000, 2001, 2011; Hooper et al., 2004; Kampes, 2006) detects strong, stable, and coherent radar signals from a time series of SAR images. Such persistent signals are reflected from so-called persistent scatterer (PS) points on ground. A set of PS attributes such as temporal coherence, line-of-sight (LoS) velocity (mm/year level), topography height, and geographic position can be derived for various applications. In practice, PSI works well on built-up cities because the preferred rectangular alignment of stationary structures ensures high PS density. In principle, monitoring of urban subsidence and uplift considers local LoS velocity pattern.

In standard PSI processing, the signal sequence of a PS point is modelled to maintain coherence during the entire acquisition period of a SAR image stack. A scene of interest covered with PS points is assumed not to undergo big changes. A typical example is a building composed of PS-like substructures, which remain permanently intact. These local PS points can thus be extracted for further applications. In contrast, if parts of the substructures or even the entire building disappears due to construction,

the corresponding PS points vanish meanwhile in the initial screening of a PSI framework for temporally stable scatterers. We call them semi-PS points, which disappear or emerge due to big changes. In principle, PSI has nothing to do with such large-scale change detection but rather LoS motion.

Some previous works (Ansari et al., 2014; Brcic and Adam, 2013; Ferretti et al., 2003; Novali et al., 2004) aim at detecting semi-PS points by searching for abrupt amplitude changes of pixels along a sequence of SAR images. PS points are supposed to manifest equally high amplitudes over time. Indeed, it is quite common to utilize an amplitude-based threshold like amplitude dispersion (Ferretti et al., 2001) to select PS candidates. These candidates are then refined to extract PS points. However, we might lose PS points of low amplitude and thus also the corresponding semi-PS points if any. We can resort to another technique.

In general, change detection (Bruzzone and Bovolo, 2013; Hussain et al., 2013; Preiss and Stacy, 2006; Rignot and van Zyl, 1993) measures signal variations in multi-temporal SAR images to identify scene changes. Such changes must be sufficiently large and comparable to the image resolution, e.g., collapsed buildings. According to target objects of interest, a variety of signal forms can be chosen, such as coherence, amplitude, backscatter coefficient, radar cross-section, and so on. For example, we can detect flood coverage (Nico et al., 2000) or vegetation expansion (Askne et al., 1997) based on coherence variance. Nevertheless, nuisances such as image noise and irrelevant changes complicate the task and therefore degrade the detection accuracy. We need complementary data and additional pre-/post-processing to improve the accuracy. Such manipulations usually cause side effects. For instance, image noise can be suppressed by low-pass spatial filters if the noise is modelled to be spatially uncorrelated; however, scene details are inevitably blurred.

This dissertation develops a spatiotemporal change detection to detect disappearing and emerging semi-PS points along with their occurrence times. We regard these semi-PS points as change points. The term "spatiotemporal" refers to changes that occur over geographical spaces at different times. This new technique proves able to detect more change points than the amplitude-based semi-PS methods. In addition, the nuisances subject to common change detection are not concerned at all.

1.2. State of the art of PSI

1.2.1. Methodology development

Persistent scatterer interferometry is extended from differential interferometric SAR (DInSAR) that estimates ground displacements over a scene of interest by using two or more SAR images. Two comprehensive reviews of DInSAR can be found in Hanssen (2001) and Massonnet and Feigl (1998). A DInSAR procedure was first proposed by Gabriel et al., (1989), followed by various applications including landslide monitoring (Carnece et al., 1996; García-Davalillo et al., 2014), uplift and subsidence analysis (Amelung et al., 1999; Galloway et al., 1998; Massonnet et al., 1997; Raucoules et al., 2003), glaciology (Goldstein et al., 1993; Rignot et al., 1997), seismology (Dalla Via et al., 2012; Massonnet et al., 1993; Peltzer and Rosen, 1995; Zebker et al., 1994), and volcanology (Antonielli et al., 2014; Massonnet et al., 1995; Massonnet and Sigmundsson, 2000). However, the displacement estimation is often degraded due to coherence loss of signals caused by temporal and geometric decorrelations, errors caused by phase unwrapping, and atmospheric phase screen (APS) (Crosetto et al., 2016). PSI was thus developed in the early 2000s to overcome this drawback.

The research pioneers (Ferretti et al., 2000, 2001) coined their method as permanent scatterers approach, which was patented as PSInSARTM in 2000 by Tele-Rilevamento Europa. This approach aims at detecting and analysing PS points for scene deformation monitoring. The signals of PS points maintain coherence consistently as they are little affected by temporal and geometric decorrelations. This method requires a time series of N SAR images, which are acquired using the same system parameters, i.e., orbit, look angle, polarization, wavelength, etc. After all of the images are precisely co-registered, $N-1$ interferograms between a master image and the other $N-1$ slave ones are computed. The phases of the interferograms are employed in the following procedure. PS candidates are selected from the pixels if their time-series signals are strong above a certain level. Here amplitude-based dispersion index is used for this purpose. A periodogram grid search is applied to the PS candidates to estimate their best-fit deformation velocities and residual topographic errors. The goal of this searching is to maximize the temporal coherences, which are modelled in a cost function. This step is done without phase unwrapping. The phase components of the best-fit estimates are subtracted from the original phases to obtain residual phases. The

residual phases are mainly attributed to noise and APS. The APS phases (only spatially correlated, not temporally) are derived by a low-pass spatial filtering and then removed from the original phases. The refined phases are used to estimate again the PS candidates' deformation velocities and residual topographic errors. Compared with the first estimation, their accuracies are improved because of less APS disturbance. Finally, PS points are extracted from the candidates if their temporal coherences fulfil a specified threshold.

PSInSARTM approach has two major constraints. First, moderate-coherence areas like natural lands usually result in low PS density due to lack of coherent signals. Second, amplitude-based dispersion is not suited to low SNR scenes (often in natural lands) to select PS candidates. These two constraints mentioned above hampers applications to low- and moderate-coherence areas. We can resort to another technique described in the following to improve both density and reliability of PS points in particular for suburban scenes.

The small baseline subset (SBAS) method (Berardino et al., 2002; Lanari et al., 2007) allows several master images to establish their own optimal interferogram sets characterized by small temporal and normal baselines. This so-called small baseline constraint mitigates scene coherence loss caused by temporal and geometric decorrelations. Therefore, more PS points over suburban areas are probably identified compared with PSInSARTM. The interferogram sets are temporally connected by singular value decomposition (SVD) (Golub and Van Loan, 1996). A pixel is selected as a PS point if its ensemble coherence of interferograms fulfils a specified threshold. Afterwards, all of the PS points are spatially connected by Delaunay triangulation to form a PS network. The PS points' phases are unwrapped (Costantini and Rosen, 1999) and interpolated for the remaining non-PS points. Based on the unwrapped phases, a least square algorithm is utilized to evaluate the deformation velocities and residual topographic errors for all pixels. The evaluation accuracy is further improved by iteration after APS removal. For this purpose, the APS phases are derived by means of a low-pass spatial filtering and a high-pass temporal one.

Certain advances in technique and application were achieved in 2003. Schmidt and Bürgmann (2003) introduced a SBAS-like approach for monitoring of uplift and subsidence. Based on small baseline constraint, Mora et al. (2003) sought and used only crucial SAR images in PSI computation to improve the efficiency. Colesanti et al. (2003) adapted PSInSARTM method for seasonal deformation phenomena. Other important literatures are Adam et al. (2003), Crosetto et al. (2003), and Lyons and Sandwell

(2003). The industry community also began to commercialize PSI and SBAS techniques (Duro et al., 2003; Werner et al., 2003).

So far the PS density in low SNR natural terrains was still insufficient for reliable analysis. To overcome this shortcoming, Stanford method for persistent scatterers (StaMPS) (Hooper et al., 2004) brought a phase-based threshold to detect PS points irrespective of SNR. The increase of PS density in suburban areas was proven. In the same year, SBAS experts also improved their method. Formerly, SBAS relied on multi-look operation to improve scene coherence and thus enhance phase unwrapping accuracy. However, this operation causes loss of spatial resolution as well. This disadvantage was addressed by an extended SBAS version (Lanari et al., 2004) where the phase unwrapping was adapted to work on full-resolution SAR images without accuracy degradation.

Afterwards, technical development kept moving forward. Crosetto et al. (2005) divided PSI procedure into two consecutive steps. The first computation only involves parts of SAR images in order to spare processing time. The second step employs the entire images but considers only the subareas of interest, which are subject to notable deformation signals in the first results. This strategy improves the efficiency of PSI processing and analysis. Ferretti et al. (2005) characterized the physical properties of PS points, i.e., backscattering, geometrical features, and corner reflection type. Understanding these properties assists in interpretation of scene deformation. Kampes (2006) proposed a spatiotemporal unwrapping network (STUN), which is able to assess precisions of PS-related estimates. Originally, a minimum cost flow (MCF) phase unwrapping was designed for one single interferogram (Costantini, 1998; Schmidt and Bürgmann, 2003). An extended MCF (EMCF) version was then tailored to be compatible with multi-temporal interferograms for SBAS (Pepe and Lanari, 2006). A 3D phase unwrapping method was developed by Hooper and Zebker (2007) to solve spatiotemporal phase ambiguity. Ferretti et al. (2007) demonstrated how to decompose a LoS deformation velocity to derive the vertical and horizontal components. This method requires at least two PSI results from ascending and descending SAR image stacks to solve rank deficiency. Quasi-PS (QPS) method (Perissin et al., 2007; Perissin and Wang, 2011, 2012) is devoted for PS points of medium coherence, which are usually ignored in a standard PSI processing. Persistent scatterer pairs (PSP) approach estimates relative deformation velocities and topography heights between connected PS points. These estimates are unwrapped to derive the absolute values for each PS point. The final results are insensitive to APS disturbance, which is modelled to be offset between connected points. Stable point network (SPN) (Crosetto et al., 2008) was

proposed to determine a linear deformation velocity and a nonlinear displacement sequence for each PS point. López-Quiroz et al. (2009) and Wegmuller et al. (2010) contributed to monitoring of extraordinarily large deformation.

In the late 2000s, Hooper (2008) and Rocca (2007) emphasized the need to combine PS and distributed scatterers (DS) points to increase the measurement points for comprehensive monitoring. DS points are defined to be a cluster of pixels where reflected radar signals share the same statistics. In general, DS points are found on homogeneous areas of moderate coherence such as non-cultivated vegetation, outcrops, or rocky lands. Ferretti et al. (2011) developed SqueeSARTM (patented by Tele-Rilevamento Europa) to detect and combine PS and DS points in a standard PSI workflow. First of all, PS points are located by PSInSARTM. Then, DS points are identified by a two-sample Kolmogorov-Smirnov test (Kvam and Vidakovic, 2007; Press et al., 1988; Stephens, 1970). The time-series phases of each DS point are refined by phase triangulation algorithm to "squeeze" useful and high-coherence phases. Afterwards, the DS points are treated as and processed with the PS points in a standard PSI computation. The increase of measurement points enhances the PSI applicability to various kinds of land cover.

Recent works are summarized as follows. The improved EMCF phase unwrapping (Fornaro et al., 2011; Pepe et al., 2011, 2015) does not require multi-look operation and thus prevents loss of detail. Goel and Adam (2014) and Wang et al. (2012) contributed to detect DS points in a more efficient way. Multiscale interferometric SAR time series (MInTS) (Hetland et al., 2012) features its flexible usage of various deformation models including linear, nonlinear, logarithmic, exponential, sinusoidal, B-spline motions, etc. Lv et al. (2014) extracted DS points, whose phases can be correctly retrieved even from SAR images of poor co-registration accuracy. Zhang et al. (2014) integrated different deformation models characterized by linearity, acceleration, periodicity, etc., to investigate complex deformation scenarios. Morishita and Hanssen (2015) combined SAR images, which are acquired from multiple radar sensors, in a single PSI processing. The major contribution is a refined deformation model, which integrates radar signals of different wavelengths and look angles. Chang and Hanssen (2016) introduced multiple hypothesis testing (Koch, 1999; Teunissen, 2000) in PSI to optimize parameter solution and enable reliability assessment. Unlike SqueeSARTM, a single DS point detected by Cao et al. (2016) is modelled to be dominated by multiple scattering mechanisms instead of only one. This new modelling leads to increase of DS density. Esmaeili and Motagh (2016) merged dual-polarized SAR signals to be used in PSI. The benefit of a proper merging in a proper way is to increase the signal coherences.

1.2.2. Techniques for urban monitoring

In particular, PSI works well for urban areas where dense PS points are likely formed on steady buildings due to multi-bounce corner reflection. For example, an urban PS density detected from a stack of high-resolution TerraSAR-X images can be greater than 100000 points/km² (Gernhardt et al., 2010). Nevertheless, monitoring structural details was constrained in the early days because only low- or moderate-resolution SAR images such as Radarsat-1/2 and Envisat were available. This constraint has been overcome by the second-generation SAR systems such as TerraSAR-X and COSMO-SkyMed (Bamler et al., 2009; Sansosti et al., 2014). They were launched since 2008 and are able to provide metre-resolution images. For instance, the azimuth and slant-range resolutions of a TerraSAR-X image are up to 0.2 and 0.6 m given use of Staring Spotlight mode (Mittermayer et al., 2014). Meanwhile, high spatial resolution also assists with increase of PS density. Bonano et al. (2013) demonstrated that the PS densities from the Radarsat-1 and Envisat images to the COSMO-SkyMed images are increased by 320% and 550%. Besides, the updated georeferencing system enables accurate 3D geocoding of PS points. The geocoding accuracy of TerraSAR-X images can be better than 1 m (Gernhardt et al., 2015; Gisinger et al., 2015). In summary, the advanced SAR systems benefit PSI performance especially for urban applications.

We summarize important studies with respect to urban applications of high-resolution SAR images. Gernhardt et al. (2010) analysed the factors in determining PS density on buildings. These factors include polarization, look angle, and spatiotemporal resolution of SAR signals as well as geometric features of buildings. This research helps people to select adequate parameters to make PS density as high as possible. Monserrat et al. (2011) investigated thermal expansions of PS points to interpret structural deformation caused by temperature variation. A similar work was later done by Crosetto et al. (2015). Gernhardt and Bamler (2012) demonstrated how to evaluate building deformation by using high-resolution SAR images. The geometric characteristics of PS points on facades was discussed in Gernhardt et al. (2015), Schack and Soergel (2014), and Schunert and Soergel (2012). The aim is to take advantage of PS geometry to improve PSI accuracy or translate deformation values into semantic information. Ma and Lin (2016) devise a way to identify PS points subject to double dominant scatterers. This method is suited for built-up environments where double dominant scattering is often caused by layover distortion. The work conducted by Schunert and Soergel (2016) fits PS points to a 3D building model, which facilitates geometric interpretation of structural deformation. Huang et al. (2017) evaluated the thermal expansion of a high-

speed railway bridge using Sentinel-1 images.

1.2.3. Bottom line

PSI is a mature technology capable of providing qualitative and quantitative (at millimetre or even sub-millimetre level) deformation estimation for large-scale scenes or small objects. This technology suits monitoring of urban areas in particular when high-resolution SAR images are used. So far most of the researches have been devoted to improving PS density and estimation accuracy and to adapting deformation models for various applications. These methodological improvements mainly benefit from the advancements of radar systems and algorithms.

PSI relies on PS points, which always exist and provide coherent signals during a whole acquisition period of SAR images. Given occurrence of big changes, the coherent signals are interrupted and no longer PS points. Consequently, these affected points are not present in the PSI result. However, there are no clues to the causes, i.e., change events. We must resort to other approaches for change detection.

1.3. State of the art of change detection

1.3.1. Common approaches

Change detection using multi-temporal SAR images (Bruzzone and Bovolo, 2013; Hussain et al., 2013; Rignot and van Zyl, 1993) is widely used to recognize big changes. The methodological categories contain direct comparison (Hall and Hay, 2003; Rignot and van Zyl, 1993), coherent and incoherent methods (Preiss and Stacy, 2006), supervised analysis (Balz and Liao, 2010; Dong et al., 2011; Ehrlich et al., 2009), unsupervised analysis (Bazi et al., 2005; Brett and Guida, 2013; Dekker, 2011; Matsuoka and Yamazaki, 2004), classification (Bruzzone et al., 2004; Gong et al., 2017), GIS application (Dell'Acqua et al., 2011), time-frequency analysis (Bovolo and Bruzzone, 2005), joint use of SAR and complementary data (Brunner et al., 2010; Chini et al., 2009; Poulain et al., 2011; Tao et al., 2012; Taubenböck et al., 2012), and so on.

Whichever methods are employed, there are four considerations to achieve accurate and reliable results. First, ground changes of interest are mixed with speckle and noise in SAR images. Second, side-looking imaging of SAR systems causes image distortions (foreshortening, layover, and shadowing), which are particularly problematic in built-

up areas (Dong et al., 1997; Franceschetti et al., 2002; Soergel et al., 2005, 2006; Stilla et al., 2003). Third, geometric and radiometric characteristics of ground objects are diverse depending on signal parameters (wavelength, polarization, look angle, etc.), scene environments (topography, land cover, corner reflection, etc.), and object properties (dielectric constant, surface roughness, etc.) (Xia and Henderson, 1997). Fourth, high-resolution images are more heterogeneous than moderate- and low-resolution ones (Brenner and Roessing, 2008; Soergel et al., 2006). For example, a single building is regarded as a pure object in a moderate-resolution image. In contrast, the substructures like facades and roofs are independently treated as small objects given use of a high-resolution image. On the one hand, the changes of small objects can be detected; on the other hand, the task becomes more difficult and requires new and adequate methods. All of these considerations make change detection complicated and vulnerable in particular for urban areas. To solve these problems, we rather turn to another technique explained in the next section.

1.3.2. Amplitude-based semi-PS detection

We regard amplitude-based semi-PS detection (Ansari et al., 2014; Brcic and Adam, 2013; Ferretti et al., 2003; Novali et al., 2004) as one category of change detection. The concept of semi-PS points was first introduced by Ferretti et al. (2003). This method looks for abrupt amplitude changes of pixels in a SAR image stack to recognize semi-PS points. For instance, building constructions can be detected in cities without consideration for speckle, noise, and irrelevant changes (e.g., water or vegetation). Bayesian step detector (Ó Ruanaidh and Fitzgerald, 1996) or Normality test can be utilized for this purpose. Brcic and Adam (2013) compared other common change point detectors, i.e., ratio edge detector (Touzi et al., 1988), exponential maximum likelihood estimation (MLE), rice MLE, and Gaussian MLE. These detectors perform similarly in practice. Further applications and discussions were later conducted by Ansari et al. (2014) and Novali et al. (2004).

1.3.3. Bottom line

So far we have introduced common change detection and amplitude-based semi-PS detection. The performance of common change detection is limited due to complex processing and analysis of SAR images. Amplitude-based semi-PS detection is dedicated to identifying disappearance or emergence of PS points. This technique suits especially monitoring of building changes in urban areas. However, semi-PS points of low amplitude are likely missed considering that PS points are assumed to manifest

high amplitudes. To overcome this drawback, we propose a novel technique to detect sort of semi-PS points based on temporal phase stability rather than amplitude stability.

1.4. Summary

In this dissertation, the proposed PSI-based change detection aims to identify disappearing and emerging semi-PS points along with their occurrence times. We distinguish and label these two kinds of points as disappearing big change (DBC) and emerging big change (EBC) points. The key idea of our approach is to derive a change index sequence for each pixel from its temporal coherence estimates spanning different periods. Temporal coherence is modelled to be proportional to phase stability and serves as an indicator of a PS point. Change points are then identified by statistical analysis of their change indices. Finally, we analyse the evolution of change indices to detect the occurrence time of a change point. In practice, this technique is suitable to monitor built-up areas covered with intensive PS-like structures. The concept is simple and portable because only temporal coherence images are needed instead of developing a specialized approach from scratch.

1.5. Dissertation structure

This dissertation is organized as follows. Section 2 illustrates fundamentals of SAR interferometry: brief of development, SAR imaging, interferometric SAR (InSAR), DInSAR, and PSI. The proposed methodology is described in detail in Section 3. By using simulated data, we validate and assess our approach in Section 4. Our real data test (Section 5) is to detect the disappearing and emerging buildings as well as their occurrence times in the Berlin's city centre. In addition, some examples with respect to urban applications are discussed. We also compare our method with the conventional ratio change detection and the amplitude-based semi-PS approach. Finally, the conclusions and future works are summarized in Section 6.

2. Fundamentals of SAR interferometry

2.1 Development

Radar is an acronym for radio detection and ranging. Principle of radar operation is to emit electromagnetic signals in the microwave domain and then receive the return signals backscattered from target objects. The range between radar and target object can be approximated from the two-way travel time of each signal. The intensities of the return signals regard the physical properties, e.g., material and roughness, on the object surfaces. The first radar system (Hülsmeier, 1904) was developed in 1903 for ship tracking and collision avoidance. The military needs promoted the radar development in the 1930s and 1940s (Curlander and McDonough, 1991). Since the beginning of 1950s, an imaging radar system called side-looking radar (SLR) has been operational. This system is able to distinguish adjacent backscattering sources, i.e., image resolution. In addition, the active sensors mounted on airplanes or satellites are capable of day-and-night vision regardless of weather conditions. This advantage guarantees high temporal density of image acquisition. Initially, an imaging radar was called real aperture radar (RAR), in which due to diffraction the azimuth resolution is inversely proportional to the antenna length. In principle, a longer antenna results in a finer azimuth resolution. However, the restriction on an antenna length restrains improvement of azimuth resolution at reasonable costs. This limitation hampers in-depth scene investigation. Compared with RAR, SAR, which was later developed, improves its azimuth resolution in a cost-effective manner. A long virtual antenna is synthesized from successive radar signals received by a moving antenna. Another system advancement of SAR is that the signals maintain coherence during transmission. Phases can hence be utilized in SAR interferometry (Bamler and Hartl, 1998; Gens and Van Genderen, 1996; Hanssen, 2001; Massonnet and Feigl, 1998; Rosen et al., 2000) for mapping and monitoring. Among them, InSAR and DInSAR are devoted to topography reconstruction and monitoring of ground displacement, respectively. The performance of DInSAR can be further improved by an extended technique called PSI.

2.2 SAR imaging

Figure 1 illustrates how a scene of interest is imaged by a side-looking SAR. The two-way travel times of the received signals backscattered from ground objects determine their slant-range positions, i.e., the signals received earlier are imaged closer

to the antenna. However, such side-looking imaging causes geometric distortions (Schreier, 1993), i.e., foreshortening, layover, and shadow. On the one hand, these distortions make image analysis complicated particularly in built-up areas; on the other hand, they also pertain to building geometry in 3D modelling (Soergel, 2010). Integrating the 1D slant-range data along the azimuth direction forms a 2D SAR image (azimuth, slant-range). The azimuth resolution

$$\rho_a = \frac{L_a}{2} \quad (1)$$

depends on the antenna length L_a . The slant-range resolution is formulated as

$$\rho_{sr} = \frac{c \cdot \tau}{2} \quad (2)$$

where c is the speed of light and τ is the pulse duration of a SAR signal. The slant-range resolution is a constant but varies when it is projected onto the ground range. For a flat scene, a ground-range resolution

$$\rho_{gr} = \frac{c \cdot \tau}{2 \cdot \sin \theta} \quad (3)$$

varies with the look angle θ , i.e., towards the nadir it becomes coarser and finally loses discrimination. For this reason, SAR imaging must operate under oblique view.

The SAR signal of each image pixel can be expressed as a complex value

$$s = I \cdot e^{j\phi} \quad (4)$$

which consists of intensity I and phase ϕ . The intensity is mainly determined by geometry, roughness and dielectric constant on ground surface. An intensity image is characterized by bright and dark speckles, which are caused by constructive and destructive interferences of returned signals from independent and random distributed sub-scatterers. The speckle effect leads to granular patterns and so complicates image processing, interpretation, and analysis. Many filters can be used to suppress speckle for further applications (Lee, 1981a; Lee et al., 1994; Porcello et al., 1976). The phase measures the range between an antenna and an object. However, we cannot obtain absolute phases directly from SAR processor; instead, wrapped phases subject to

modulo 2π (Ghiglia and Pritt, 1998; Goldstein et al., 1988; Judge and Bryanston-Cross, 1994; Zebker and Lu, 1998). The phases that follow a uniform distribution are usually ignored in case of single image analysis. In contrast, the phase differences between two or more SAR images provide useful information for InSAR and DInSAR.

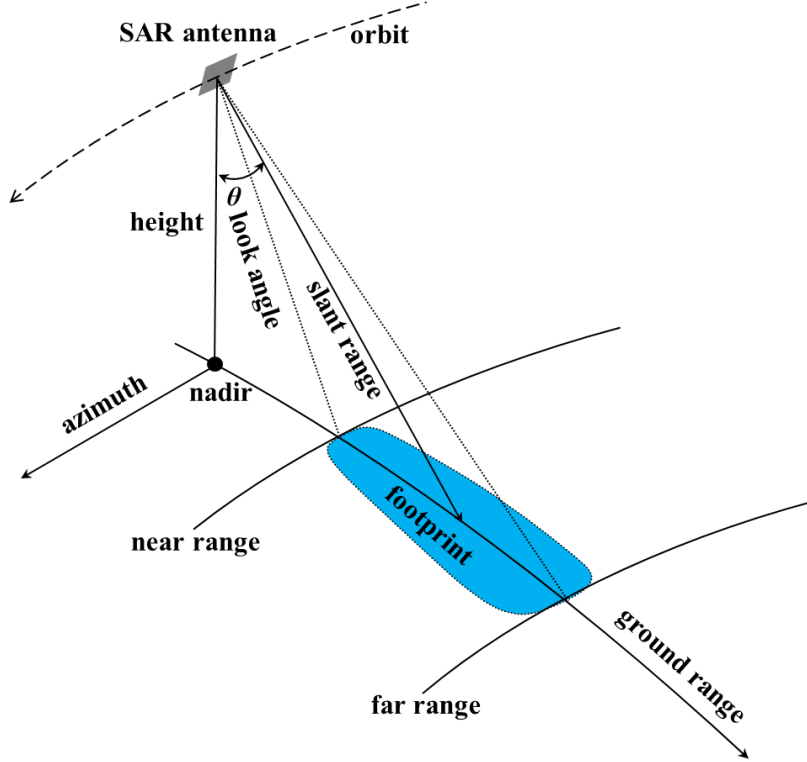


Figure 1: Side-looking SAR. SAR antenna orbits along azimuth axis perpendicular to ground range axis. A sequence of emitted SAR signals illuminates footprint along ground range axis from near to far range. Line of sight is defined as slant-range axis. Look angle is included between antenna-to-nadir and slant-range axis. (This figure is modified from SAR-EDU: <https://saredu.dlr.de/>)

2.3 InSAR and DInSAR

In theory, we can derive an object's height from a single SAR signal based on trigonometry. As shown in Figure 2, considering only the master antenna, the heights of object a and b can be computed geometrically by

$$H_a = H_m - R \cdot \cos \theta_a \quad (5)$$

$$H_b = H_m - R \cdot \cos \theta_b \quad (6)$$

However, this geometric approach is not practical because of three limitations. First, the SAR sensor is incapable of exactly measuring look angles θ_a and θ_b . Second, the

slant-range R can be measured based on the two-way travel time of the SAR signal. The required accuracy is millimetre level. However, the accuracy is degraded due to atmospheric interference and imprecise timing. In addition, the slant-range resolution is normally three orders of magnitude worse than millimetre (Hanssen, 2001). Last but not least, SAR imaging is unable to discriminate objects at the same slant-range like objects a and b.

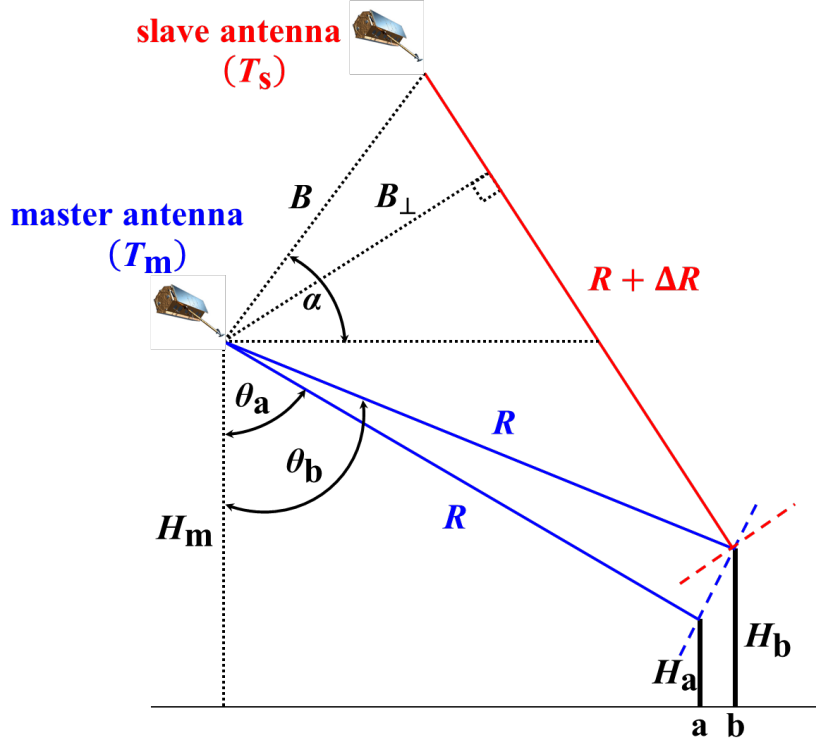


Figure 2: Repeat-pass InSAR. Master and slave antennas operate at times T_m and T_s whose interval $B_T = T_m - T_s$ is called temporal baseline. Master antenna receives signals reflected from objects a and b at the same slant-range R but with different look angles θ_a and θ_b . Slave antenna receives signal reflected from object b at slant-range $R + \Delta R$. Spatial distance of master and slave antennas is defined as spatial baseline B . α is tilt angle between spatial baseline and horizontal. Component of spatial baseline perpendicular to line of sight of slave antenna is called perpendicular baseline $B_{\perp} = B \cdot \cos(\theta_b - \alpha)$. H_m , H_a , and H_b are heights of master antenna, object a, and object b. (This figure is modified from Hanssen (2001))

Repeat-pass InSAR (Zebker and Goldstein, 1986) (Figure 2) utilizes the interferometric signals from the master and slave antennas to determine the objects' heights with a considerably high accuracy compared with the trigonometry method. First of all, the master and slave images are precisely co-registered with sub-pixel accuracy or better (Hanssen, 2001). Multiplying the master image by the conjugate slave image obtains an interferogram. Given object b, the interferometric signal is

expressed as

$$s_b^{int} = s_m \cdot s_s^* = (I_m \cdot I_s) \cdot e^{j(\phi_m - \phi_s)} = I_b \cdot e^{j\phi_b} \quad (7)$$

where s_m and s_s are the master and slave SAR signals. The complex coherence of s_b^{int} is defined as (Bamler and Hartl, 1998)

$$\gamma = \frac{E[s_m \cdot s_s^*]}{\sqrt{E[|s_m|^2] \cdot E[|s_s|^2]}}. \quad (8)$$

The magnitude $|\gamma| [0, 1] \in \mathbb{R}$, customarily called coherence, can be expressed as a function of SNR (Zebker and Villasenor, 1992)

$$|\gamma| \cong \frac{\text{SNR}}{\text{SNR} + 1} \quad (9)$$

which is established for signals of high SNR contaminated by only thermal noise. In principle, high-coherence interferometric signals are a prerequisite for accurate InSAR results. The noise floors of the interferometric signals are assumed to be the same for all acquisitions. Also the signal powers are always large to assure high SNR and so high coherence. Suppose that the interferometric phase ϕ_b and slant-range difference ΔR are subject to the spatial baseline B , their transformation can be expressed as

$$\phi_b = \frac{4\pi}{\lambda} \cdot \Delta R = \frac{4\pi}{\lambda} \cdot [B \cdot \sin(\theta_b - \alpha)] \quad (10)$$

where λ indicates the signal wavelength. Based on law of cosines, the geometric relationship between B , R , and ΔR is formulated as

$$(R + \Delta R)^2 = R^2 + B^2 - 2 \cdot R \cdot B \cdot \cos(90^\circ - \theta_b + \alpha). \quad (11)$$

By combining and reformulating (6), (10), and (11), we derive the equation between the height of object b (H_b) and interferometric phase ϕ_b as

$$H_b = \frac{\lambda \cdot R \cdot \sin \theta_b}{4\pi \cdot B_\perp} \cdot \phi_b \quad (12)$$

whereby H_b can be calculated given that ϕ_b is correctly unwrapped. A large

perpendicular baseline B_{\perp} seems preferable to achieve a fine height resolution as a certain height can be represented by a large range of interferometric phases. On the other hand, the coherence becomes lower because the overlap of signal spectra is decreased, i.e., geometric decorrelation. The coherence loss results in degradation of H_b . The upper limit of perpendicular baseline is called critical baseline (Bamler and Hartl, 1998) expressed as

$$B_c = \frac{\lambda \cdot R \cdot \tan \theta_b}{2 \cdot \rho_{sr}}. \quad (13)$$

An interferogram subject to critical baseline is completely decorrelated and contains only noise.

InSAR assumes that the ground surface of interest is stationary between two acquisition dates of SAR images. This means, the interferometric phases are caused only by topography if the phase noise is not considered. In case ground motions occur, the motion-induced phases are added to the interferometric phases. In this situation, the slant-range difference ΔR (10) stems from both topography and motion. We resort to DInSAR for motion monitoring. For this purpose, topographic phases are first subtracted from interferometric phases to obtain differential interferometric phases. The topographic phases can be derived from either a DEM (digital elevation model) or an InSAR result. According to (10), the differential interferometric phase of object b (Figure 2) can be expressed as

$$\varphi'_b = \frac{4\pi}{\lambda} \cdot \Delta R' \quad (14)$$

where LoS motion $\Delta R'$ is computed as long as φ'_b is correctly unwrapped. The motion sensitivity mainly depends on the signal wavelength λ . In principle, short wavelength is adequate to detect small motions; however, it is also sensitive to APS and therefore leads to phase disturbance.

Thus far, we assume that only topography and motion effects are contained in interferometric phases for InSAR and DInSAR. In more detail, an interferometric phase can be modelled as

$$\varphi = \varphi_{\text{topo}} + \varphi_{\text{mot}} + \varphi_{\text{fE}} + \varphi_{\text{orb}} + \varphi_{\text{APS}} + \varphi_{\text{decor}} + \varphi_{\text{ther}} + \varphi_{\text{proc}} \quad (15)$$

where the topographic and motion phases are denoted by φ_{topo} and φ_{mot} , the flat Earth phase φ_{fE} is caused by the ground range (Figure 1), φ_{orb} is related to inaccuracy of orbital parameters, φ_{APS} represents APS disturbance, φ_{decor} means phase biases due to temporal and geometric decorrelations, the thermal noise φ_{ther} stems from thermal agitation of electrons inside a radar system, and the last component, φ_{proc} , is attributed to imperfect image processing, including co-registration, resampling, and interpolation. The phases φ_{fE} , φ_{orb} , φ_{APS} , φ_{decor} , φ_{ther} , and φ_{proc} are treated as noise (generally assessed by coherence (8)) in InSAR and DInSAR. The phase noise can be diminished by proper signal processing and filtering (Hanssen, 2001). Among them, φ_{APS} and φ_{decor} are particularly difficult to model and filter out because APS disturbance and temporal decorrelation vary arbitrarily in time and space. To overcome this drawback, Ferretti et al. (2000, 2001) developed PSI to detect and analyse only PS points, which are less affected by phase noise and permanently maintain coherence.

2.4 PSI

A time series of N SAR images acquired using the same system parameters is a prerequisite for PSI. At first, a set of PS candidates are selected if their amplitudes are high enough to pass some threshold, e.g., amplitude dispersion (Ferretti et al., 2001)

$$D_A = \frac{\sigma_A}{\mu_A} \quad (16)$$

where μ_A and σ_A are mean and standard deviation of amplitudes. This concept is widely used (Adam et al., 2003; Crosetto et al., 2003; Lyons and Sandwell, 2003; Werner et al., 2003) as PS points usually appear to be high amplitude signals. Nevertheless, those potential PS points of low amplitude or SNR might be lost. To avoid such loss, we estimate phase stability for PS selection, i.e., temporal coherence described in the following.

$N-1$ interferograms are generated based on a master image among others. This image is optimally chosen under small baseline constraint (Berardino et al., 2002; Lanari et al., 2004) to diminish temporal and geometric decorrelations. The differential interferometric phases can be modelled as

$$\varphi^{\text{int}}(x) = \varphi_{\text{res_topo}}^{\text{int}}(x) + \varphi_{\text{mot}}^{\text{int}}(x) + \varphi_{\text{APS}}^{\text{int}}(x) + \varphi_{\text{noise}}^{\text{int}}(x) \quad (17)$$

where x denotes the pixels in the interferograms indexed by $\text{int} [1, N-1] \in \mathbb{N}$ and

$\varphi_{\text{res_topo}}^{\text{int}}$ regards residual topographic errors Δh remained after subtraction of topographic phases. $\varphi_{\text{res_topo}}^{\text{int}}$ is formulated as

$$\varphi_{\text{res_topo}}^{\text{int}}(x) = \frac{4\pi \cdot B_{\perp}^{\text{int}}}{\lambda \cdot R(x) \cdot \sin[\theta(x)]} \cdot \Delta h(x). \quad (18)$$

The motion phase $\varphi_{\text{mot}}^{\text{int}}$ is expressed as

$$\varphi_{\text{mot}}^{\text{int}}(x) = \frac{4\pi}{\lambda} \cdot B_{\text{T}}^{\text{int}} \cdot v(x) \quad (19)$$

where v indicates LoS velocity. Both Δh and v are the two unknowns to be solved for each pixel. Their optimal estimates, $\hat{\Delta h}$ and \hat{v} , are determined by the periodogram searching (Ferretti et al., 2001)

$$\underset{\Delta h(x) \& v(x)}{\operatorname{argmax}} \left\{ \gamma_{\text{T}}(x) = \left| \frac{1}{N-1} \cdot \sum_{\text{int}=1}^{N-1} \exp j[\varphi_{\text{o}}^{\text{int}}(x) - \varphi^{\text{int}}(x)] \right| \right\} \quad (20)$$

where γ_{T} is defined as temporal coherence and $\varphi_{\text{o}}^{\text{int}}$ indicates the differential interferometric phases in the interferograms. However, the APS phases in $\varphi_{\text{o}}^{\text{int}}$ degrade the estimates and must be excluded in the second searching to improve the precision. After the first searching, the residual phases calculated as

$$\varphi_{\text{res}}^{\text{int}}(x) = \varphi_{\text{o}}^{\text{int}}(x) - \hat{\varphi}_{\text{res_topo}}^{\text{int}}(x) - \hat{\varphi}_{\text{mot}}^{\text{int}}(x) \quad (21)$$

are mainly composed of APS phases $\varphi_{\text{APS}}^{\text{int}}$ and noise $\varphi_{\text{noise}}^{\text{int}}$. A spatiotemporal filtering (Ferretti et al., 2000, 2011) is applied to $\varphi_{\text{res}}^{\text{int}}$ to derive the APS phases $\hat{\varphi}_{\text{APS}}^{\text{int}}$, which are modelled to be spatially correlated but temporally uncorrelated. The periodogram searching is iterated after subtracting $\hat{\varphi}_{\text{APS}}^{\text{int}}$ from $\varphi_{\text{o}}^{\text{int}}$. As a result, the estimates' precisions and temporal coherences should be improved; if not, the whole procedure must be exhaustively checked to find and solve the problems. For instance, the searching ranges of unknowns Δh and v can be adjusted to seek a better fit. This requires prior knowledge and operators' experience. Another alternative is to apply a stronger filtering to filter out more APS phases; however, we risk losing also the phases related to Δh and v .

Generally, the coherence estimates in interferometry tend towards the optimistic side in case of low number of samples (i.e., N) and low true coherences (Bamler and Hartl, 1998; Touzi et al., 1999). Conventionally, for medium-resolution SAR sensors like ERS or Envisat a minimum stack of 15 images is considered a prerequisite for PSI (Crosetto et al., 2016). For high-resolution sensors even less images are sufficient (Bovenga et al., 2012). We later use a least 12 TerraSAR-X images in the PSI processing for an urban scene and a rather high threshold of temporal coherence to select PS points.

Finally, pixels are selected as PS points if their temporal coherences fulfil a specified threshold while the unselected pixels are discarded. However, these discarded pixels might include change points, which cannot be detected at this stage by PSI. An alternative approach can be used for retrieval of such change points.

2.5 Semi-PS detection

Ferretti et al. (2003) first mentioned the concept of semi-PS points, which behave as PS either before or after some change event. The PS points are assumed to be characterized by consistently high amplitudes subject to Gaussian distribution. Given a SAR image stack, this method looks for abrupt amplitude changes of pixels to identify semi-PS points. The amplitude is calculated from (4) as

$$A = \sqrt{I}. \quad (22)$$

Here amplitude is used rather than intensity because the second's value range is too large and so hampers the analysis. Another reason is that amplitude phase dispersion can be utilized later to test whether semi-PS points existed as PS points during a specific time period. Bayesian step detector (Ó Ruanaidh and Fitzgerald, 1996) is applied to the amplitude sequence of each pixel to locate its abrupt amplitude change, if any. Alternatively, we can utilize normality test to seek for semi-PS points. We assume that their amplitudes conform to Gaussian when they act as PS either before or after a change event. Nevertheless, some semi-PS points of low amplitude do not fulfil the assumptions mentioned above and so are missed in this approach. To overcome this shortcoming, we can now turn to our novel methodology described in the next section.

3. Methodology

3.1 Basic concept

Our spatiotemporal change detection approach is inspired and extended from PSI. This technique is able to identify DBC and EBC points, which are regarded as big changes on ground, along with their occurrence times. To begin with, multi-temporal SAR images are divided into several subsets by a sequence of break dates (an interval between two successive image acquisitions). We want to detect the change events, which takes place during these break dates. The temporal coherence of each pixel in each image set is estimated in a standard PSI processing. The change events must cause variation of temporal coherences over time. Simply speaking, when the time is passing forward, a disappearance or emergence event leads to decrease or increase of temporal coherences, respectively. The key idea is to derive a change index sequence for each pixel from its temporal coherence estimates spanning different periods. These change indices quantify probabilities of change events subject to a break date. The higher the change indices are, the more likely there are changes occurring. Change points are extracted by statistical analysis on the change indices. We then eliminate the blunders by spatial filters, which are designed based on spatial characteristics between change points. This step is crucial for a spatiotemporal analysis. Finally, for each change point we check the evolution of its change index sequence to identify the occurrence date.

3.2 Single-break-date scheme

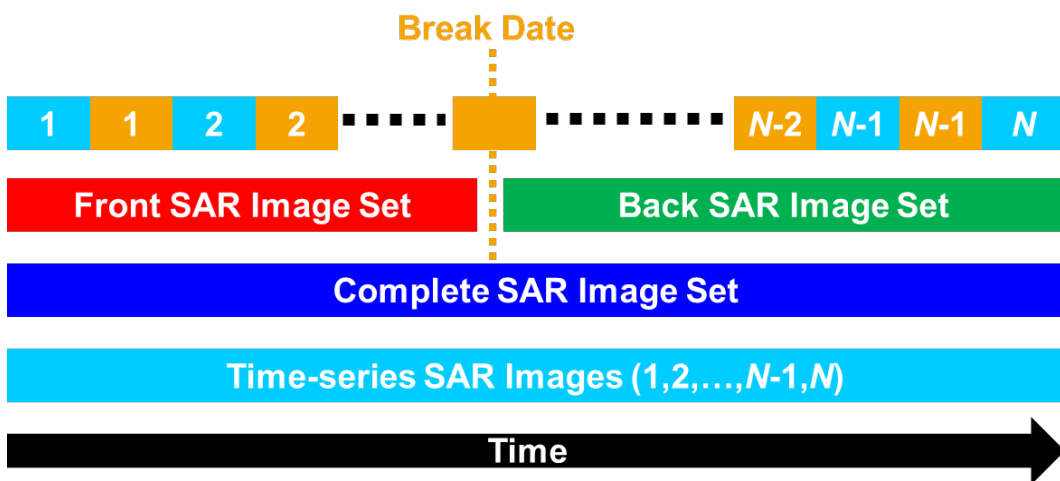


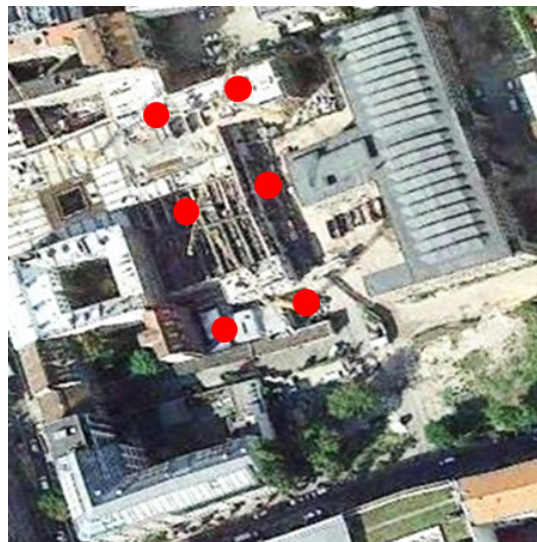
Figure 3: Three sets of time-series SAR images.

We first explain how to detect change points, which emerge or disappear somewhere close to or after a single break date. A break date is set to divide a complete SAR image set into a front and a back sets (Figure 3). The complete set consists of all of the images, from which PS points can be detected but change points are missed. The front and back sets comprise the images taken before and after the break date, respectively. We extract additional information from these two image set to retrieve the change points. The basic idea is to find change points that exist as PS points in the front set but disappear in the back set and vice versa (emergence).



(a)

(b)



(c)

Figure 4: Example to detect disappearing buildings, i.e., DBC points. PS points (blue) detected (a) before and (b) after construction. (c) DBC points (red) extracted by comparison between PS points (a) and (b).

We exemplify the basic idea to detect a construction event (Figure 4), in which some buildings were levelled down at a specific time. Normally, all of the available SAR images during a time period are involved in PSI to identify PS points for scene monitoring. When the image acquisition spans across the construction event, a PSI computation is able to recognize many PS points on the steady buildings but not at the construction site (Figure 4(b)). Our method first sets a break date, which is supposedly prior to the construction. We begin another PSI computation using only the images taken before the break date. The result contains also the PS points at the coming construction site (Figure 4(a)). Finally, these two PSI results are compared to locate the DBC points (Figure 4(c)), i.e., the construction event.

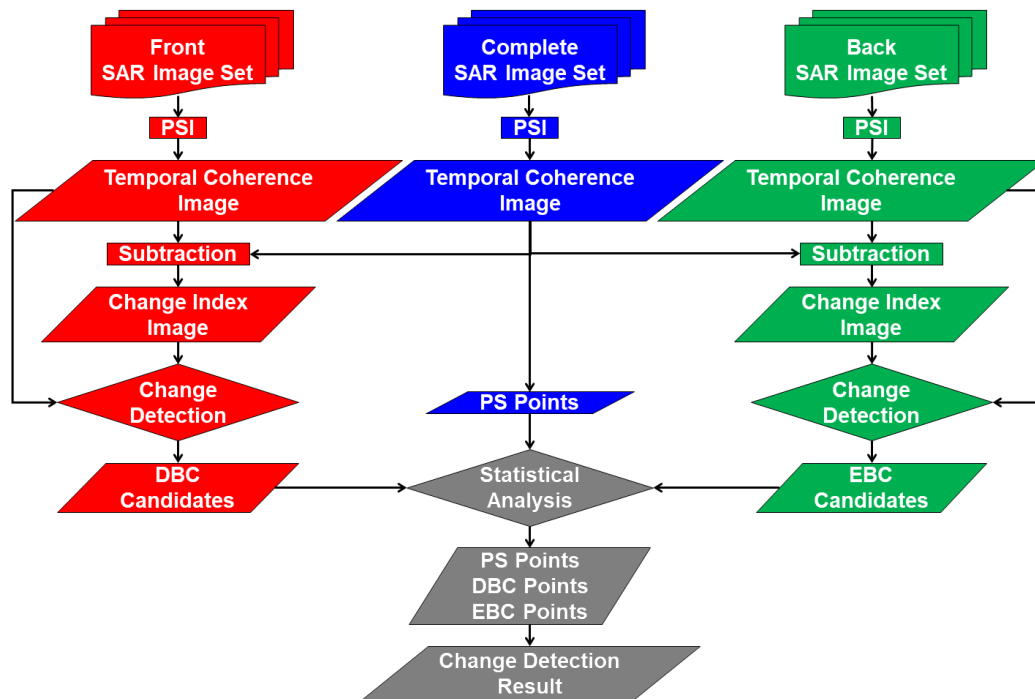


Figure 5: Flowchart of single-break-date change detection scheme. Persistence (blue), disappearance (red), and emergence (green) scenarios are dedicated to extracting PS, DBC, and EBC points.

The flowchart (Figure 5) constitutes the persistence, disappearance, and emergence scenarios, in which the complete, front, and back SAR image sets are involved in detecting PS, DBC, and EBC points, respectively. The three image sets are processed by a standard PSI procedure to generate three temporal coherence images. Pixels are selected as PS points if their temporal coherences of the complete set fulfil a specific threshold. The temporal coherence image of the complete set is then subtracted from those of the front and back sets to obtain two change index images. The change indices in the disappearance scenario reflects how likely objects disappear. The points,

which satisfies PS condition in the front set, are selected as change candidates. These candidates either remain as PS points or disappear to be DBC points. We then separate these two point types by statistically analysing their change indices. A similar process is also used to detect EBC points. Those points, which pertain to both change labels, are regarded as errors and so discarded in this step. The remaining pixels without any label are labelled as void points. Finally, the PS and change points are combined for further analysis.

3.3 Change index

We assume that the temporal coherence estimates of a PS point in complete, front, and back SAR image sets are approximately the same. This assumption is sound only if all of the PSI computations are strictly controlled to have a consistent and high accuracy. For this purpose, we process all of the image sets on the same computer and follow the exactly same parameters in PSI processing. In addition, the stack sizes of the three image sets must be sufficiently large (at least 12 images in our case). In contrast to a PS point, the temporal coherence of a change point in the complete set is partly lost as parts of the images lack the signal of this target. The coherence drops severely when such irrelevant images take a big part, i.e., the target disappears very early or emerges very late. In other words, the time of a change event is related to the evolution of temporal coherences subject to a series of break dates. More details will be discussed when we talk about how to detect events' occurrence times in Section 3.6.

We quantify coherence differences among complete, front, and back sets to be change indices. The change indices of a pixel x in disappearance (CI^D) and emergence (CI^E) scenarios are calculated by

$$CI^D(x)_{[-1, +1] \in \mathbb{R}} = \gamma_T^F(x) - \gamma_T^C \quad (23)$$

$$CI^E(x)_{[-1, +1] \in \mathbb{R}} = \gamma_T^B(x) - \gamma_T^C \quad (24)$$

where γ_T^C , γ_T^F , and γ_T^B denote temporal coherences in complete, front, and back sets. Images should be equally distributed in a sequence to avoid biases of change indices. A pixel is likely a DBC or EBC point when CI^D or CI^E tends towards 1, respectively. This indicates a remarkable coherence loss caused by a big change. In contrast, change indices of PS points should be around 0. The characteristics of change indices between PS and change points are clearly diverse. However, it is difficult to separate these two

point types perfectly by comparing their change indices.

The uncertainty in PSI computations may bias PS points' change indices away from 0. As for change points, their change indices could be too small and so falsely selected as PS points. Usually, we can use a thresholding approach as Otsu thresholding (Otsu, 1979) to separate these two point types. However, a thresholding approach certainly causes missed detection and false alarm because none of thresholds is perfect. To overcome this drawback, we developed a statistics-based method, which is explained in the next section, rather than thresholding.

3.4 Change detection

Based on change indices, we design a global, automatic, and statistical method to extract change points. Given that no big change occurs, a change index distribution over PS points in disappearance or emergence scenario is assumed to follow a Gaussian distribution

$$N(CI_{PS}(x)|\mu,\sigma) = \frac{1}{\sigma\sqrt{2\pi}} \exp\left(\frac{-CI_{PS}^2(x)}{2\sigma^2}\right). \quad (25)$$

This assumption is valid as only random factors are considered to cause variation of change indices. For example, disparity of temporal coherences for a PS point between different PSI computations should be credited to random phase noise. We regard such a disparity as a form of random noise for change indices. The mean μ of change indices is anticipated to be 0. However, a positive bias is likely to occur due to overestimation of temporal coherence (Bamler and Hartl, 1998; Touzi et al., 1999) from the shorter front or back SAR image set compared with the complete set. For example, as shown in (23), CI^D tends to positive bias if γ_T^F is overestimated. The standard deviation σ indicates the relative precision between two PSI results. High precision give rise to a narrow and tall curve of change index distribution with a small σ . In contrast to PS points, a change index distribution over change points does not conform to the Gaussian model because the big changes substantially and arbitrarily alter their temporal coherences computed from complete, front, and back sets. This distribution is complicated to be modelled but known to repel away from the Gaussian distribution towards 1. We utilize the significant difference between change index distributions over PS and change points to separate these two point types.

We first select PS points from a front or back SAR image set and sketch their change index distribution (red curve, Figure 6). Parts of them turn into change points if they disappear or emerge in the complete set; the others remain the same as PS points. This change index distribution is modelled as the sum of a Gaussian curve plus an asymmetric probability distribution function of a large right tail. The Gaussian curve originates from the change indices of the PS points that remain in the complete set; the right tail is caused mainly by the high change indices of the change points. We observe a positive bias of the change index distribution. For this reason, we can no longer regard change indices near 0 as an indication of PS points. To compensate for this bias, we shift this indication to 0.045 (magenta line, Figure 6), which pertains to the nadir of the peak. The asymmetric distribution is mainly subject to the number of change events and their temporal distances to the break date.

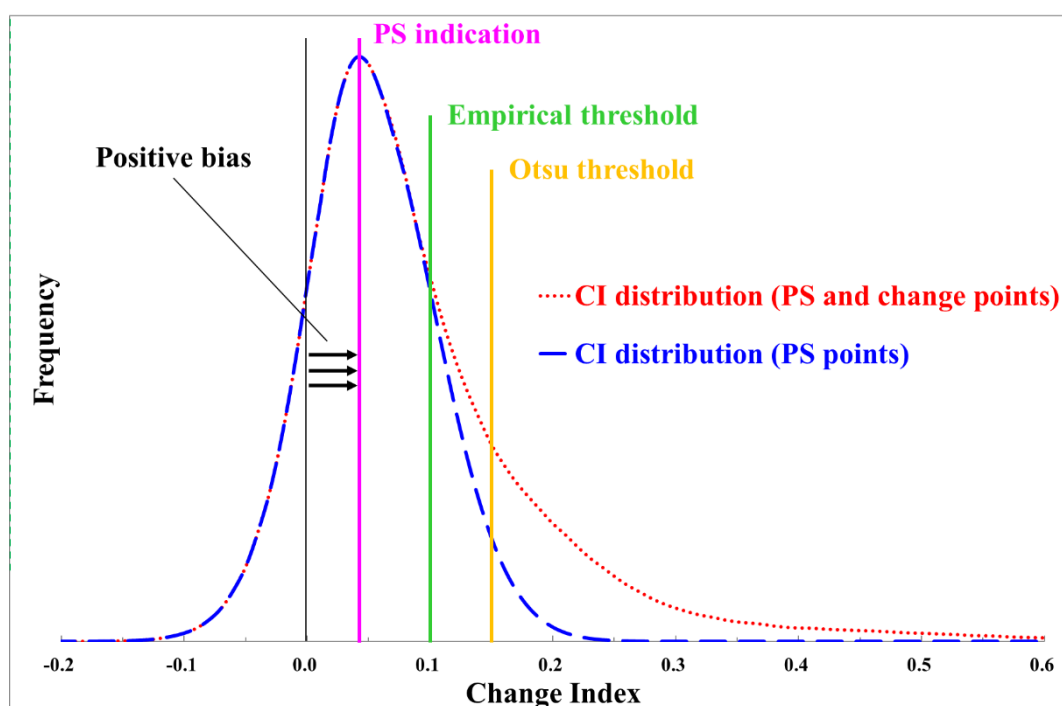


Figure 6: Examples of change index distributions

There are a variety of thresholding approaches to extract the change points. For example, we can set an empirical threshold 0.1 (green line, Figure 6) to detect as many change points as possible. However, the number of false alarms is unfavourably increased. Another way is to look for a threshold, which conforms to an optimization assumption. For instance, the Otsu threshold 0.15 (orange line, Figure 6) balances and makes the ratio between missed detection and false alarm nearly the same. No matter how we optimize thresholding, the PS and change points can never be distinguished without errors because their change index distributions are partly overlapped.

Rather than thresholding, we propose a workaround to substantially prevent errors. Those points on the right side of the PS indication (magenta line, Figure 6) are selected as change candidates. These candidates are either PS or change points. Instead of trying to directly extract the change points, we first check whether the change candidates are PS points in the complete SAR image set. If so, they are classified as PS points; otherwise, we label them as change points. As a result, there should be neither missed detection nor false alarm. The success of this method relies on precise PSI computations.

3.5 Limitations

There are three limitations for the single-break-date scheme. First, how to set up a break date? Which and whether big changes can be detected is dependent on the break date, which is manually set for specific interests. The changes, which occurred too early or late to the break date, do not have a chance to be detected. This requirement restricts the applicability particularly when a priori knowledge of scene changes is unavailable. Second, accurate occurrence times of big changes are absent as they are only known to disappear or emerge close to or after a break date. Last but not least, errors could happen, for instance, due to uncertainty and imperfection of a PSI processing. How to deal with such errors? To cope with these limitations, we need to integrate several single-break-date results into multi-break-date scheme. Each single-break-date result contributes a hint about which and when exactly changes take place. All of the hints combined provide extra information to exclude errors and locate occurrence times of change events.

3.6 Multi-break-date scheme

The multi-break-date scheme (Figure 7) demands a set of single-break-date results as input. Each pixel contains a sequence of change indices along with their corresponding initial point labels (PS, DBC, EBC, or void). We compare these initial point labels to determine its final label. The principle is to label a pixel as PS if all of its initial labels belong to PS. A pixel is labelled as DBC or EBC if any of its initial labels as such is found. When initial labels include both DBC and EBC, one of them should be wrong coming from the single-break-date results. We then resort to a voting step to select the change label in the majority. In case of equality, we deal with a contradiction and rather get rid of this pixel as void. We believe that this voting strategy is able to prevent false labels effectively. Once PS and change points are confirmed, those unlabelled pixels are classified to be void points. We apply spatial filters to further

remove false change points remained. Afterwards, the occurrence date of each change point is detected from the break dates based on the temporal variation in its change index sequence. In the end, the PS and change points along with the occurrence dates are combined to illustrate the spatiotemporal information.

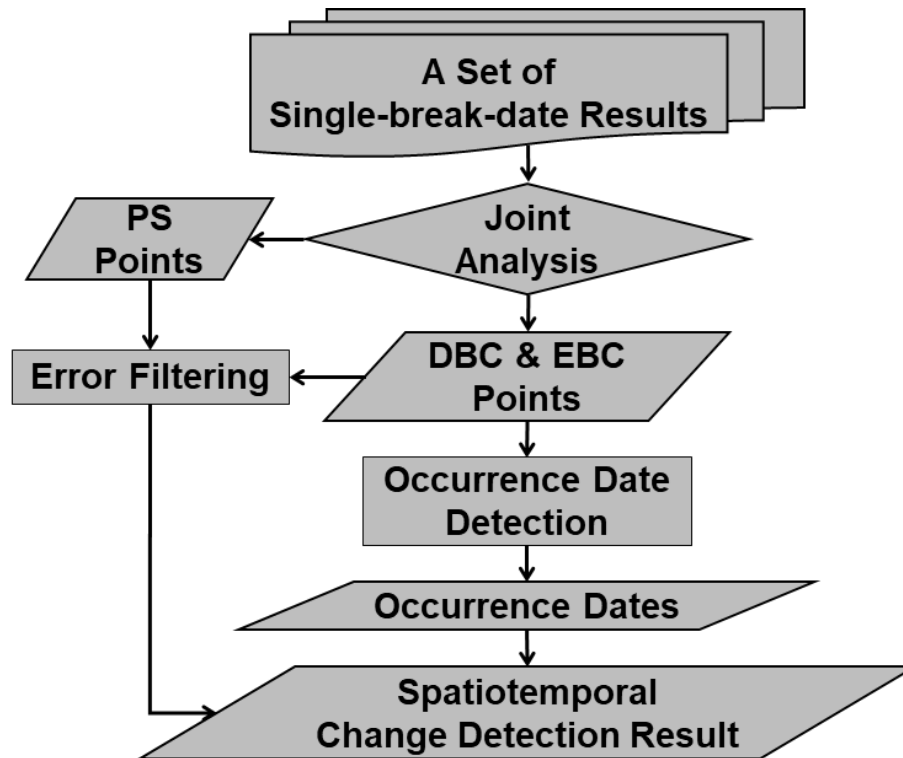


Figure 7: Flowchart of multi-break-date change detection scheme.

We exemplify how to detect a DBC point (Figure 8). Suppose the DBC point disappears at the middle date. We run a series of single-break-date examples, which results in a change index sequence. The break date and front SAR image set refer to the first single-break-date example. In the beginning, the change indices maintain constantly high and so imply that this point probably disappears sometime later. The turning point indicates the exact occurrence date, after which the change indices decrease gradually. The evolution of the change indices gives a hint to detect the disappearance date. We will discuss this topic later. Each single-break-date example supplies an initial point label, i.e., DBC, EBC, or void. Some void labels (grey) are present because their change indices are low or erroneous EBC labels coincides. This tells us that change points might be missed if only a single-break-date result is considered. These void labels are ignored here. Most of the single-break-date results show the correct DBC labels (red) when their change indices are high; otherwise, there are a few of erroneous EBC labels (green). Such errors are mainly credited to inaccurate PSI results at a local or global aspect. The local factors could be, for instance, strong

APS turbulence within a limited area. Such APS-induced phase noise may not be properly filtered out sometimes as we apply the same spatiotemporal filter to the whole image scene. For the global cases, an unsuitable selection of a master image will make the entire temporal coherences down. Simply speaking, errors always happen in single-break-date results. We then apply voting to the initial point labels to determine the final one in the majority, which turns out to be the correct DBC label. A similar process is also used to detect EBC points.

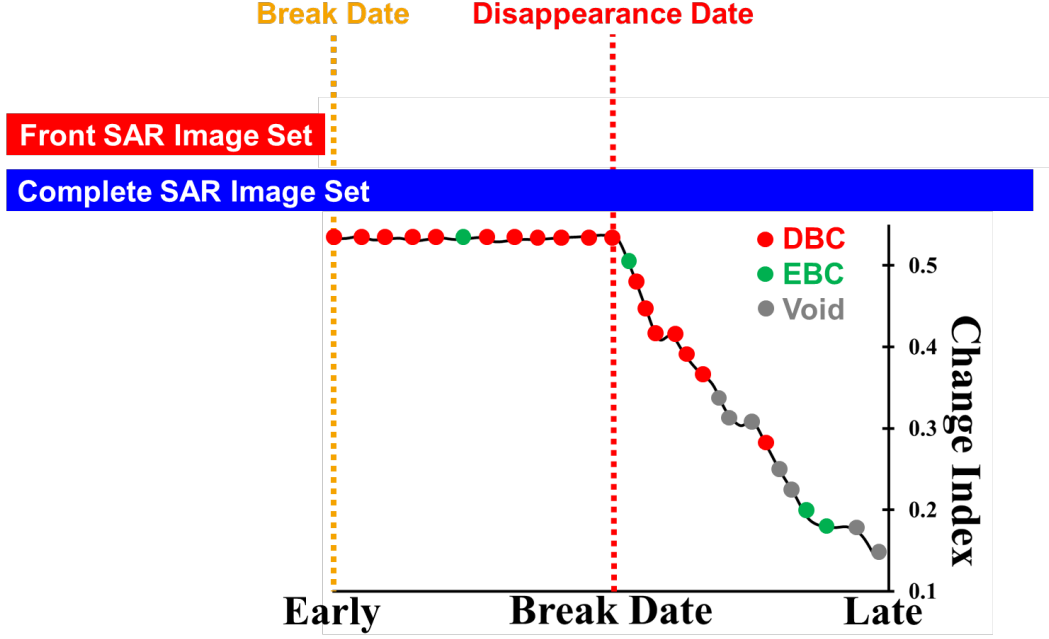


Figure 8: DBC detection in multi-break-date scheme.

We design an automatic way to detect change points' occurrence dates. Figure 8 is modified to Figure 9 for the following explanation. Considering (23), the temporal coherence γ_T^C over the entire image stack drops because the object of interest disappears on some date. In contrast, the temporal coherence γ_T^F of the front SAR image set stays equally high before the disappearance date. As a result, the change indices CI^D keeps consistently high above 0.5. After the object disappears, however, more and more incoherent signals are added to the front set in PSI computations. Consequently, γ_T^F decreases gradually and thereby CI^D is falling. We figured out that detecting a disappearance date is equivalent to locating the turning point in a change index sequence.

A simple geometric method is then proposed for this purpose. We consider only the break dates, whose initial point labels correctly pertain to DBC (red point), as the candidates for the disappearance date. First, a horizontal line 1 extends from the

sequence beginning to the left. Starting from this, a straight line 2 is drawn to the end of the sequence. We calculate the distances between the red points and the line 2. The turning point is then detected by looking for the longest distance (line 3). Finally, the corresponding break date is regarded as the disappearance date. We use a similar process to detect emergence dates of EBC points as well. The extension of line 1 is to ensure that line 2 does not overlap the change index sequence. This step keeps all of the red points on the right-hand side to make the distance comparison rational and simple. In theory, the length of line 1 does not affect the disappearance date detected while a longer length makes the overlap less possible. Our experiences suggest that the same length of the horizontal of the change index sequence suits most of the cases.

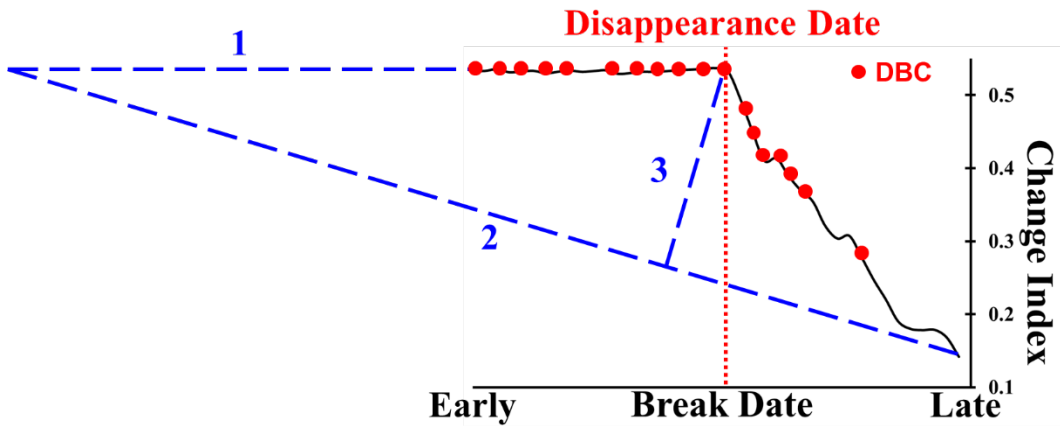


Figure 9: Detection of disappearance date.

3.7 Spatial error filtering

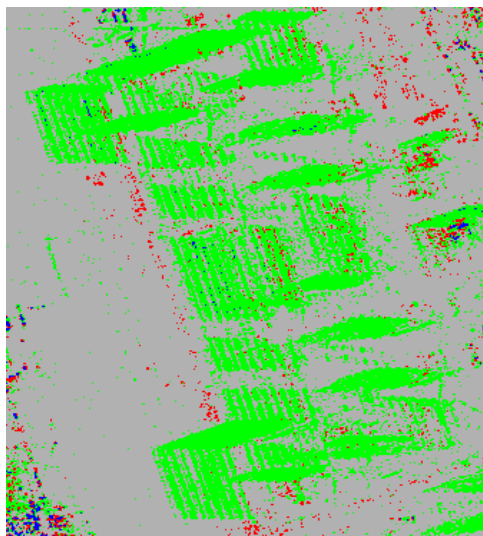
Most of the false change points, i.e., errors, can be avoided after voting in multi-break-date scheme. We resort to spatial characteristics between change points to further filter out the errors remained, if any. Our targets of interest are change events on structures of a certain size. For example, a demolished house causes a cluster of DBC points or a patch of EBC points attached to a building-like PS pattern indicates a partial construction. Such a group of change points is assumed to contain only one change label. Two kinds of errors are defined here along with their removal strategies operating in a sliding window. First, an isolated change point within a window of 3×3 is deleted. We choose the minimum window size because we intend to remove such errors as far as possible. Second, change points within a window are totally deleted if they contain different change labels. The larger a window size is, the stronger the filtering effect is made while more probably true change points are eliminated. We choose the minimum window size of 3×3 considering that only a minor portion of errors are remained after

the voting. Besides, we prefer to remove local errors clustering in a small size.

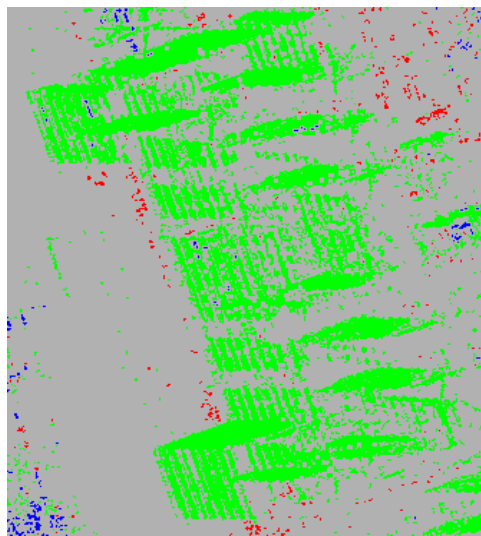
An example is shown in Figure 10. The new headquarters of federal intelligence service was erected in 2013. This event is successfully detected as many EBC points cluster to be a building-like shape. Before filtering, we observe some DBC points mixing with EBC points and regard them as possible errors. Such errors are then removed after filtering.



(a)



(b)



(c)

Figure 10: Example of spatial filtering. (a) Headquarters of federal intelligence service. Change detection result (b) before and (c) after filtering: blue, PS; red, DBC; green, EBC.

4. Simulated data test

4.1 Simulation procedure

We simulate a time series of M interferograms (int) (Figure 11), where PS, DBC, EBC, and void points are randomly generated and distributed, as input data for tests. First of all, we assign a stochastic constant phase φ_{cons} to the simulated phases $\varphi_{\text{sim}}^{int} [-\pi, \pi) \in \mathbb{R}$ of each pixel x :

$$\varphi_{\text{sim}}^{int}(x) = \varphi_{\text{cons}}(x), int = [1, M]. \quad (26)$$

Gaussian phase noise φ_{n}^{int} ($\mu = 0$, $\sigma = [-\pi, \pi) \in \mathbb{R}$) is then added to the simulated phases:

$$\varphi_{\text{sim}}^{int}(x) = \varphi_{\text{cons}}(x) + \varphi_{\text{n}}^{int}(x). \quad (27)$$

Here we consider only random thermal noise. The other noise sources, i.e., residual topographic errors, APS, orbital inaccuracy, flat Earth, temporal and geometric decorrelations, and image processing, are assumed to be perfectly calibrated or removed. All of the PS points are fixed, i.e., deformation velocity is 0. The temporal coherences of $\varphi_{\text{sim}}^{int}$ are calculated by

$$\gamma_{\text{T}}(x) = \left| \frac{1}{M} \cdot \sum_{int=1}^M \exp(j \cdot \varphi_{\text{sim}}^{int}(x)) \right| \quad (28)$$

which is derived from (20). Pixels are selected as PS points if their temporal coherences fulfil a specific threshold. Among them, in case a PS point disappears or emerges right at a break data (bd), a series of irregular phases $\varphi_{\text{irr}}^{int^D}$ or $\varphi_{\text{irr}}^{int^E} [-\pi, \pi) \in \mathbb{R}$, randomly generated, is added to its simulated phases as

$$\varphi_{\text{sim}}^{int}(x) = \varphi_{\text{cons}}(x) + \varphi_{\text{n}}^{int}(x) + \varphi_{\text{irr}}^{int^D}(x), int^D = [bd + 1, M] \quad (29)$$

$$\varphi_{\text{sim}}^{int}(x) = \varphi_{\text{cons}}(x) + \varphi_{\text{n}}^{int}(x) + \varphi_{\text{irr}}^{int^E}(x), int^E = [1, bd], \quad (30)$$

respectively. We then label them as DBC and EBC points. Finally, those pixels without any label (PS, DBC, or EBC) are regarded as void points.

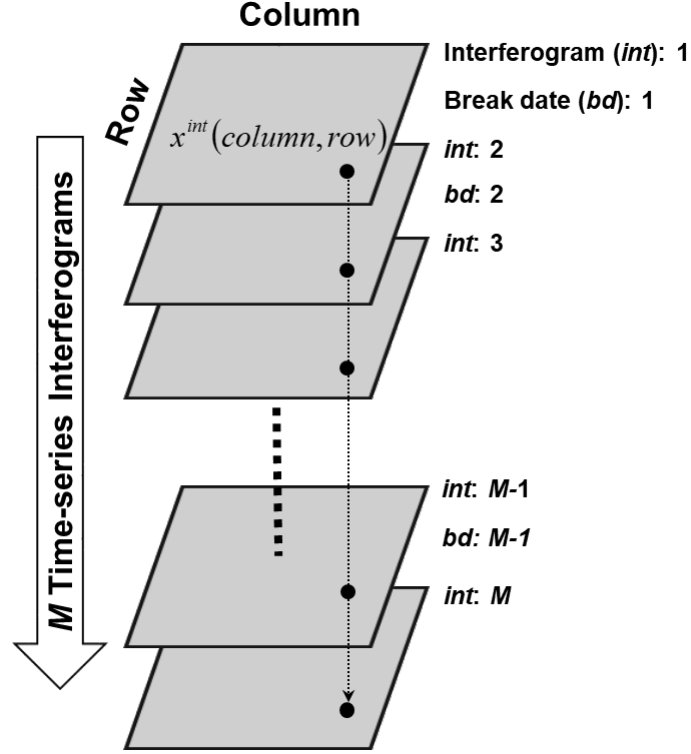


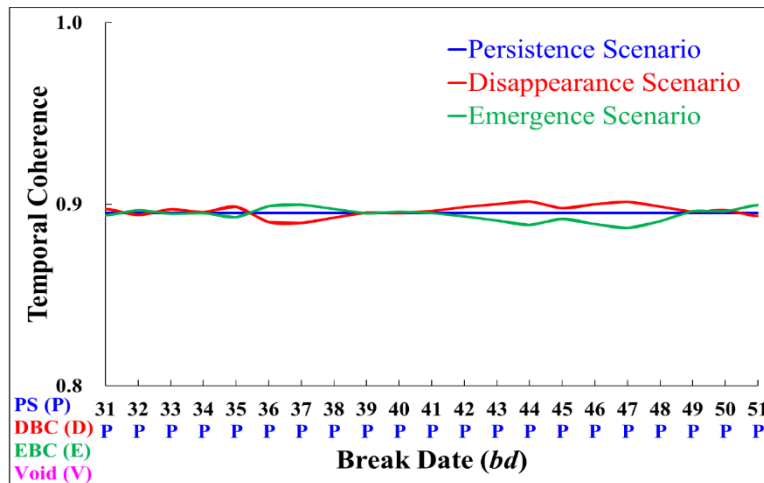
Figure 11: Simulated interferograms.

4.2 Simulated data

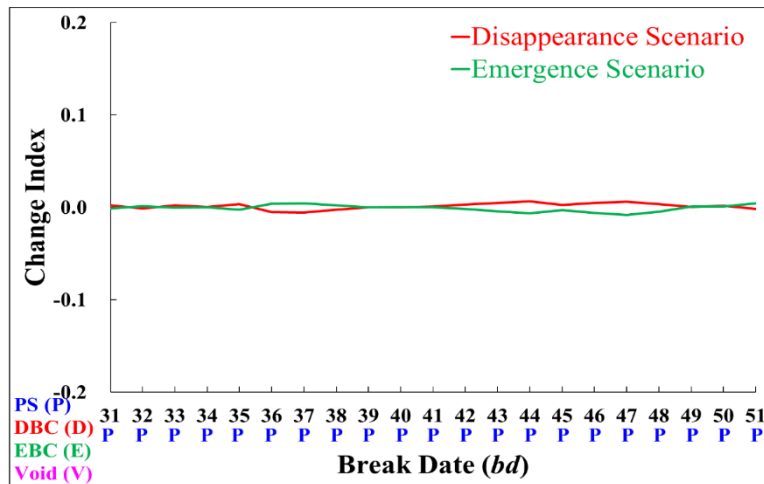
We simulated a scene like a developing city with numerous big changes (more than 30% coverage) to analyse the performance of our technique. For this purpose, we generated 80 time-series interferograms (500×500) containing 58% PS, 17% DBC, 17% EBC, and 8% void points. A temporal coherence threshold of 0.8 is used for PS selection. This threshold is also used in the real data tests (Section 5). More details about how to determine a suitable temporal coherence threshold refers to Section 5.6. The disappearance and emergence dates of the change points are evenly distributed from $bd: 31$ to 51.

One example of a PS point is shown in Figure 12. It is confirmed as a PS point because its temporal coherence (nearly 0.9) in the persistence scenario (Figure 3 and Figure 5, entire phase series used) exceeds the threshold of 0.8. As a result, all of the initial point labels are marked as PS. In the disappearance scenario, the temporal coherences at different break dates stay close to 0.9 with a standard deviation of 0.004.

Here only the phases before a break date are used to estimate the temporal coherence. The emergence scenario shows the same trend of temporal coherence sequence. The difference is that we only utilize the phases after a break date for coherence estimation. We can see that the temporal coherences are high and almost constant no matter which phase sections and break dates are chosen. This agrees with our definition of a PS point (Section 3.3). We then check the change index sequences in both the disappearance and emergence scenarios. The change indices are close to almost 0, which indicates that this point is not a change point.



(a)

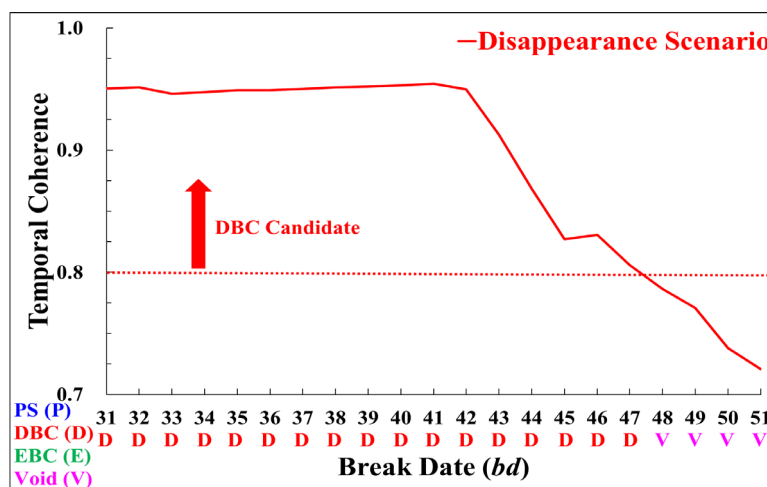


(b)

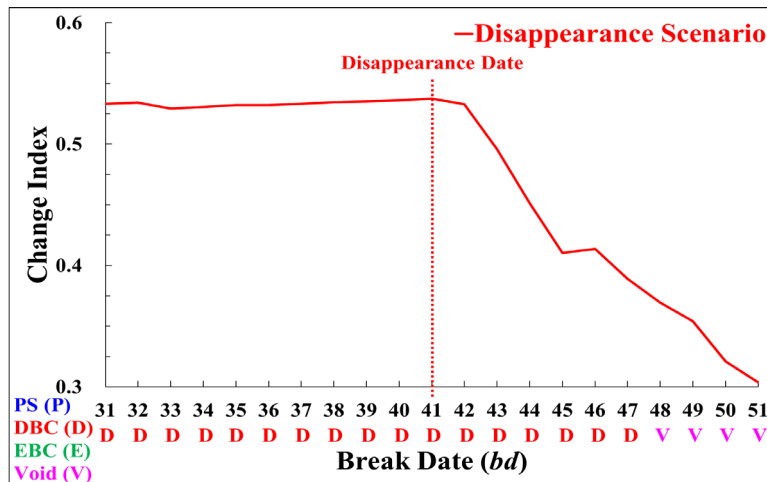
Figure 12: Simulated example of PS point's (a) temporal coherence sequence and (b) change index sequence along with initial point labels at different break dates. Persistence scenario uses entire phase series in coherence estimation; disappearance and emergence scenarios utilizes only phases generated before and after a break date, respectively.

Let's look into the example of a DBC point subject to a disappearance date $bd: 41$ (Figure 13). Before $bd: 41$, the temporal coherences maintain nearly 0.95, which

indicates existence of a PS point. Its temporal coherence begins to decline after $bd: 41$ as more and more pure phase noise (after this PS point disappears) are involved in coherence estimation. The change index sequence shows a typical trend of a DBC point. These high change indices imply a high probability of a DBC point. The turning point is right at $bd: 41$. By using our approach, we then successfully detect this DBC point and its disappearance date. Note that four initial point labels are void rather than DBC because their temporal coherences do not fulfil the threshold of 0.8 to be a DBC candidate (a PS point before disappearance). Nevertheless, these void labels in minority do not affect the final decision that labels this point as DBC after voting of the initial point labels.



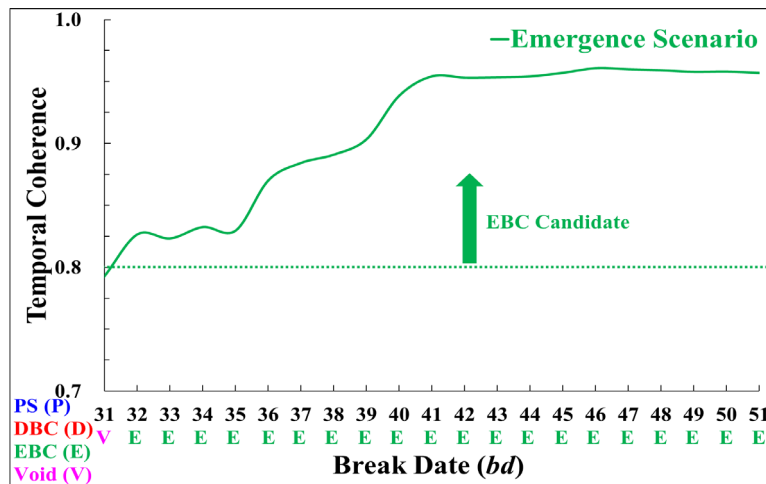
(a)



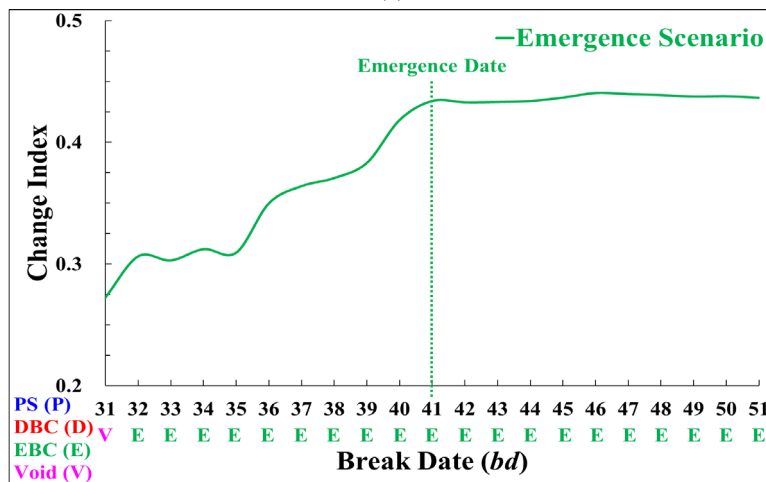
(b)

Figure 13: Simulated example of DBC point's (a) temporal coherence sequence and (b) change index sequence along with initial point labels at different break dates. Temporal coherence in complete image set is 0.42. Disappearance scenario uses only phases generated before a break date to estimate coherence.

The example of an EBC point (Figure 14) shows a reverse behaviour to DBC (Figure 13). The temporal coherences maintain nearly 0.95 after this point emerges as a PS point at $bd: 41$. Note that only the phases generated after a break date are used to calculate the coherences. The temporal coherences are lower when the break dates are set earlier. The reason is that more and more pure phase noise (before emergence of the PS point) are included to compute the temporal coherences. The change indices are sufficiently high to fulfil the condition of an EBC point. They increase gradually from the earliest break date and then keep around 0.43 after $bd: 41$. At $bd: 31$, the point cannot be selected as an EBC candidate because the temporal coherence is below the threshold of 0.8. Its initial label is later marked as void since it is neither a PS point. During voting, this point is decided to be an EBC point because of initial point labels of EBC in majority.



(a)



(b)

Figure 14: Simulated example of EBC point's (a) temporal coherence sequence and (b) change index sequence along with initial point labels at different break dates. Temporal coherence in complete image set is 0.52. Emergence scenario uses only phases generated after a break date to estimate coherence.

4.3 Accuracy assessment

We assess the detection accuracy by using confusion matrix (Table I). Four classes include PS, DBC, EBC, and void. Each column and row represents the instances in a true and detected class, respectively. The diagonal instances are the correctly detected points. Dividing the sum of the diagonal instances by the total amount of the instances obtains the overall accuracy. However, the overall accuracy might be misleading. For instance, an overall accuracy could be high while some classes contain a considerable amount of errors. For a complete description of accuracy, we must look into producer's and user's accuracies for each class. A producer's accuracy is the number of correctly detected instances divided by the number of total instances in a column. It reflects, for each true class, the ratio of true instances which are correctly detected. Dividing the number of correctly detected instances by the number of total instances in a row derives a user's accuracy. We therefore know the ratio of correctly detected instances in each detected class.

Table I Confusion matrix

		Reference				
		PS	DBC	EBC	Void	Sum
Result	PS	145544	110	93	0	145747
	DBC	0	41647	0	0	41647
	EBC	0	0	41713	0	41713
	Void	0	0	0	20893	20893
	Sum	145544	41757	41806	20893	250000
		PS	DBC	EBC	Void	
Producer's Accuracy		100%	99%	99%	100%	
User's Accuracy		99%	100%	100%	100%	
Overall Accuracy		99%				

The confusion matrix (Table I) shows that the overall accuracy is 99% and all of the producer's and user's accuracies are better than 99%. Such high accuracy tells that our approach works well given perfect PSI computations. In this test, we assume that those PSI-related phase noises caused by residual topographic errors, APS, orbital inaccuracy, flat Earth, temporal and geometric decorrelations, and image processing, are perfectly calibrated or removed. In practice, they must be delicately handled in a PSI processing for an accurate result. This is not an easy task and requires deep

expertise and experience. We do not dig into the details in this study. While the overall accuracy is high, we also check the producer's and user's accuracies as follows.

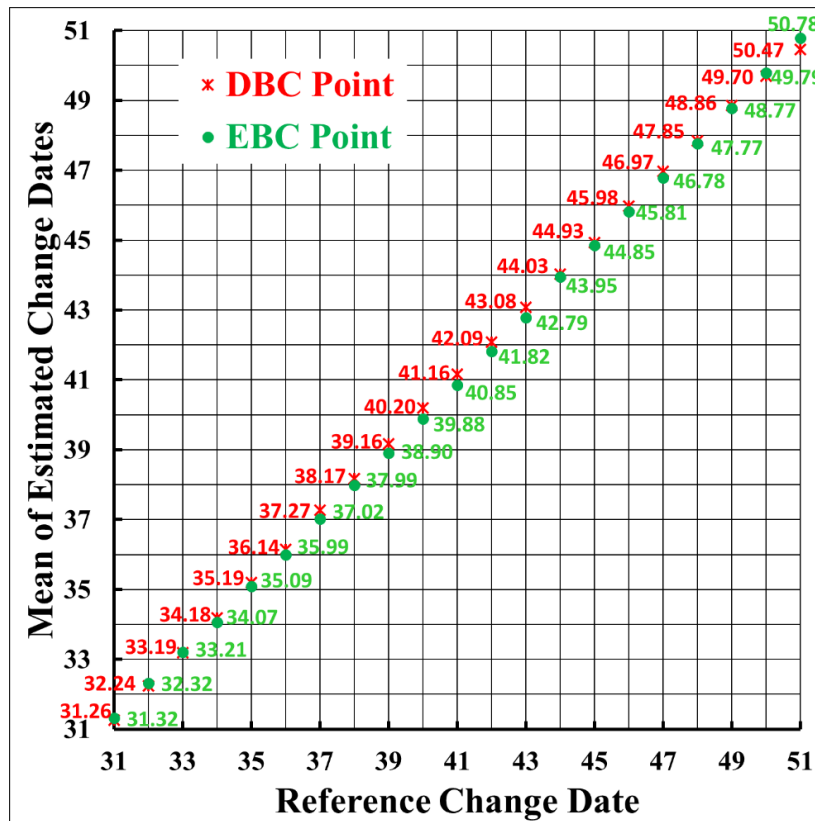


Figure 15: Mean of estimated change dates versus each reference change date. Correlation coefficient of 0.999, mean (absolute) difference 0.17, maximum (absolute) difference 0.53 for DBC; 0.999, 0.16, and 0.32 for EBC.

The only errors are the change points falsely labelled as PS, which result in producer's accuracy of 99% for both change labels and user's accuracy of 99% for PS. The temporal coherences of these change points in the complete image set (Figure 3) are still above the threshold of 0.8. Consequently, they turn out to be PS points that are missed detections of change points. Such errors often happen if a change point emerged very early or disappeared very late. In this case, temporal coherences of change points in the complete set are overestimated. The reason is that those images, in which the change points act as PS points after emergence or before disappearance, account for a large proportion of the whole images. The solution is to make sure sufficient images in front and back sets when choosing a period of break dates to detect changes of interest. According to our experience, a front or back set should occupy at least 30% of a complete set.

The estimated change dates are compared with the reference (Figure 15). For each reference change date, we calculate the mean of the estimated disappearance dates (red) and plot it in the vertical axis. The correlation coefficient is 0.999, indicating a high agreement between the estimated and reference disappearance dates. The mean (absolute) difference is 0.17 and the maximum (absolute) difference is 0.53. The accuracy of estimated disappearance date is then regarded as sublevel of break date. That is to say, given Sentinel-1 images, the accuracy could be less than 6 days (shortest temporal baseline) under optimal conditions, i.e., sufficient images and high-quality PSI results. The estimated emergence dates (green) show the same characteristics as the disappearance case. The correlation coefficient is also 0.999. The mean difference is 0.16 and the maximum difference is 0.32. In summary, we prove that our method can detect events' occurrence dates with a considerably high accuracy.

5. Real data test

5.1 Data

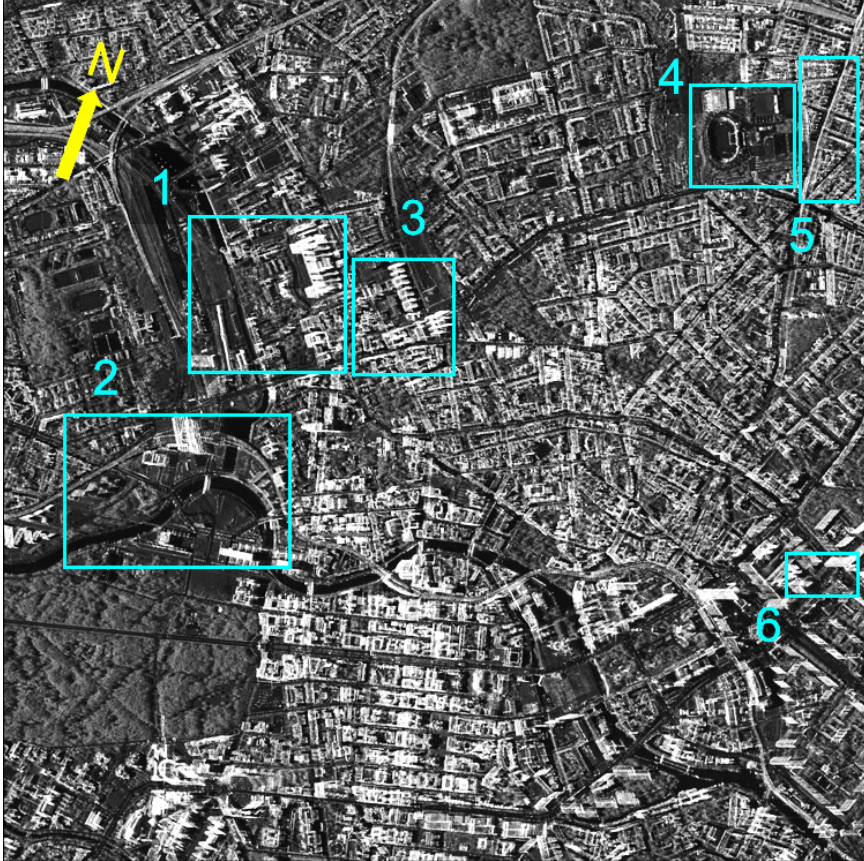


Figure 16: Mean TerraSAR-X image over study area. Patches 1 to 6 are used for in-depth analysis.

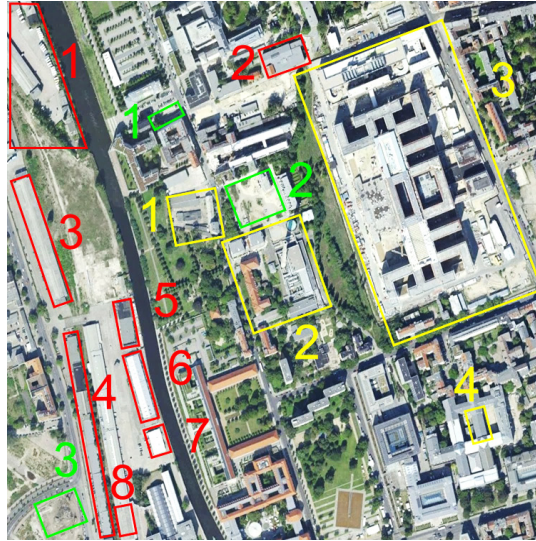
Our study area (Figure 16) covers the city centre of Berlin (25 km²), containing Berlin Central Station, Spree River, governmental offices, commercial buildings, houses, sport facilities, highways, metro lines, parks, etc. The mean TerraSAR-X image shows many bright clusters of strong signals, which mainly come from structures and appear to be potential PS and change points. Patches 1 to 6 are used for in-depth analysis. Patch 1 is the main area of interest where different types of construction occurred over time, including the new headquarters of federal intelligence service. There were many new buildings built in patch 2. We also found reconstruction on Berlin Central Station and a bridge. Patch 3 contains several buildings that were demolished or erected in a business district. In patch 4, we want to detect the changes of the sport facilities in Mauerpark and Friedrich-Ludwig-Jahn-Sportpark. We test whether our approach is able to detect a new metro line in patch 5. The last example investigates construction

progresses of two single high-rise buildings in patch 6. More details will be discussed later.

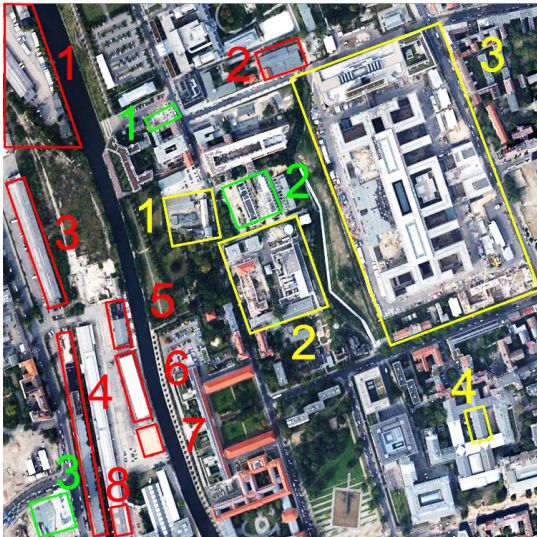
We used forty TerraSAR-X images (Table II) for our test, which were acquired in High Resolution Spotlight mode along an ascending orbit from October 27, 2010 to September 4, 2014. The incidence angle is around 30°. The polarization is VV, i.e., vertically polarized signals are transmitted and received. The azimuth and slant-range resolutions are 0.87 m and 0.45 m, respectively. All of the images were precisely co-registered and resampled into 5000 × 5000 grid (ground resolution: 1m). We found many changes in the city around 2013 from Google Earth’s historical images. The thirteen break dates (*bd*: 16 to 28) were then chosen to detect these changes. We compared and analysed our results with three Google Earth’s images (ground truth) taken on September 12, 2010, May 20, 2012, and September 5, 2014.

Table II TerraSAR-X images and break date setup

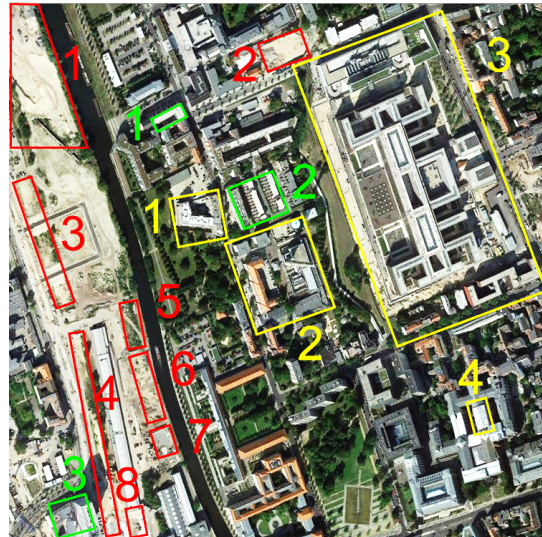
Acquisition Dates of TSX Images			
2010/10/27	2011/08/31	2013/08/26	2014/02/07
		<i>bd = 21</i>	
2010/11/18	2011/10/03	2013/09/17	2014/03/01
		<i>bd = 22</i>	
2011/01/23	2011/12/30	2013/09/28	2014/03/23
		<i>bd = 23</i>	
2011/02/14	2012/01/10	2013/10/20	2014/05/06
		<i>bd = 24</i>	
2011/03/08	2012/02/01	2013/10/31	2014/05/28
		<i>bd = 25</i>	
2011/03/30	2012/02/12	2013/11/22	2014/06/19
	<i>bd = 16</i>	<i>bd = 26</i>	
2011/06/04	2013/06/21	2013/12/03	2014/07/11
	<i>bd = 17</i>	<i>bd = 27</i>	
2011/06/15	2013/07/13	2013/12/25	2014/08/02
	<i>bd = 18</i>	<i>bd = 28</i>	
2011/07/18	2013/07/24	2014/01/05	2014/08/24
	<i>bd = 19</i>		
2011/08/20	2013/08/15	2014/01/16	2014/09/04
	<i>bd = 20</i>		



(a)



(b)



(c)

Figure 17: Aerial images (Google Earth) over patch 1 (Figure 16) at the north of Berlin Central Station acquired on (a) September 12, 2010, (b) May 20, 2012, and (c) September 5, 2014. Building change (ground truth): red, disappearance area; green, emergence area; yellow, complex area.

We focus our analysis on patch 1 (Figure 16) at the north of Berlin Central Station where various construction events occurred. The three Google Earth images (Figure 17) display what happened in this area. The buildings in disappearance areas 1 to 8 (red) were demolished over time after September 2010. The building in disappearance area 7 is gone in Figure 17 (b); the rest in other areas vanish in Figure 17 (c). Accordingly, we expect dense DBC points to be detected inside these areas. We observe some new buildings in emergence areas 1 to 3 (green) where EBC points are anticipated on the newly-built substructures. Parts of these new buildings showed up in 2012 (Figure 17

(b)). They appeared to be still under construction at this moment. The complete buildings can be seen later in 2014 (Figure 17 (c)). The building changes in complex areas 1 to 4 (yellow) cannot be purely attributed to either disappearance or emergence. In complex area 1, two different buildings were present at the same place in 2012 (Figure 17 (b)) and 2014 (Figure 17 (c)). We are not sure whether the old building was levelled down in 2013 or the new one was already erected back then. A similar ambiguity is also found in complex area 4. The white roof replaced the grey one as shown in Figure 17 (b) and Figure 17 (c). Another question is that the roof was replaced or merely painted to white? Given the first case, our approach will detect the corresponding change points if the old roof disappeared or the new roof emerged in 2013. Otherwise, PS points will be probably found considering that only the roof color was changed. In complex area 2, we see that some constructions were in progress in 2012 (Figure 17 (b)) and then completed in 2014 (Figure 17 (c)). The completed buildings look like the same as those (Figure 17 (a)) in 2010. We thus infer that there were renovation activities in this area, in which different point labels should be mixed. The new headquarters of federal intelligence service was built in complex area 3. The construction took roughly 7 years since 2006 until 2013. However, it is difficult to recognize this event and to estimate its progress from the Google Earth images. Our aim is to monitor the construction progress in detail to find out where and when the substructures were removed or constructed by using our approach.

5.2 PS extraction

We show the PS points extracted from all of the SAR images (Table II) and discuss their spatial distribution. The temporal coherence image (Figure 18) manifests the coherent SAR signals reflected from the intensive structures and those incoherent regions such as grass, forest, and river. The high-coherence (brighter) signals indicate potential PS points, which fit well the linear velocity model and did not undergo any big changes. They can be later extracted by thresholding based on their temporal coherences and then used to monitor structural deformations. In our study, we are more interested in those low- or moderate-coherence objects. Due to big changes, they were likely present during only a certain time window rather than the entire acquisition period of the SAR images. This is the reason why their coherences are partly lost. For instance, patch 1 (Figure 18) presents rather moderate coherence while lots of buildings were present between 2010 and 2014 (Figure 17). This is a hint that constructions took place. Our purpose is to detect such change events automatically.

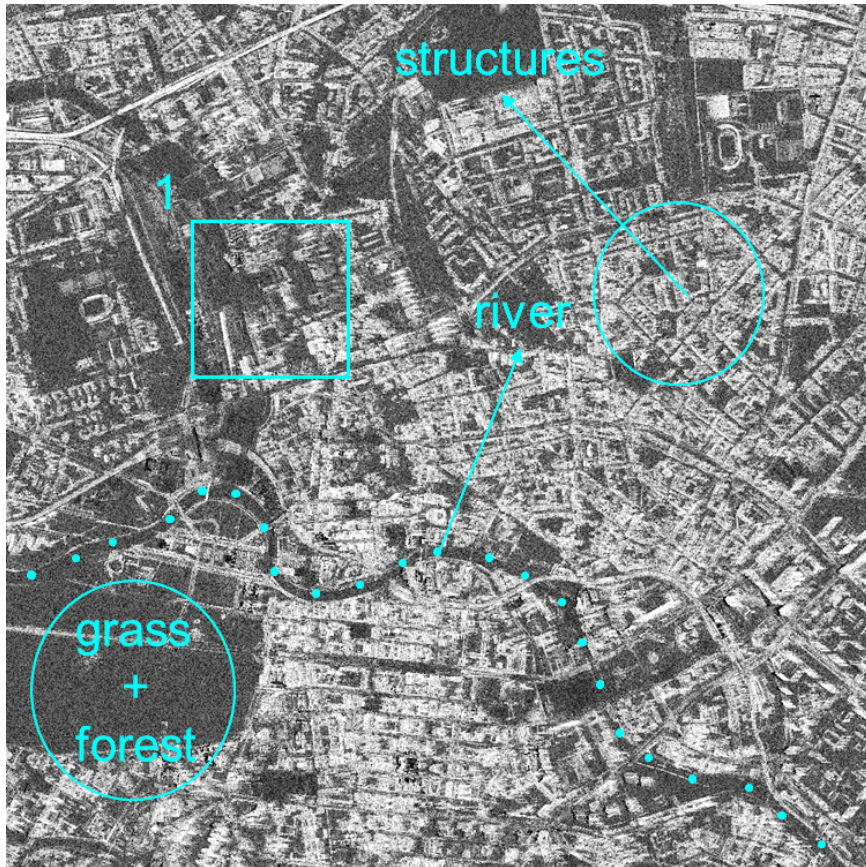


Figure 18: Temporal coherence image over study area. Patch 1 is used for in-depth analysis.

We used coherence threshold of 0.8 to extract PS points (Figure 19). We will explain in Section 5.6 why we chose 0.8 as the threshold. Most PS points come from structures and cluster as various building- and infrastructure-like patterns. For example, the PS points on the top-left corner form an outline of a railway system. In contrast, we cannot find PS points on the incoherent areas, i.e., grass, forest, and river. Patch 1 (Figure 20) is enlarged for in-depth investigation. Most of the PS points are located on the intact buildings outside the disappearance and emergence areas. Only a few of them are found in the complex areas. Without a priori knowledge, people would assume the lack of PS points originates from incoherent areas such as vegetation. In fact, the buildings were or are there but are present only in some of the SAR images due to big changes. Such change information can be retrieved later by using our new technique.

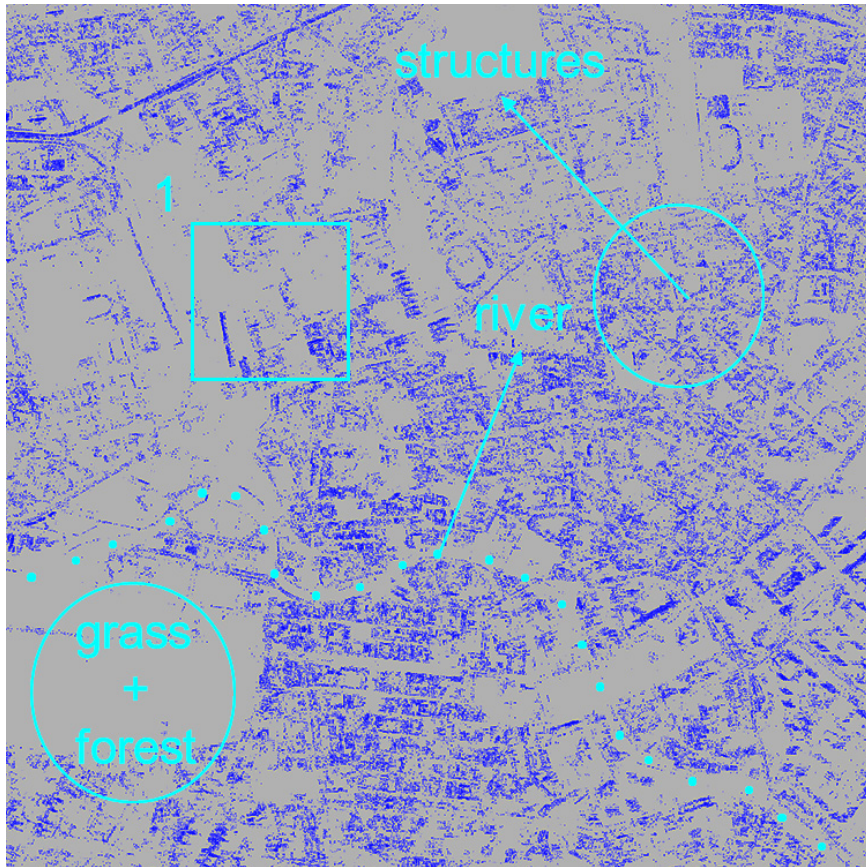


Figure 19: PS points (blue) over study area. Patch 1 is used for in-depth analysis.



Figure 20: PS points within patch 1 (Figure 19). Building change (ground truth): red, disappearance area; green, emergence area; yellow, complex area.

5.3 Single-break-date result

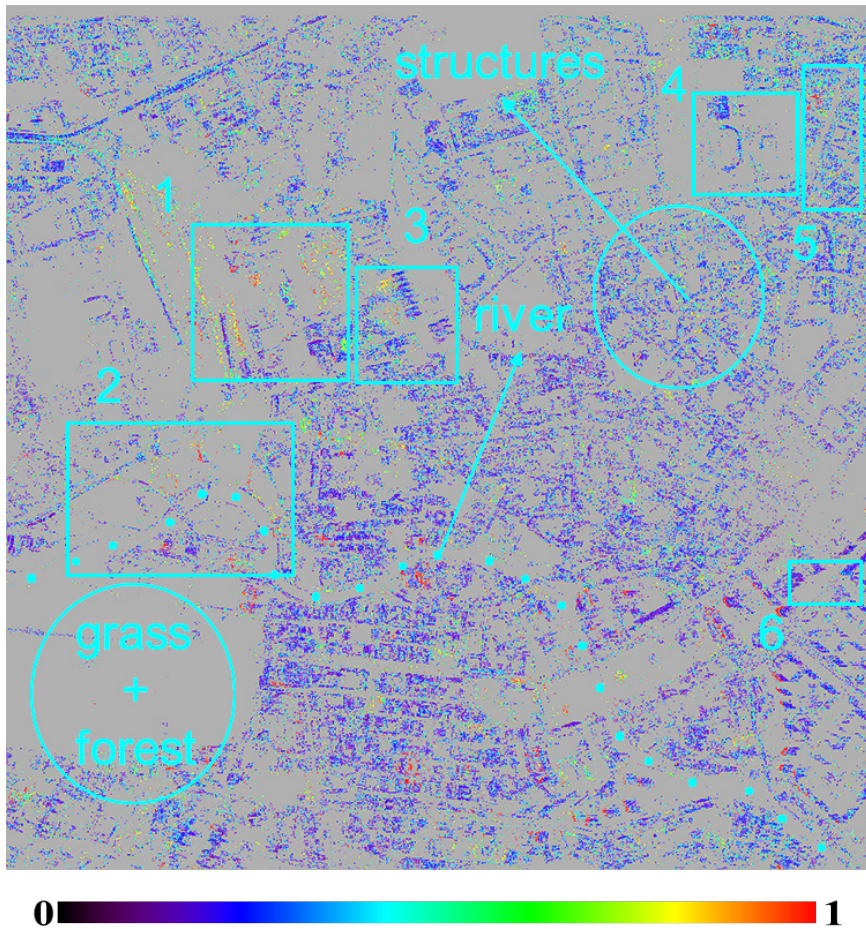


Figure 21: Change index image (disappearance scenario). Patches 1 to 6 are used for in-depth analysis.

We demonstrate a single-break-date result subject to the break date $bd: 16$ (Table II) between February 12, 2012 and June 21, 2013. In the disappearance scenario, PS points are extracted from the first 16 images taken before $bd: 16$ and regarded as change candidates. Note that these change candidates are not the normal PS points (Figure 19) extracted from the entire SAR stack. These candidates' change indices quantify their probabilities of disappearing since $bd: 16$, i.e., DBC points (Figure 21). There are no information from the inconsistent areas (grass, forest, river, etc.). Most of the structures manifest low change indices as no devastating and extensive disasters like earthquake hit Berlin. Those structures highlighted by high change indices were likely demolished due to construction close to or after the break date. For example, we observe many high change indices in patches 1 to 6 (especially the first three).

Let's check the change index image of the emergence scenario (Figure 22). Here the change candidates are those PS points that are extracted from the images taken after $bd: 16$. Their change indices are proportional to the probabilities of emerging since $bd: 16$. Low change indices are distributed across the whole area. This makes sense because Berlin is not a highly developing and expanding city neither a city under reconstruction. We observe some high change indices grouped as structure-like shapes in patches 1 to 6. For instance, the high change indices on the top-right corner of patch 1 come from the new headquarters of federal intelligence service.

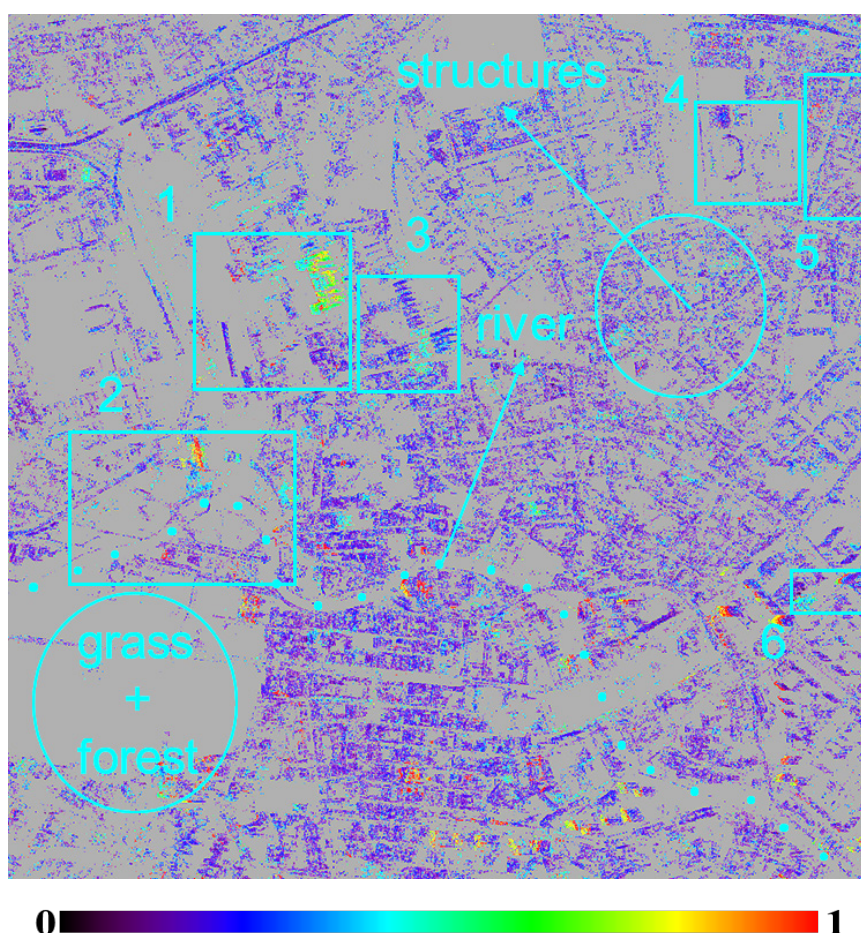


Figure 22: Change index image (emergence scenario). Patches 1 to 6 are used for in-depth analysis.

The change index images of the disappearance and emergence scenarios only quantify probabilities of being change points (Figure 21 and Figure 22). These change indices are then employed to detect initial change labels at the break date $bd: 16$. The change detection result (Figure 23) reveals the steady (PS), disappearing (DBC), and emerging (EBC) structures, which are clearly distinguished. The change events in patches 1 to 6 are successfully caught. Compared with the pure PS extraction (Figure 20), we now add also change points into the disappearance, emergence, and complex

areas (Figure 24). Overall, these detected changes agree with the ground truth (Figure 17). More details will be discussed in the multi-break-date result (Section 5.4). Note that here these initial change labels are subject to the break date bd : 16. More change points might be identified in the multi-break-date result (bd : 16 to 28); on the other hand, some of them could be picked up as errors and then deleted after voting. In addition, we only know the initial change points disappeared or emerged since bd : 16. The accurate occurrence times are still unknown, which is the main limitation of the single-break-date scheme. To overcome this weakness, we then consider the multi-break-date result in the next section.

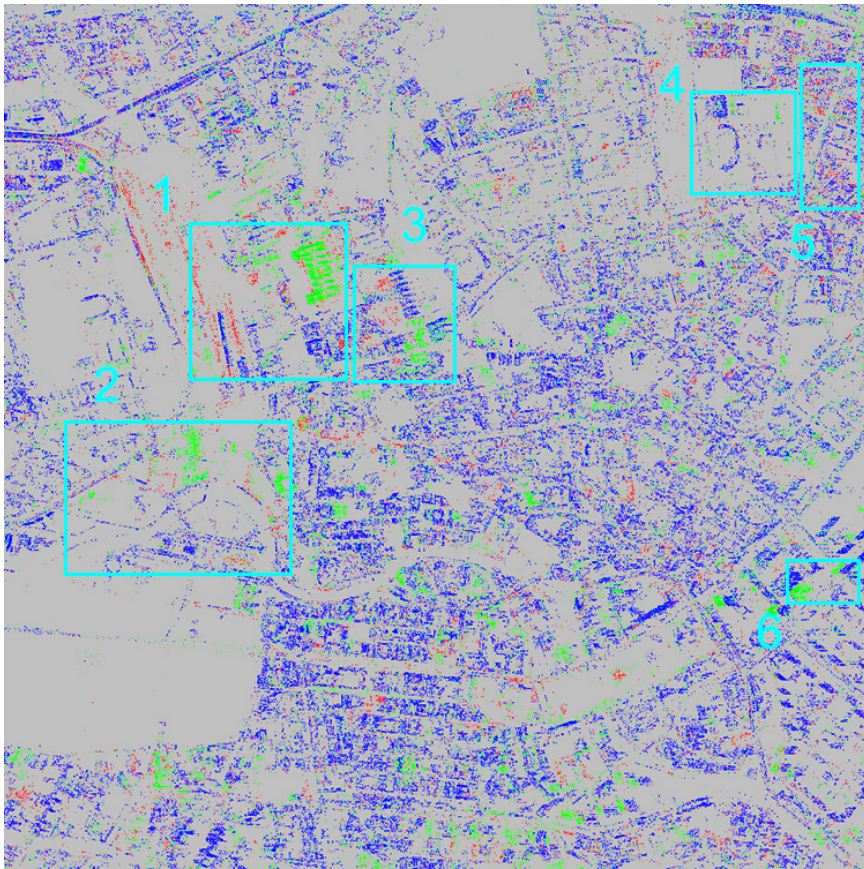


Figure 23: Change detection result: steady, disappearing, and emerging structures represented by PS (blue), DBC (red), and EBC (green) points. Patches 1 to 6 are used for in-depth analysis.

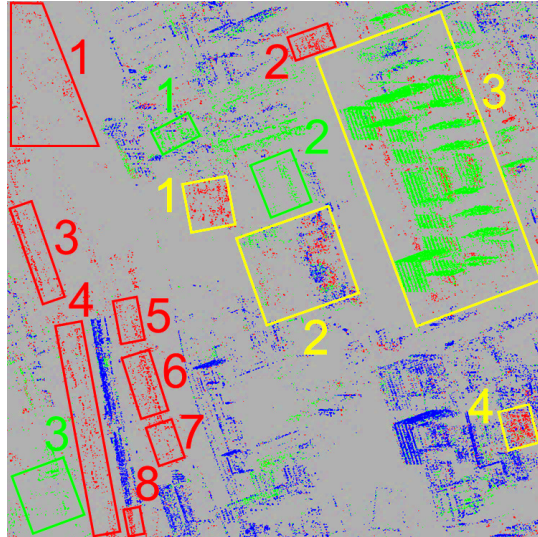
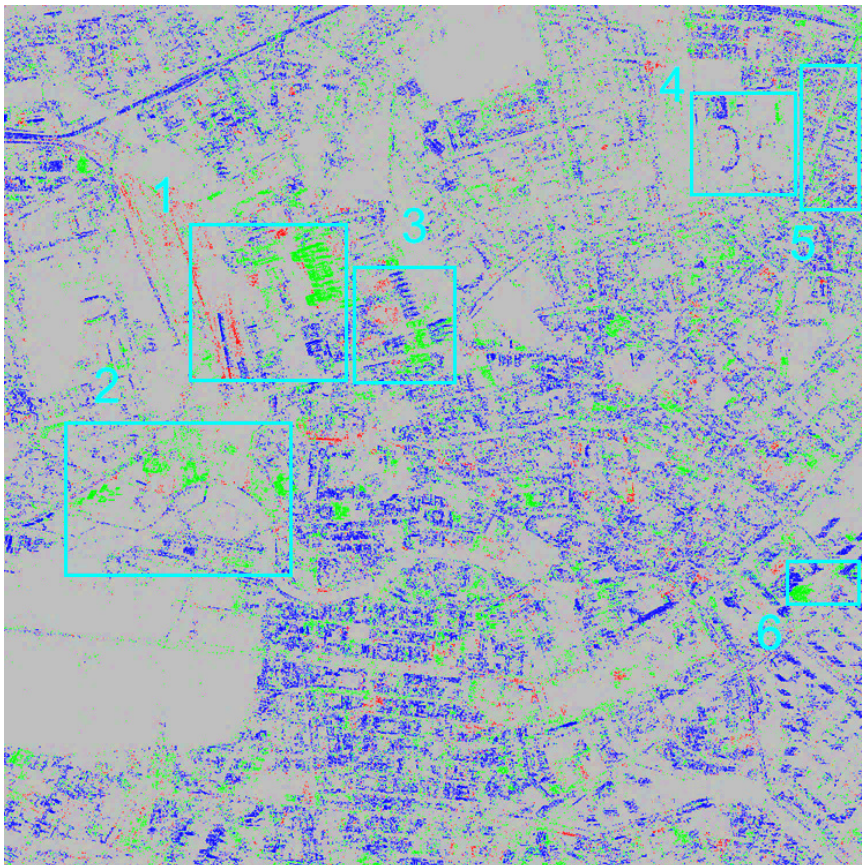
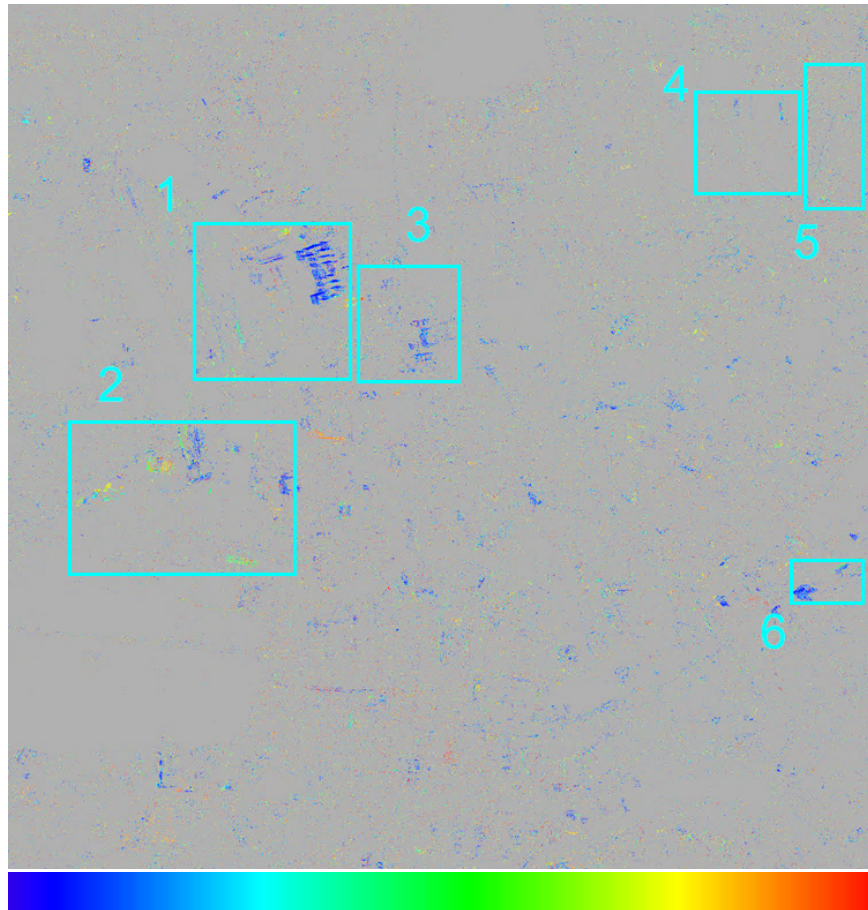


Figure 24: Change detection result within patch 1 (Figure 23). Building change (ground truth): red, disappearance area; green, emergence area; yellow, complex area.

5.4 Multi-break-date result



(a)



(b)

Figure 25: Spatiotemporal change detection result. Patches 1 to 6 are used for in-depth analysis. (a) Steady, disappearing, and emerging structures represented by PS (blue), DBC (red), and EBC (green) points. (b) Disappearance and emergence dates: blue to red, earliest to latest in 2013.

All of the single-break-date results (bd : 16 to 28) are involved in the multi-break-date processing. The spatiotemporal change detection result (Figure 25) reveals where the changed structures are along with their occurrence times. We first compare and analyse patch 1 (Figure 26) with the ground truth (Figure 17) as follows. The rest of patches will be discussed in Section 5.5.

Overall, our results (Figure 26) agree with the ground truth (Figure 17). The buildings in disappearance areas 1 and 3 to 7 are detected to be demolished by the middle 2013, followed by those in areas 2 and 8. The ground truth shows that the building in area 7 was already gone on May 20, 2012 (Figure 17 (b)); in contrast, those in other areas were still there and vanished later on September 5, 2014 (Figure 17 (c)). This is the reason why the detected disappearance dates in area 7 were earlier than the other areas.

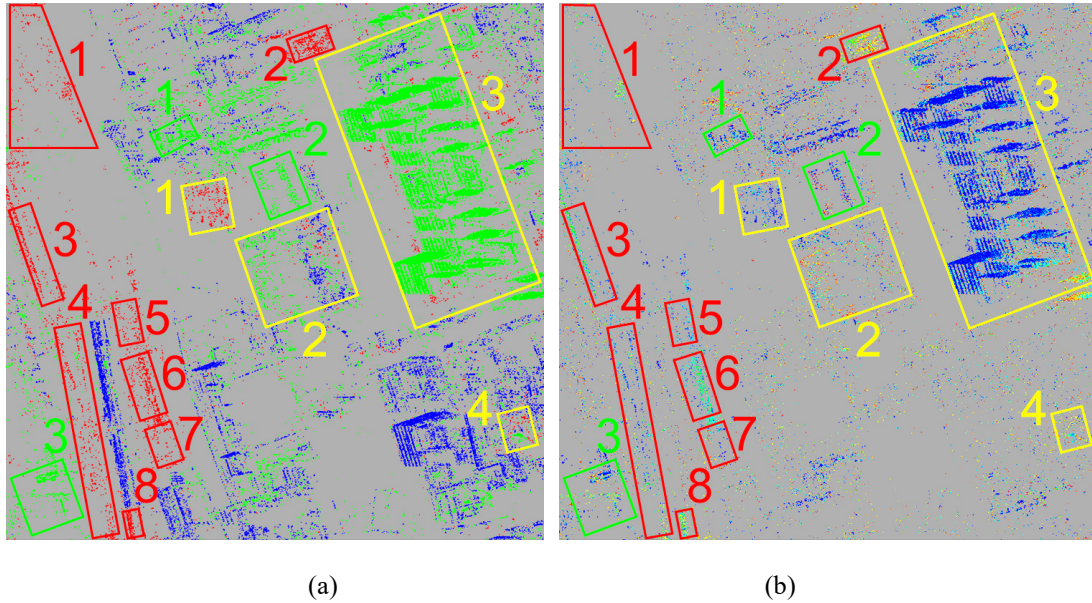
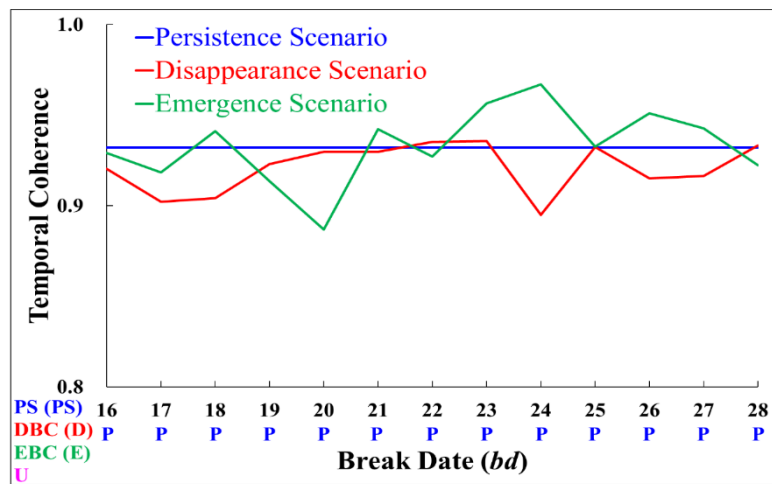


Figure 26: Spatiotemporal change detection result in patch 1 (Figure 25). Building change (ground truth): red, disappearance area; green, emergence area; yellow, complex area.

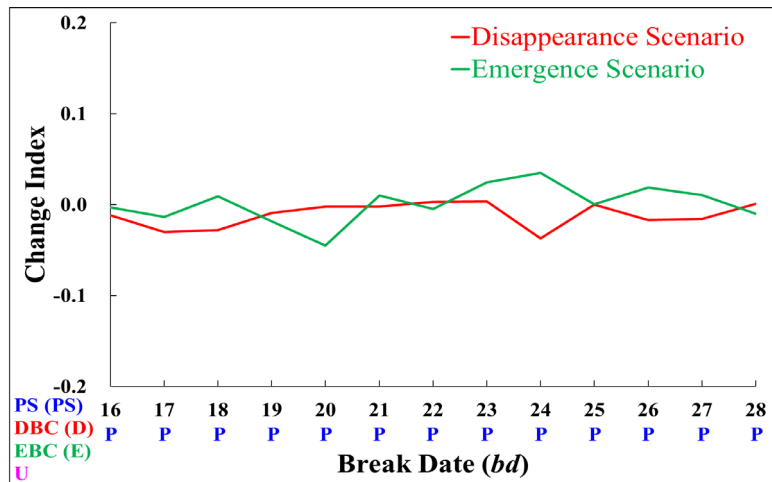
Our result reveals that a new building was erected in emergence area 1 in early 2013 (Figure 26). In fact, parts of this building was completed on May 20, 2012 (Figure 17 (b)) and the rest should be constructed soon in 2013. In emergence area 2, the unfinished new apartments were present on May 20, 2012 (Figure 17 (b)), which leads to the EBC points appearing on the early dates. The new office building in emergence area 3 was still under construction in 2012 (Figure 17 (b)) and then completed before September 5, 2014 (Figure 17 (c)). This fact is consistent with our finding that the corresponding EBC points emerged gradually since 2013.

In complex area 1, the ground truth (Figure 17) cannot tell whether the old building was demolished or the new one was built in 2013. This question has been answered in our result (Figure 26): the old building was gone in 2013. We infer that the new one should be erected after 2013. We find that certain substructures in complex area 2 were removed or added during the second half of 2013 (Figure 26). This finding corresponds to the renovation events shown in the ground truth. We want to monitor the construction progress in complex area 3, which is difficult to see even from the ground truth. Our result shows that many EBC points form a building-shaped pattern, i.e., the new headquarters of federal intelligence service. The main building structure was constructed in early 2013 and then other substructures were added to it over time. In addition, we also observe some disappearing substructures around. They are considered to be some temporary materials on the foundations and were removed in the early stage. Some change points are shown in complex area 4. We then prove that the roof (or the

entire building) was replaced by a new one after the middle 2013 rather than painted into white (Figure 17 (c)).



(a)

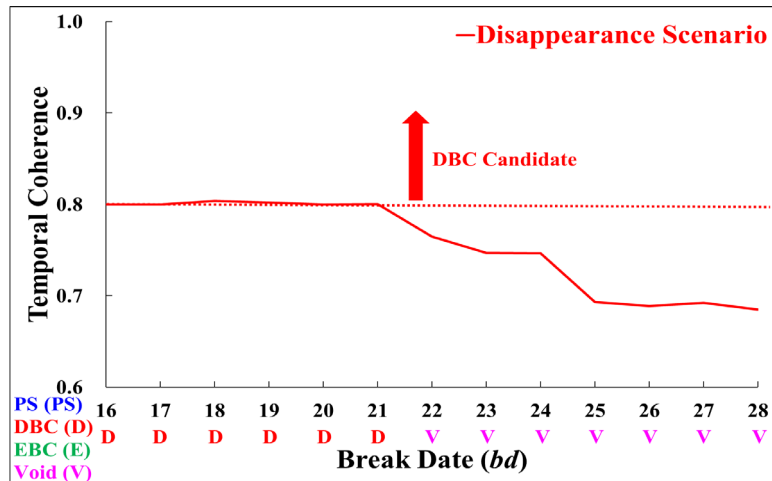


(b)

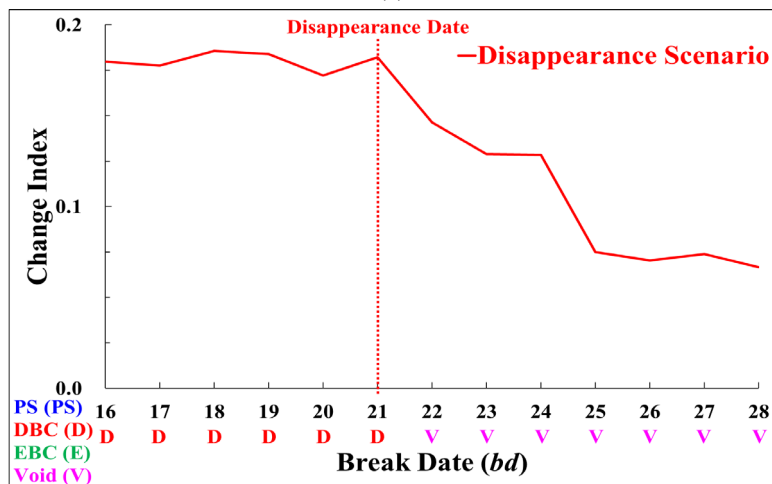
Figure 27: Example of PS point's (a) temporal coherence sequence and (b) chance index sequence along with initial point labels.

So far we have validated our results. Now let's check the behaviours of PS, DBC, and EBC points. Figure 27 displays an example of a PS point, whose temporal coherence 0.93 in the persistence scenario (Figure 3 and Figure 5, all of the images used) fulfils the threshold of 0.8. All of the initial point labels are thus marked as PS. The images taken before and after a break date are used to estimate the temporal coherence for the disappearance and emergence scenarios, respectively. In the disappearance scenario, the temporal coherences along the break date sequence stay averagely 0.92 with a standard deviation of 0.01. The emergence scenario also gives a series of high temporal coherences. The average and standard deviation are 0.93 and 0.02, respectively. Overall, the temporal coherences maintain high without regard to

use of images and break date setting. The change index sequences in both the disappearance and emergence scenarios move around 0, i.e., unlikely a change point. In summary, the characteristics of this PS example conform to our definition of a PS point (Section 3.3).



(a)

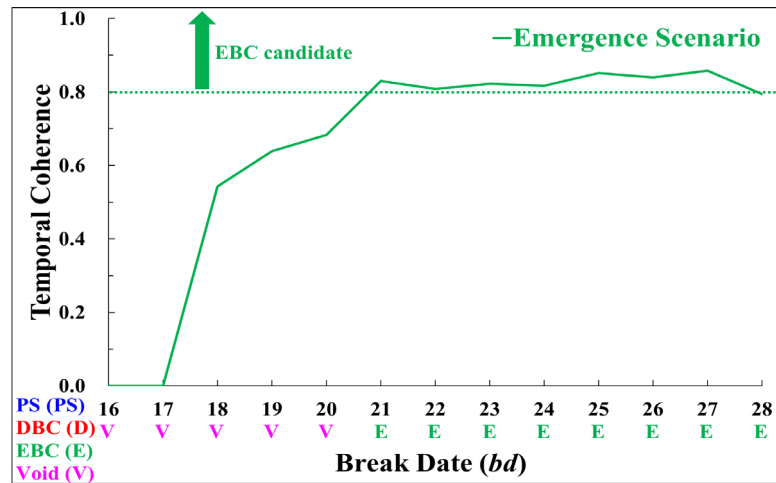


(b)

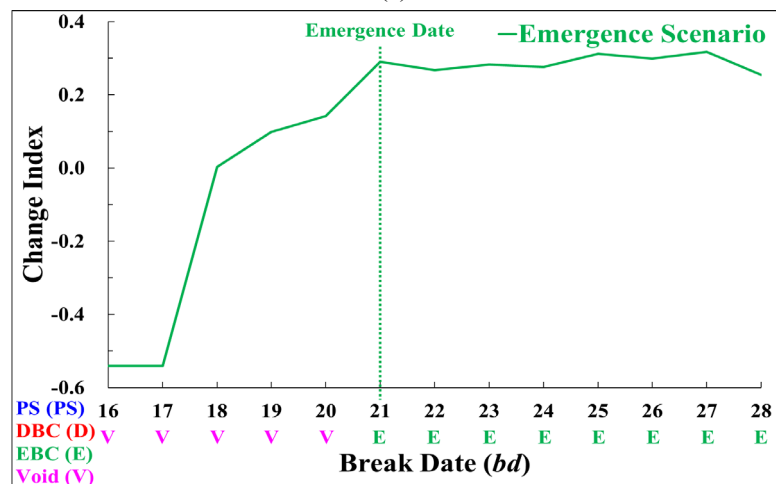
Figure 28: Example of DBC point's (a) temporal coherence sequence and (b) change index sequence along with initial point labels.

The example of a DBC point subject to a disappearance date $bd: 21$ is shown in Figure 28. Since the earliest break date, the temporal coherence series maintain above the threshold of 0.8 but then decrease gradually after $bd: 21$. This behaviour implies a DBC point, which disappeared at $bd: 21$. Therefore, the temporal coherences decline because more and more pure phase noise are involved in coherence estimation. The same trend can be also found in the change index sequence. These change indices are larger than those (Figure 27 (b)) of the PS point. The first five initial point labels are correctly detected as DBC; the others are marked as void because their temporal

coherences do not pass 0.8 to be a DBC candidate (a PS point before disappearance). Our voting method validates this DBC point. The disappearance date (bd : 21) is then identified by locating the turning point of the change index series.



(a)



(b)

Figure 29: Example of EBC point's (a) temporal coherence sequence and (b) change index sequence along with initial point labels.

Figure 29 demonstrates the temporal coherences and change indices of an EBC point, which showed up since the break date bd : 21. Since the beginning, the temporal coherences increase gradually and then keep above 0.8 after the emergence date. The increase can be explained that less and less pure phase noise (before PS emergence) is included in coherence estimation. All of the initial point labels after bd : 20 are EBC because their change indices fulfil the requirements in the detection processing. In contrast, the first five initial labels belong to void rather than EBC as their temporal coherences are below the threshold of 0.8 to be EBC candidates. The voting finally labelled this point as EBC. The detected emergence date (bd : 21) corresponds to the

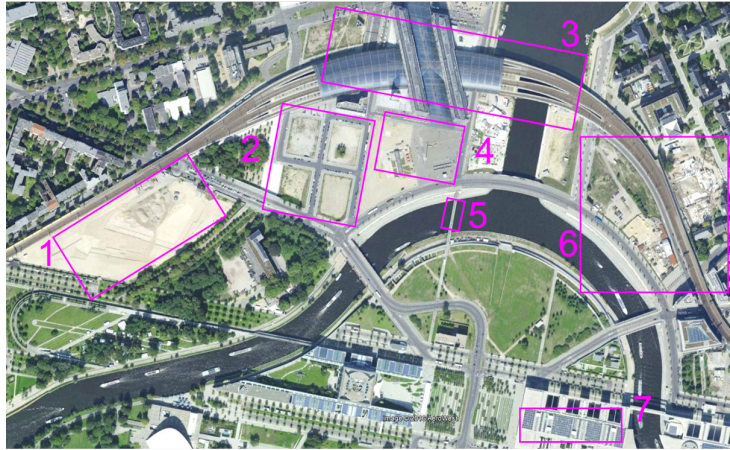
turning point of the change index sequence.

5.5 Urban applications

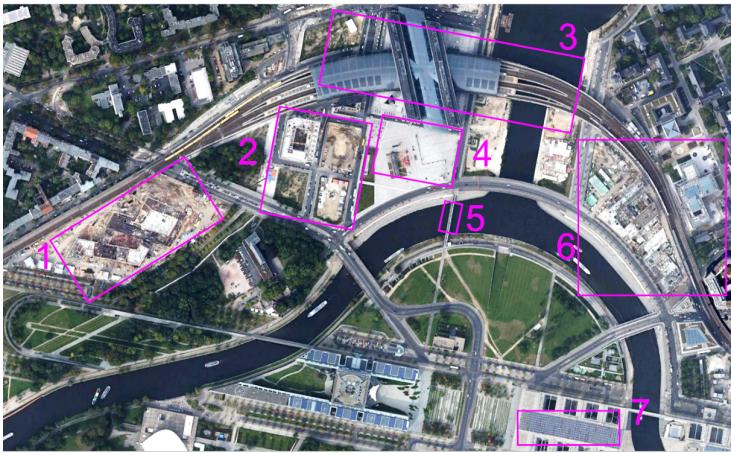
We discuss five examples regarding urban applications based on Google earth images and the spatiotemporal change detection results (patches 2 to 6, Figure 25). First, the construction events around Berlin Central Station are investigated (Figure 30). An office complex (area 1) was constructed in the second half of 2013. Several construction events are shown in area 2. The original structures were removed at the early stage as some DBC points are found around this area. Afterwards, the upper-left hotel was built gradually in 2013. However, the other two new buildings shown on September 5, 2014 (Figure 30 (c)) cannot be detected because their constructions are considered to start later than the detection period, i.e., within 2013. Certain new substructures in areas 3, 4, and 7 are revealed by our method while these changes are hardly perceived from the Google earth images. In area 5, a bridge renovation was carried out during a couple of early months in 2013, which cannot be recognized from the Google earth images. Area 6 displays two new office buildings that were built under different time schedules. The right building was constructed earlier, giving rise to a clear building-shaped pattern of clustered EBC points. By comparison, the construction progress of the left building delayed as only sparse EBC points appeared in late 2013.

The second example (Figure 31) is about monitoring a business district, in which building changes are usually frequent and require cost-effective surveillance schemes. In the early 2013, the buildings in areas 1 and 2 were demolished. Meanwhile, the main structures of the new buildings in areas 3 to 7 were erected; the other parts were built one after another by the end of 2013. Our result shows that certain substructures were added to the office complex in area 8 since the second half of 2013. These additions are hardly perceivable in the Google Earth images.

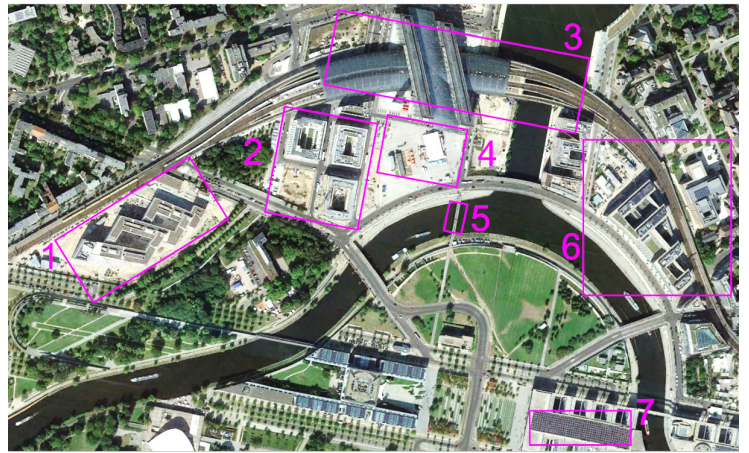
The third example is to monitor sports facilities (Figure 32). Our result indicates that the roof and right-hand side of the arena (area 1) were renovated mostly in early 2013. This renovation cannot be seen from the Google Earth images. A new building (area 3) was erected beside a sports playground nearly the middle 2013. This building was still under construction on September 12, 2010 (Figure 32 (a)) and seemed to be nearly finished on May 20, 2012 (Figure 32 (b)). Some structural changes are found on the stadium (area 2). They are regarded as a renovation event because the DBC and EBC points are mixed.



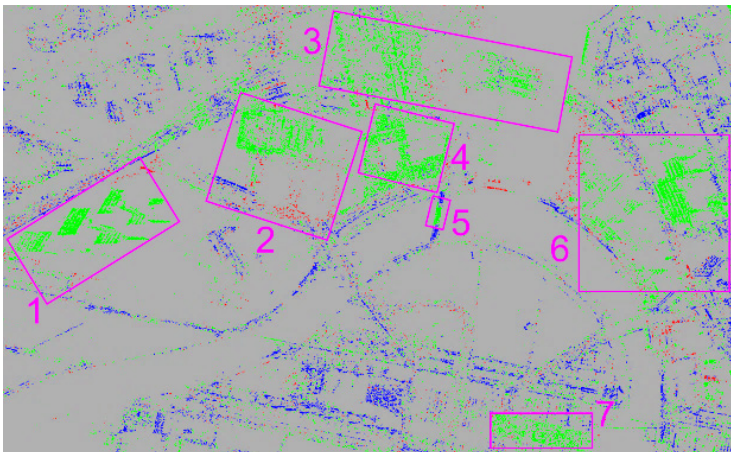
(a)



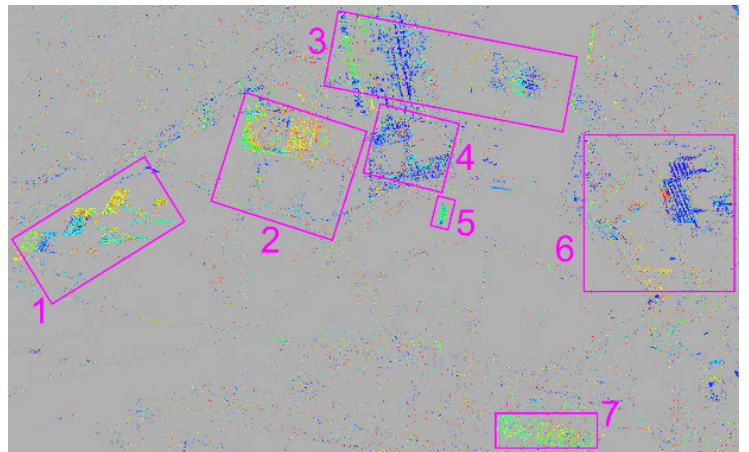
(b)



(c)

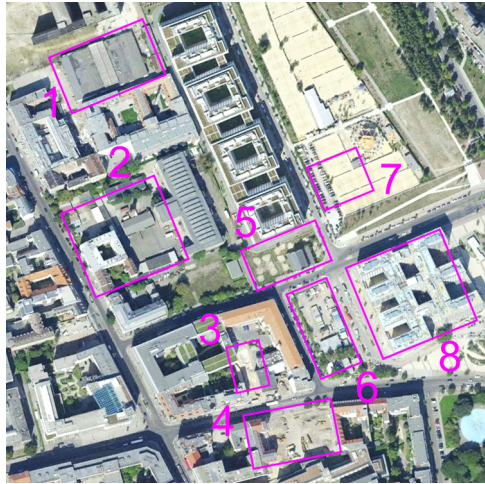


(d)

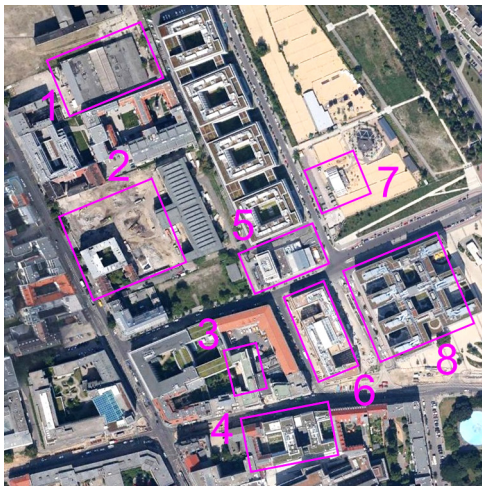


(e)

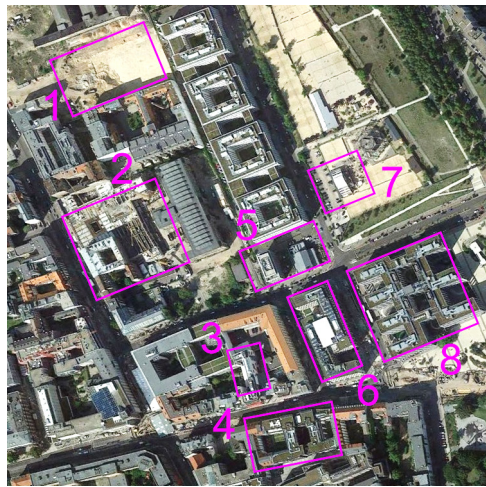
Figure 30: Construction monitoring around Berlin Central Station. Areas 1 to 7 are used for in-depth analysis. Google earth images were acquired on (a) September 12, 2010, (b) May 20, 2012, and (c) September 5, 2014. (d) and (e): spatiotemporal change detection result in patch 2 (Figure 25).



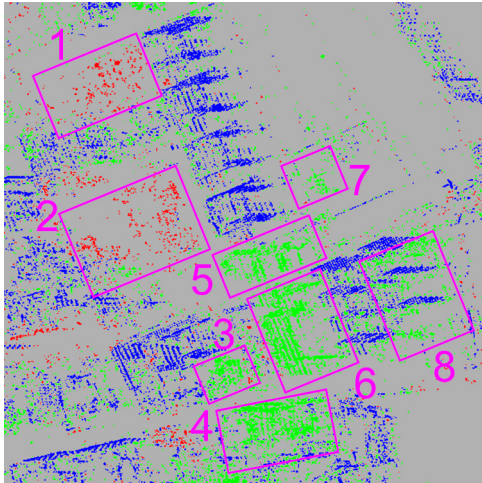
(a)



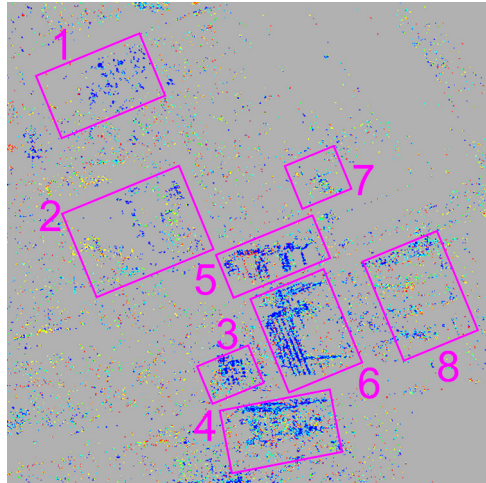
(b)



(c)

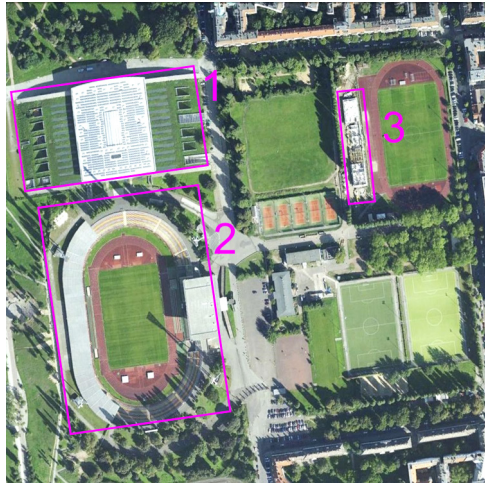


(d)

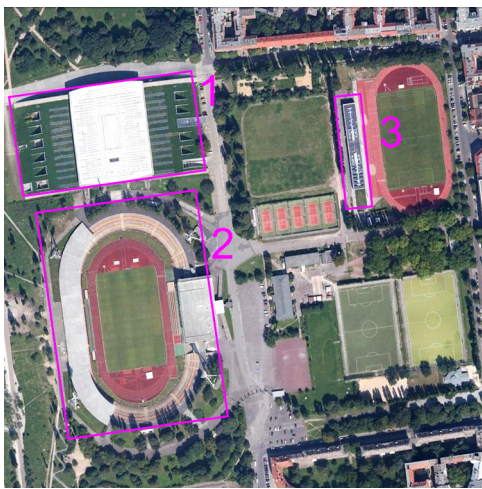


(e)

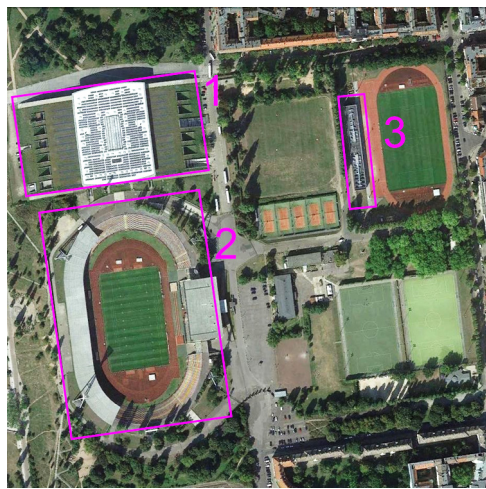
Figure 31: Business district monitoring. Areas 1 to 8 are used for in-depth analysis. Google earth images were acquired on (a) September 12, 2010, (b) May 20, 2012, and (c) September 5, 2014. (d) and (e): spatiotemporal change detection result in patch 3 (Figure 25).



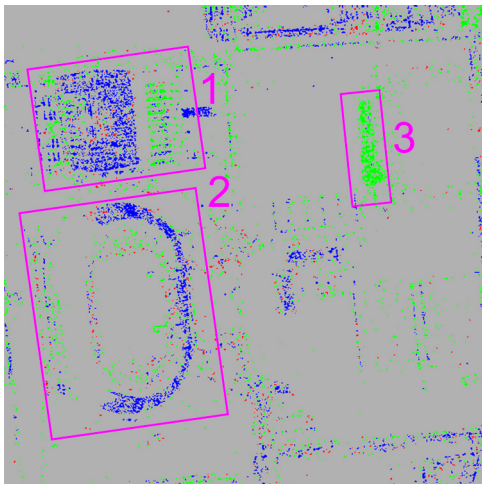
(a)



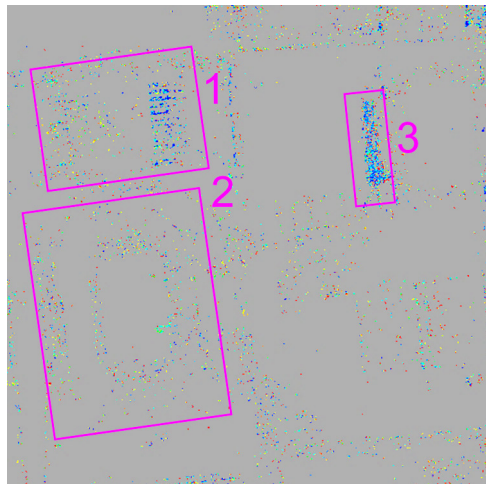
(b)



(c)



(d)



(e)

Figure 32: Sports facility monitoring. Areas 1 and 3 are used for in-depth analysis. Google earth images were acquired on (a) September 12, 2010, (b) May 20, 2012, and (c) September 5, 2014. (d) and (e): spatiotemporal change detection result in patch 4 (Figure 25).

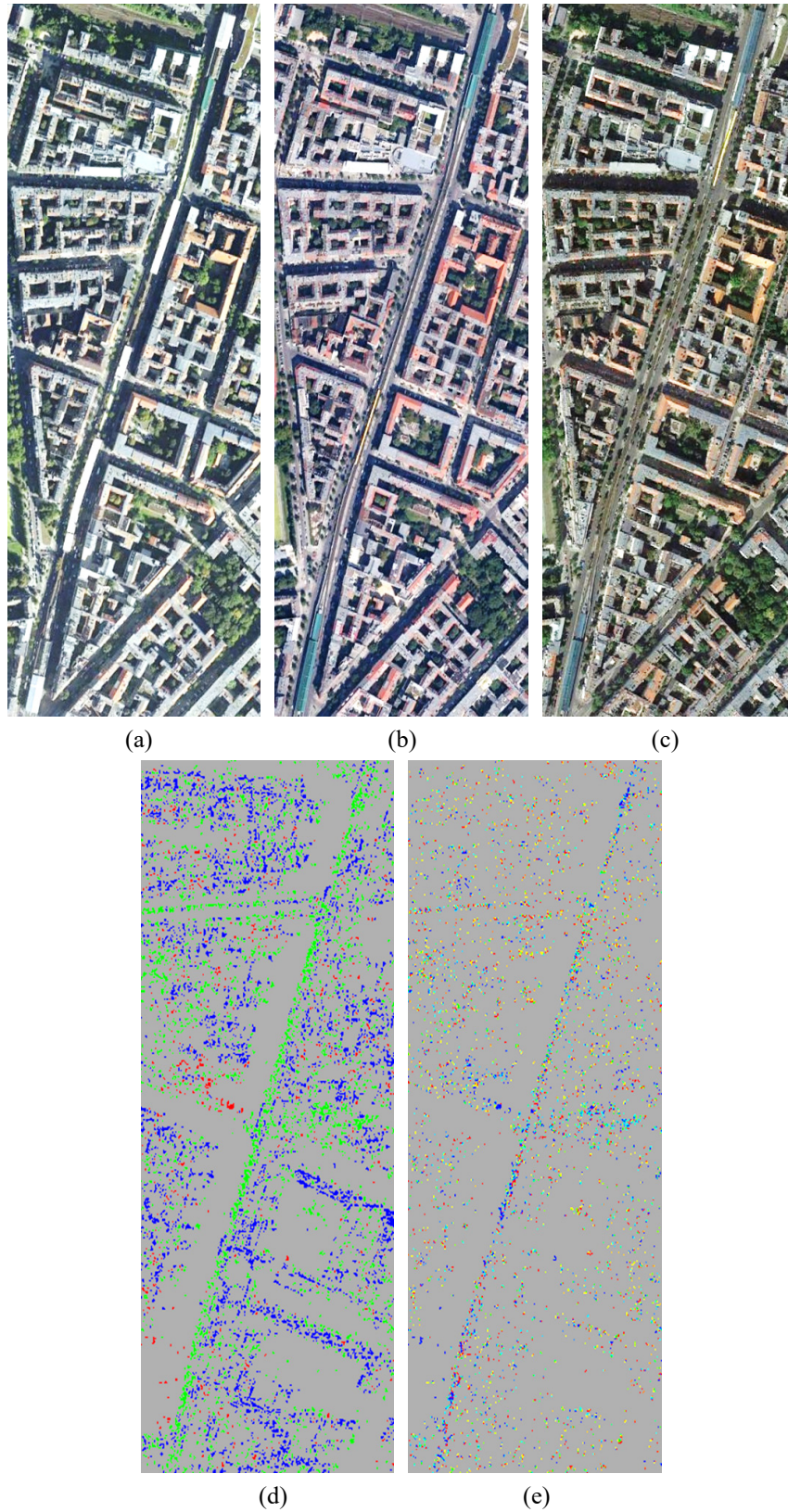
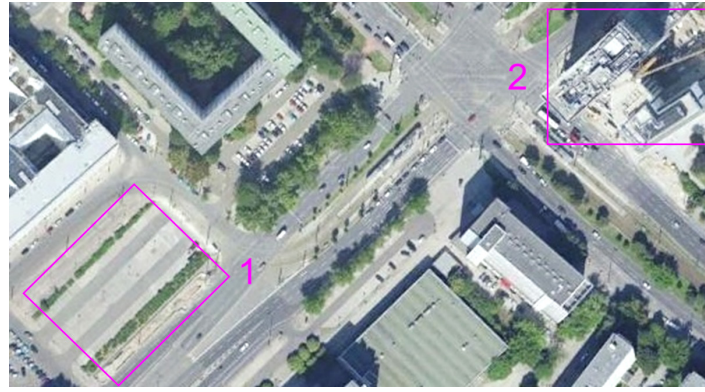
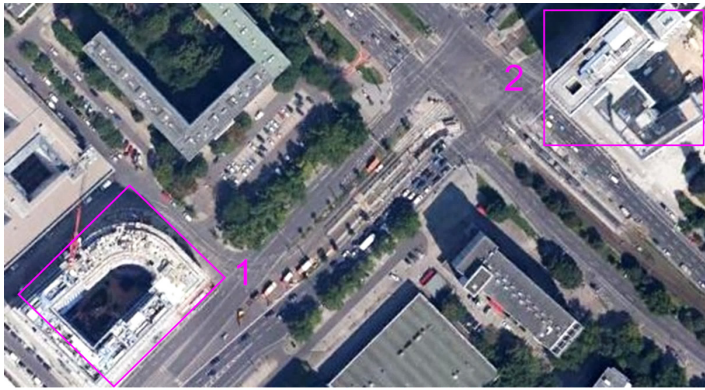


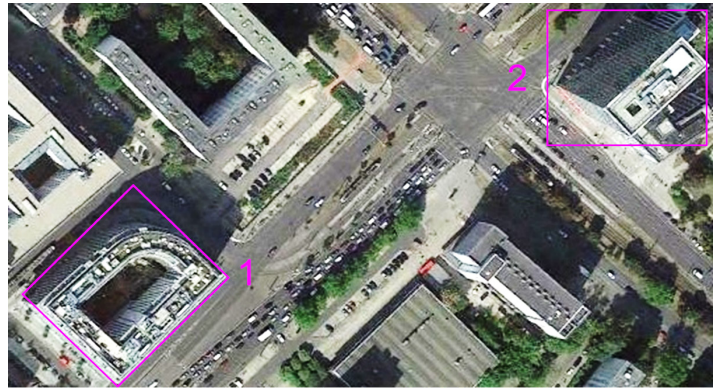
Figure 33: Monitoring of traffic infrastructure. Google earth images were acquired on (a) September 12, 2010, (b) May 20, 2012, and (c) September 5, 2014. (d) and (e): spatiotemporal change detection result in patch 5 (Figure 25).



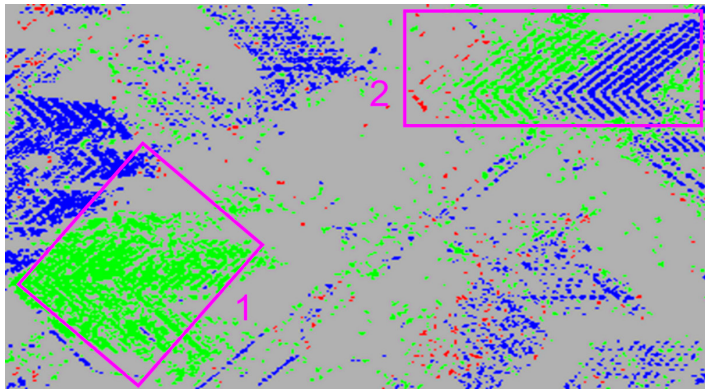
(a)



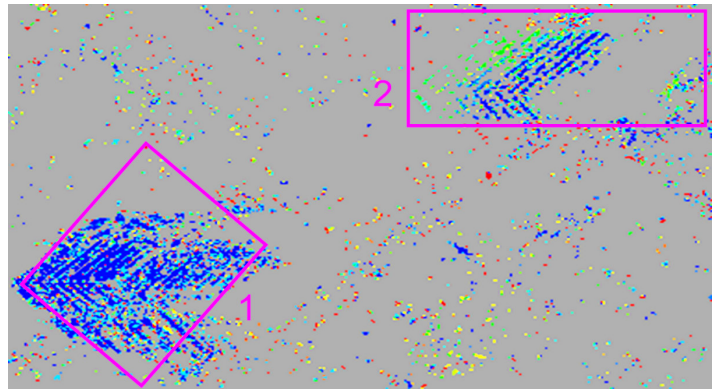
(b)



(c)



(d)



(e)

Figure 34: Construction monitoring of single high-rise buildings (1 and 2). Google earth images were acquired on (a) September 12, 2010, (b) May 20, 2012, and (c) September 5, 2014. (d) and (e): spatiotemporal change detection result in patch 6 (Figure 25).

Monitoring of traffic infrastructure is useful for transportation management especially in busy cities. Our approach discovers a new elevated metro line that was under construction across a couple of blocks in 2013 (Figure 33). The main structure was accomplished in the early stage. The other substructures were later added into it over time. We notice that some canopies were present in 2010 (Figure 33 (a)) but then removed in 2012 (Figure 33 (b)). These changes cannot be identified for now because the break dates (bd : 16 to 28) were set to detect only the changes occurring in 2013. If

the break dates are set before 2013, these roof removals can be detected.

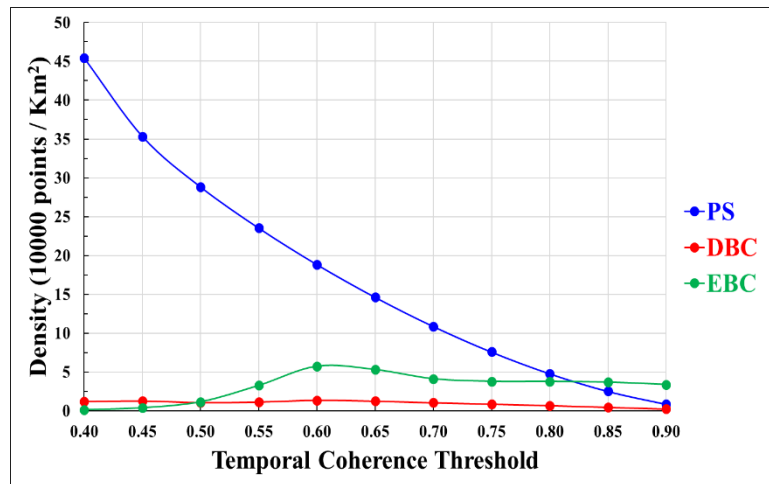
The last example demonstrates a construction monitoring concerning two high-rise buildings (Figure 34). For building 1, a building-like shape is formed from a group of EBC points. Most of them appeared in early 2013 and the others were joined later over time. For this reason, we believe that the main structure was erected in the beginning of 2013 and the construction continued until the end of this year. Intensive PS points, which cluster as a storey-like pattern, account for half of building 2. This means, these storeys has been existing since October, 2010 when the first TerraSAR-X image was acquired (Table II). The new facades (EBC points) were then built upon the old storeys one after another. A handful of DBC points on the top are supposed to be the old materials that were removed before adding parts of the new facades. In conclusion, our technique is able to provide detailed spatiotemporal information about construction progress when focusing on a single event of a certain size.

5.6 Optimal selection of temporal coherence threshold

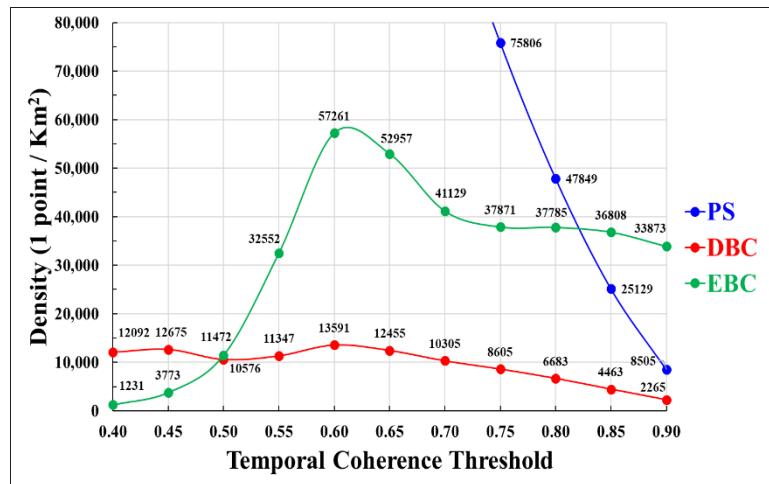
Selection of temporal coherence threshold associates with a trade-off between quality and quantity of PS points. Given a high threshold, we anticipate precise estimates of deformation velocity and object height while the number of PS points is restrained. In addition, we also need to consider different applications and purposes to decide a suitable threshold. For instance, a moderate threshold should be applied to monitoring of volcanic activity to generate an extensive deformation map. In case of a strict threshold used, the sparse and disconnected PS clusters might not deliver complete information for volcanological analysis. In contrast, considering built-up cities covered with intensive corner reflectors, we prefer a high threshold as both the quality and quantity of PS points should satisfy most of the needs. Last but not least, system parameters of SAR sensors, in particular spatial resolution, also influence threshold selection. Generally speaking, high-resolution images increases PS quantity as a small pixel size prevent the coherent signals from being contaminated by the incoherent neighbours. Therefore, we can think of raising the threshold in such a case. In summary, there is no standard answer to an optimal threshold. We must consider actual situations to make an adequate decision.

How to select a suitable threshold in our change detection method becomes even more complicated because we deal with PS and change points at the same time. On the one hand, raising a threshold decreases PS density as expected; on the other hand, the number of change points is reduced or increased? And how about the quality of change

points being detected? Does a stricter threshold lead to more precise change detection? We will answer these questions in the following.



(a)



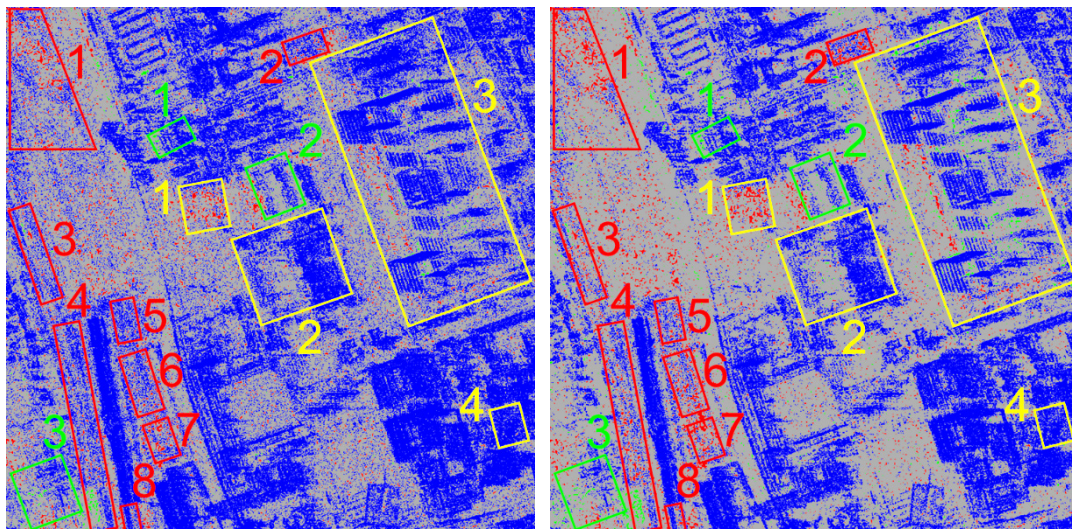
(b)

Figure 35: Point density versus temporal coherence threshold. (a) and (b), small and large scales.

We first discuss the correlation between the temporal coherence thresholds (from 0.4 to 0.9) and the quantities of the PS and change points (Figure 35). The PS density slides down as a smooth quadratic curve when the threshold is raised. In contrast, the DBC density first reaches the maximum at the threshold of 0.6, after which it becomes sparser gradually. We also observe a similar but more drastic course for the EBC density. That is to say, a density of change points tends to decrease if high thresholds are chosen.

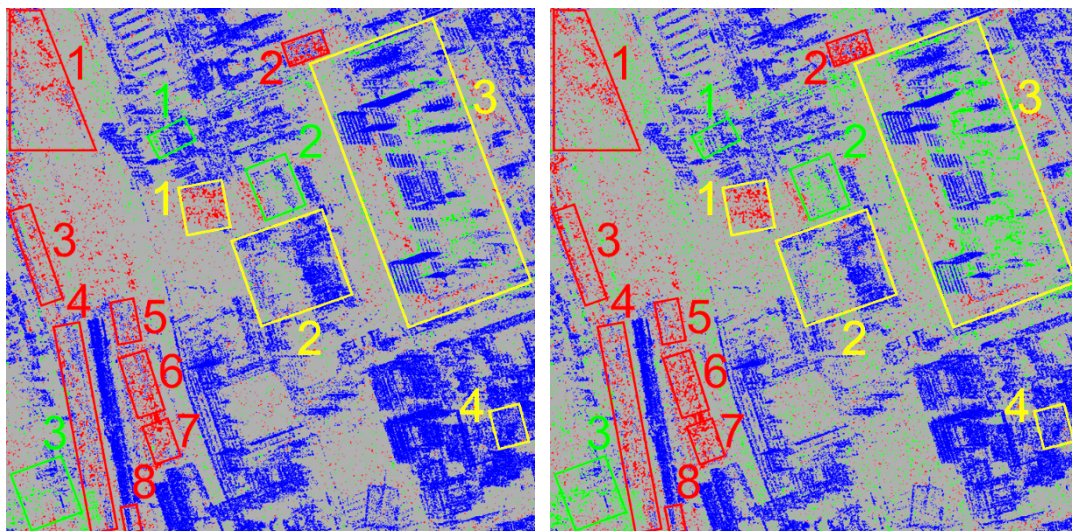
Now we turn to the change detection results of patch 1 (Figure 36) to discuss the accuracy. In the beginning (threshold of 0.4), the scene is overwhelmed by those PS points of low quality, which contradicts our ground truth (Figure 17). As the threshold is increased, the ratio of PS to change points turns reversely. The clustered change

points become more and more while the false PS points are filtered out. This phenomenon illustrates that raising a threshold can identify more authentic PS and change points. However, the cost is to bring more false change points. We see that the extreme example (Figure 36(e), threshold of 0.6) contains the change points everywhere. When the threshold (> 0.6) is set larger and larger, the number of the false change points decreases to some extent; in contrast, more and more correct ones are identified. Although a high threshold seems promising for accuracy, we also notice that the quantity of both the PS and change points is underestimated in particular when the threshold is larger than 0.8. By comparison, the loss of the change points is more restrained. The reason is that our methodology offers more opportunities of being change points, which depends on how many break dates are set. In conclusion, the optimal result in our case comes out with the threshold of 0.8. We suggest this threshold for urban scenes and high-resolution SAR images.



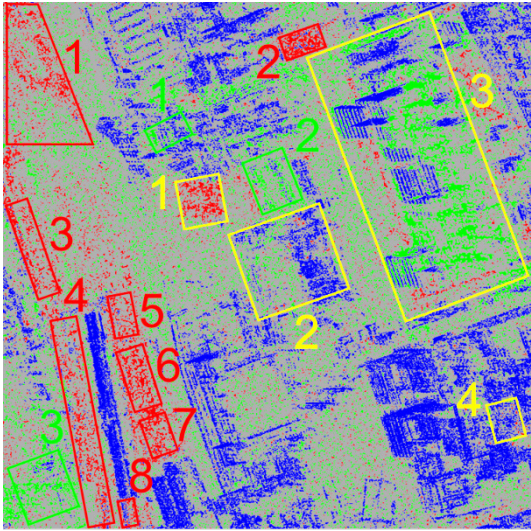
(a) 0.40

(b) 0.45

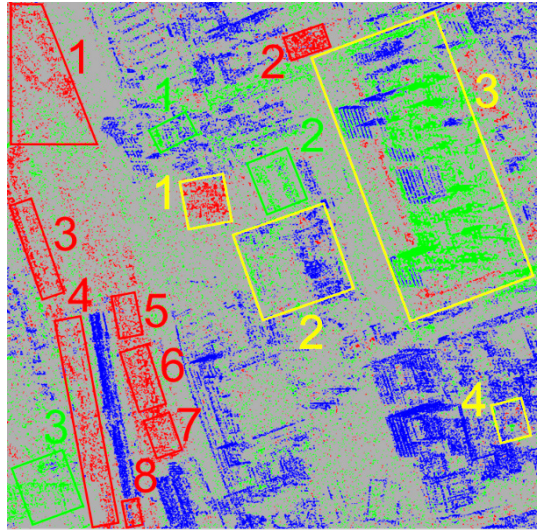


(c) 0.50

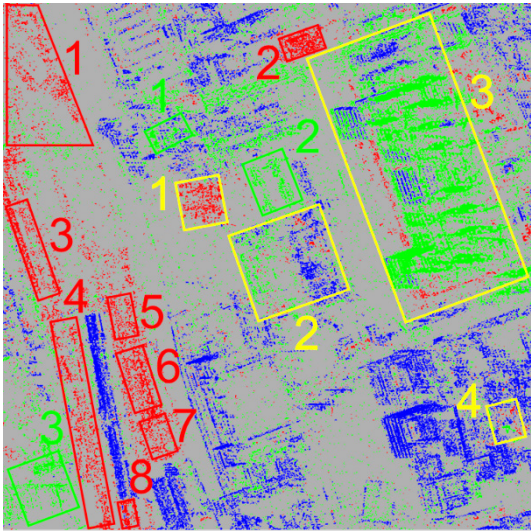
(d) 0.55



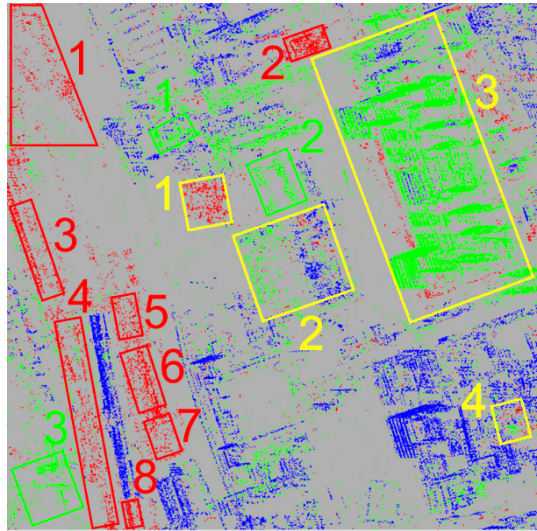
(e) 0.60



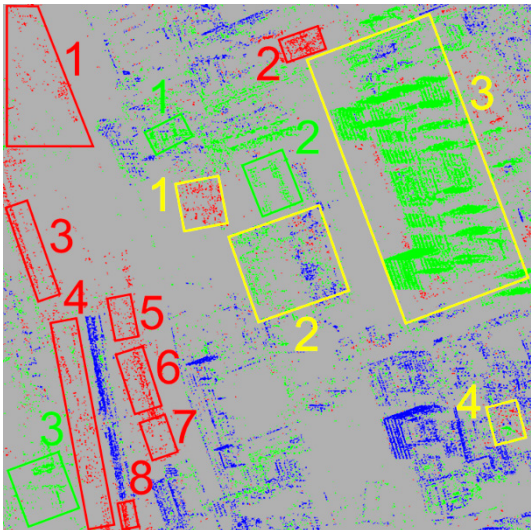
(f) 0.65



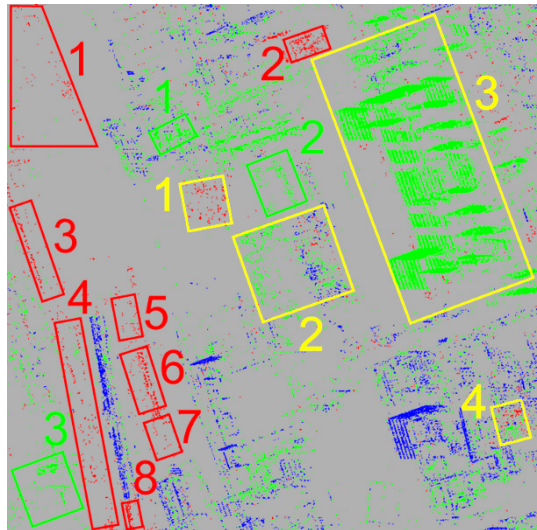
(g) 0.70



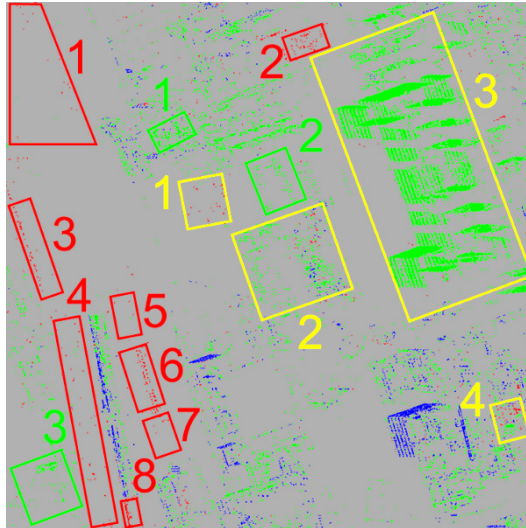
(h) 0.75



(i) 0.80



(j) 0.85



(k) 0.90

Figure 36: Change detection results subject to temporal coherence thresholds (from 0.4 to 0.9) in patch 1 (Figure 25). Building change (ground truth): red, disappearance area; green, emergence area; yellow, complex area.

5.7 Comparison with ratio change detection

We compared our technique with the conventional ratio change detection (Rignot and van Zyl, 1993). For the ratioing method, we chose two images acquired on February 12, 2012 and June 21, 2013 (Table II). During this period many construction events have been confirmed. We first derived two intensity images (dB) from the complex data and divided them by each other. The ratio values of unchanged objects concentrate at 0 as a Gaussian distribution; in contrast, those of changed objects tend towards positives or negatives. Finally, we utilized Otsu thresholding (Otsu, 1979) to extract changes.

We focus our comparison and analysis on patch 1 (Figure 26). The ratio image (Figure 37(a)) manifests the potential changes highlighted by extreme values towards black and red. Among the detected changes (Figure 37(b)) we can identify those clusters subject to changes of interest, i.e., building constructions. However, we also observe salt-and-pepper noise over the scene, which stem from speckle or image noise. Both correct and false results are mixed and therefore lead to difficulty in interpretation. To diminish the impact of speckle, we applied Lee speckle filtering (Lee, 1981b) of size 5×5 to the intensity images before ratioing in the second experiment. The changes due to construction (Figure 38) can be more clearly identified; however, the false alarms, in particular noise, still dominate the result. Finally, we turned to multi-looking by a factor of 100 before ratioing to diminish both speckle and image noise in the intensity images. As a result, most false alarms have been eliminated (Figure 39). Nevertheless, we also

lose spatial details.

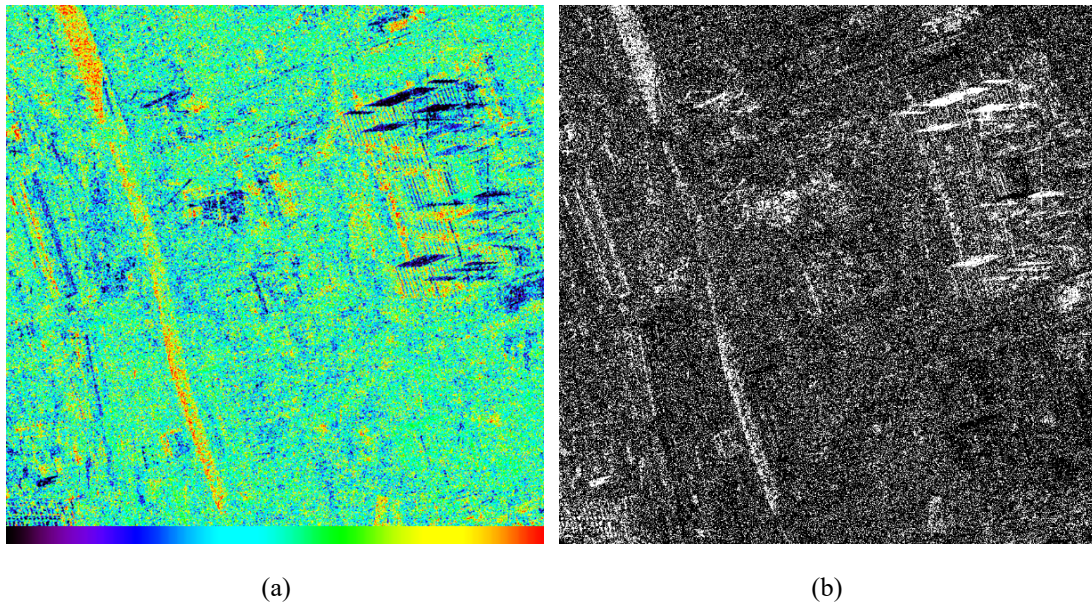


Figure 37: Original example over patch 1 (Figure 16). (a) Ratio image (potential changes towards black and red). (b) Detected changes (white).

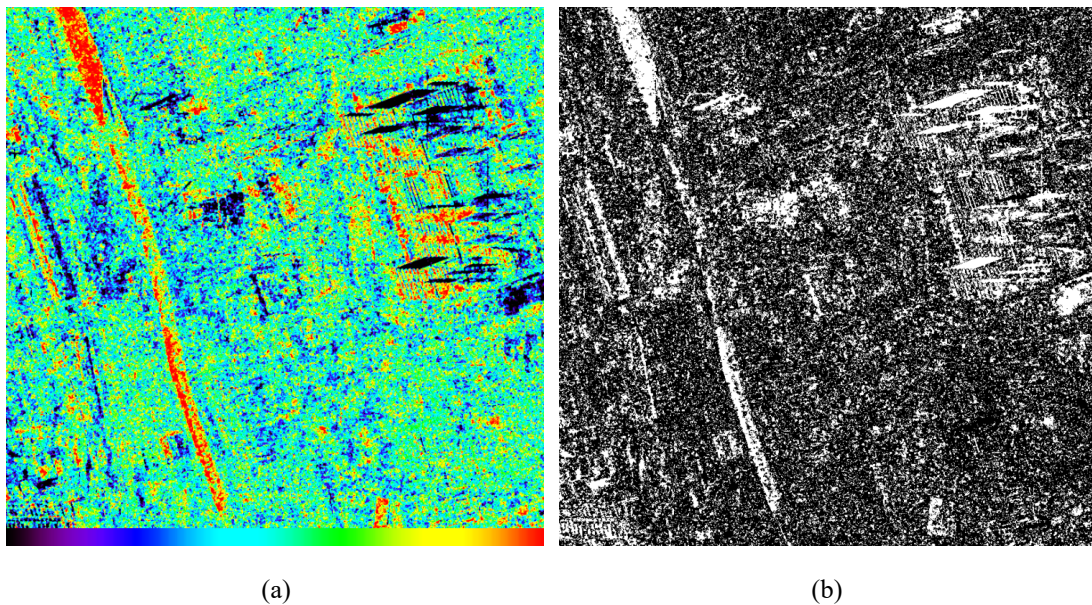


Figure 38: Despeckle example over patch 1 (Figure 16). (a) Ratio image (potential changes towards black and red). (b) Detected changes (white).

The problems mentioned above exist not only for ratio change detection but also for other incoherent approaches. Another common problem is that different change types are not easily discriminated. The strategy of our method looks for disappearance and emergence of PS points. Therefore, we deal with only constructional changes

without disturbance of other change types, speckle, and noise.

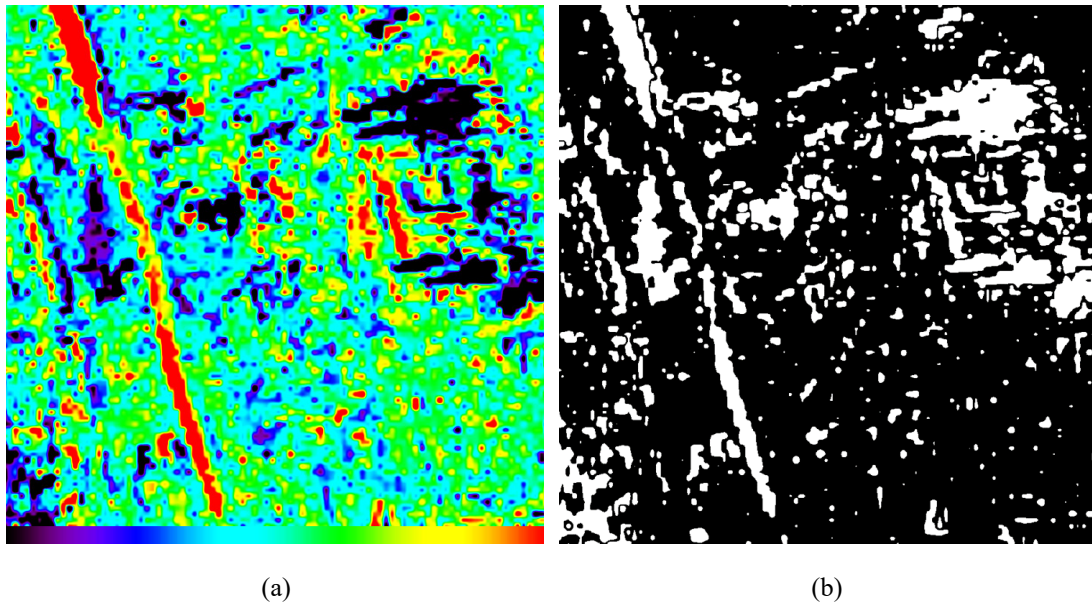


Figure 39: Multi-looking example over patch 1 (Figure 16). (a) Ratio image (potential changes towards black and red). (b) Detected changes (white).

5.8 Comparison with amplitude-based semi-PS method

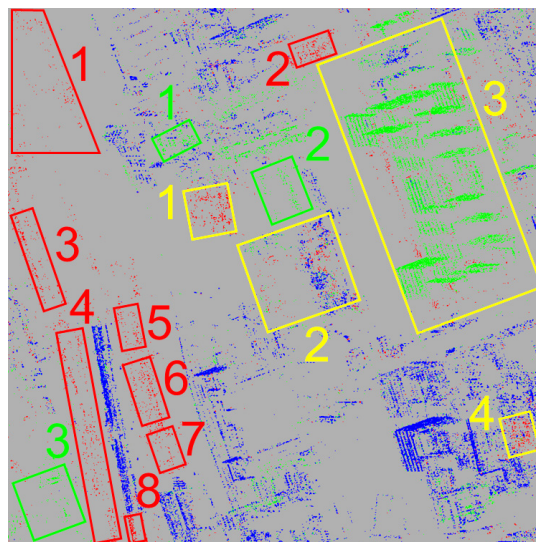


Figure 40: Amplitude-based semi-PS result within patch 1 (Figure 16). Building change (ground truth): red, disappearance area; green, emergence area; yellow, complex area.

We chose an amplitude-based semi-PS method (Ferretti et al., 2003) for comparison with our approach. Only the change points among the thirteen break dates (Table II) were detected and compared. As a result, the DBC and EBC points are

increased by 223% and 498% in our approach. Comparing the patch 1 results (Figure 26 (a) and Figure 40) shows that the amplitude-based result loses partial details or even all the change events. The change points are too few to provide complete information of changes. For example, most of the EBC points are missing in complex area 2, which fails to convey the renovation activity. In addition, the clustered EBC points in complex area 3 becomes very sparse. Compared with an amplitude-based semi-PS method, our approach working on phase information has proven capable of detecting more change points, i.e., more complete information regarding changes.

5.9 Computational requirements

We assess the computational requirements for the proposed approach, which was developed on a computer with Intel Core(TM) i7-5820K, CPU running at 3.30 GHz, and 64GB RAM. The major computational demand is credited to the PSI computations, depending on various parameters. After all of the temporal coherence images were read, the detection process of the PS and change points along with the events' dates was completed within 1 minute.

6. Conclusions

6.1 Summaries

Nowadays, applications using spaceborne SAR images are growing in remote sensing. Both systems and techniques have achieved a remarkable advancement along with launches of modern SAR satellites, e.g., TerraSAR-X (2007 - now) and COSMO-SkyMed (2007 - now). Global industries are also motivated as Sentinel-1 was launched in April, 2014, which provides high-quality and costless images. There are some systems of next generation such as TanDEM-L being planned to be launched in the coming years. The trend is to bring affordable (or costless), accurate, and regular SAR images for global monitoring. We can see a promising perspective for SAR community.

Based on multi-temporal SAR images, PSI is widely utilized in research and commercial fields to monitor structural deformation especially in urban areas. The detectable targets of interest, i.e., PS points, are assumed to move merely from millimetres to centimetres per year and must not undergo big changes like earthquake or demolition. Detecting such big changes resorted to other methodologies and data sources. We saw a potential to extend PSI and use only SAR images for change detection missions.

This study proposes a spatiotemporal change detection to detect spatial big changes along with their occurrence times. Here, the big changes are related to disappearance and emergence of PS points, which are coined as change points. For instance, such change points in urban scenes are realized as substructures, which were removed or newly built under construction. A building-like cluster of change points thus indicate a construction event. We introduce point-based change indices calculated from temporal coherences of multiple image subsets. A change index indicates a probability that a point disappeared or emerged at a specific time period. Instead of using heuristic thresholding, change points are extracted by a statistical data-driven analysis on the change indices. For each change point, the evolution of change indices are then analysed to detect the occurrence time. In practice, the detail level of change points depend on spatiotemporal resolution of SAR images. With the use of TerraSAR-X images, this study identifies the metre-resolution substructures that disappeared or emerged within, the shortest, 11 days. The temporal resolution could be up to 6 days if Sentinel-1 images are utilized; however, loss of spatial details is unavoidable. Our

method is resistive to various kinds of noise because the targets of interest are PS points, which are carefully processed and refined to diminish noise interference. Besides, irrelevant changes other than structural cases like vegetation growth, moving vehicles, temporary activities, etc. are intrinsically excluded. In summary, using only SAR images, our new technique can identify change events, detect their occurrence times, resist noise, and focus on only structural changes.

A simulated data test is realized to validate the methodology in theory. The elements contain 58% PS, 34% change, and 8% void points over a pseudo-developing-city. As a result, the overall accuracy of confusion matrix is 99%. The producer's and user's accuracies for change points are 99%. The accuracy of estimated occurrence dates achieves a sublevel of temporal baseline. For example, given Sentinel-1 images, the temporal accuracy could be less than 6 days (shortest temporal baseline) under optimal conditions, i.e., sufficient images and high-quality PSI results. The spatiotemporal accuracy proves promising but also seems to be overestimated in practice. Note that the data were simulated given ideal PSI processing. Various kinds of noise (except random item) are assumed to be perfectly calibrated or removed. We can say our approach performs very well as long as high PSI accuracy is guaranteed.

Our experiment successfully locates the construction events, which occurred in Berlin in 2013, and detects their occurrence dates. They have been cross-checked with the limited aerial optical images taken at different times. Our approach even catches some events, which are difficult to be recognized from the optical images. Some examples reveal a bridge renovation, a new metro line built across a couple of blocks, certain substructures added to an existing building, and new storeys stacked one after another. The spatiotemporal results are able to interpret the change events in more detail. For instance, whether a construction event started from scratch or was only under renovation. In the latter case, when and which parts were counted. We also see that combining our approach with complementary data brings multi-faceted and explainable results. A typical example is that a new white building was erected following an old grey one at the same place. The position and time of this construction activity are provided in our change detection result. The optical images show that its color was changed from grey to white.

A temporal coherence threshold plays a crucial role in PSI and our method. For PSI, a threshold is chosen considering a trade-off between quality and quantity of PS points. There is no absolute principle to determine a best threshold. We must consider the needs, requirements, and applications to decide a suitable threshold. This decision

becomes even more complicated in our approach, by which both PS and change points are detected. We thoroughly investigated the number and accuracy of PS and change points subject to different thresholds from low to high. In principle, a higher threshold above a certain level leads to a more accurate result and less false negatives; however, the true points might be overly filtered out. Based on our tests, we suggest using threshold of 0.8 for urban scenes and high-resolution SAR images.

For comparison, we also made tests using classical image ratioing and amplitude-based semi-PS approach to identify building changes. As expected, image ratioing highlights and extracts not only the building changes of interest but also image noise and other change types. The latter items were suppressed by speckle filtering and multi-looking, which causes loss of spatial detail. In addition, irrelevant changes need additional efforts and data sources to be separated. To some extent the abovementioned difficulties were overcome in the amplitude-based semi-PS result. The concept of the amplitude-based semi-PS method is similar to our proposed methodology. The major difference is that the former and latter utilize amplitudes and phases of SAR images, respectively, to detect change points. As a result, our technique has proven capable of detecting more change points, i.e., more complete information regarding change events.

The computational demand is divided into two parts. The heavier part is credited to PSI processes, each of which takes hours to days or even longer depending on the size of data and various PSI-related parameters. The second part belongs to change detection step (our main contribution) and only takes minutes after inputs generated by PSI are read. We have seen two prospects for time-consuming PSI to improve efficiency. First, the computing power of CPU always keeps increasing to the future. With advanced techniques, e.g., parallel computing, we believe that the time required for PSI computation will be significantly shortened to enable our approach to be near real-time or even real-time monitoring. Second, the PSI procedure can be simplified if accurate complementary data and a priori information are available. For example, deformation velocities and residual heights, which are usually estimated in PSI, can be preset to null if the areas of interest are steady and accurate topography data are available. This preset dramatically reduces computing times.

Our method is particularly suitable to monitor built-up areas where lots of PS and change points, if any, can be found. For instance, we can distinguish destroyed buildings and damaged substructures due to natural disasters, such as earthquake, from other structural changes taking place before. The subsequent reconstruction can then be monitored as well. As mentioned before, only structural changes can be detected but

what kinds of them, e.g., facades, roofs, houses, offices, factories, or infrastructures? We can use GIS-based information, like 3D city models or topic maps, to label the change points and bring semantic products. For this purpose, points can be first clustered and segmented depending on their properties such as labels, spatial proximity, occurrence times, geometry, homogeneity, temporal coherences, and so on. A potential application is to adapt the proposed approach for DS points. This adapted version enables changes on natural objects, such as rocky terrain overwhelmed by magma, to be detected.

6.2 Future works

We have four plans for the future. First, we will conduct more case studies to explore the proposed method's parameters, potentials, and applications. Second, a technical extension will be to combine the current method with other complementary data, e.g., SAR amplitude images, to improve its performance. Third, our technique can be upgraded to detect a new change point label, which undergoes double big changes during a time period. For instance, a new building is erected soon, following a demolition event. For this purpose, a pixel will be further analysed if its initial point labels contain different change types. Finally, our approach can be adapted to detect underground big changes like tunnelling. Normally such events speed up deformation velocities of PS points upon the surface. Initially, we derived a new kind of change index from variation of PS velocities subject to a set of break dates. However, our test showed that the change indices are insensitive to the underground activities of interest, which causes a large number of missed detections. Not to mention it is unable to find out the accurate occurrence times. For improvement, a possible way is to look for abrupt changes along a time series of displacement for each PS point.

Bibliography

- Adam, N., Kampes, B., Eineder, M., Worawattanamateekul, J., Kircher, M., 2003. The Development of A Scientific Permanent Scatterer System, in: ISPRS Workshop. Hannover, Germany.
- Amelung, F., Galloway, D.L., Bell, J.W., Zebker, H.A., Lacznia, R.J., 1999. Sensing The Ups and Downs of Las Vegas: InSAR Reveals Structural Control of Land Subsidence and Aquifer-system Deformation. *Geology*, 27(6), 483–486.
- Ansari, H., Adam, N., Brcic, R., 2014. Amplitude Time Series Analysis in Detection of Persistent and Temporal Coherent Scatterers, in: 2014 IEEE International Geoscience and Remote Sensing Symposium. IEEE, Quebec, Canada, pp. 2213–2216.
- Antonielli, B., Monserrat, O., Bonini, M., Righini, G., Sani, F., Luzi, G., Feyzullayev, A.A., Aliyev, C.S., 2014. Pre-eruptive Ground Deformation of Azerbaijan Mud Volcanoes Detected through Satellite Radar Interferometry (DInSAR). *Tectonophysics*, 637, 163–177.
- Askne, J.I.H., Dammert, P.B.G., Ulander, L.M.H., Smith, G., 1997. C-band Repeat-pass Interferometric SAR Observations of The Forest. *IEEE Trans. Geosci. Remote Sens.*, 35(1), 25–35.
- Balz, T., Liao, M., 2010. Building-damage Detection Using Post-seismic High-resolution SAR Satellite Data. *Int. J. Remote Sens.*, 31(13), 3369–3391.
- Bamler, R., Eineder, M., Adam, N., Zhu, X., Gernhardt, S., 2009. Interferometric Potential of High Resolution Spaceborne SAR. *Photogramm. - Fernerkundung - Geoinf.*, 2009(5), 407–419.
- Bamler, R., Hartl, P., 1998. Synthetic aperture radar interferometry. *Inverse Probl.*, 14(4), R1–R54.
- Bazi, Y., Bruzzone, L., Melgani, F., 2005. An Unsupervised Approach Based on The Generalized Gaussian Model to Automatic Change Detection in Multitemporal SAR Images. *IEEE Trans. Geosci. Remote Sens.*, 43(4), 874–887.
- Berardino, P., Fornaro, G., Lanari, R., Sansosti, E., 2002. A New Algorithm for Surface Deformation Monitoring Based on Small Baseline Differential SAR Interferograms. *IEEE Trans. Geosci. Remote Sens.*, 40(11), 2375–2383.
- Bonano, M., Manunta, M., Pepe, A., Paglia, L., Lanari, R., 2013. From Previous C-Band to New X-Band SAR Systems: Assessment of The DInSAR Mapping Improvement for Deformation Time-Series Retrieval in Urban Areas. *IEEE Trans. Geosci. Remote Sens.*, 51(4), 1973–1984.
- Bovenga, F., Wasowski, J., Nitti, D.O., Nutricato, R., Chiaradia, M.T., 2012. Using

- COSMO/SkyMed X-band and ENVISAT C-band SAR Interferometry for Landslides Analysis. *Remote Sens. Environ.*, 119, 272–285.
- Bovolo, F., Bruzzone, L., 2005. A Detail-preserving Scale-driven Approach to Change Detection in Multitemporal SAR Images. *IEEE Trans. Geosci. Remote Sens.*, 43(12), 2963–2972.
- Brcic, R., Adam, N., 2013. Detecting Changes in Persistent Scatterers, in: 2013 IEEE International Geoscience and Remote Sensing Symposium. IEEE, Melbourne, Australia, pp. 117–120.
- Brenner, A.R., Roessing, L., 2008. Radar Imaging of Urban Areas by Means of Very High-resolution SAR and Interferometric SAR. *IEEE Trans. Geosci. Remote Sens.*, 46(10), 2971–2982.
- Brett, P.T.B., Guida, R., 2013. Earthquake Damage Detection in Urban Areas Using Curvilinear Features. *IEEE Trans. Geosci. Remote Sens.*, 51(9), 4877–4884.
- Brunner, D., Lemoine, G., Bruzzone, L., 2010. Earthquake Damage Assessment of Buildings Using VHR Optical and SAR Imagery. *IEEE Trans. Geosci. Remote Sens.*, 48(5), 2403–2420.
- Bruzzone, L., Bovolo, F., 2013. A Novel Framework for The Design of Change-detection Systems for Very-high-resolution Remote Sensing Images. *Proc. IEEE*, 101(3), 609–630.
- Bruzzone, L., Marconcini, M., Wegmuller, U., Wiesmann, A., 2004. An Advanced System for The Automatic Classification of Multitemporal SAR Images. *IEEE Trans. Geosci. Remote Sens.*, 42(6), 1321–1334.
- Cao, N., Lee, H., Jung, H.C., 2016. A Phase-decomposition-based PSInSAR Processing Method. *IEEE Trans. Geosci. Remote Sens.*, 54(2), 1074–1090.
- Carnec, C., Massonnet, D., King, C., 1996. Two Examples of The Use of SAR Interferometry on Displacement Fields of Small Spatial Extent. *Geophys. Res. Lett.*, 23(24), 3579–3582.
- Chang, L., Hanssen, R.F., 2016. A Probabilistic Approach for InSAR Time-Series Postprocessing. *IEEE Trans. Geosci. Remote Sens.*, 54(1), 421–430.
- Chini, M., Pierdicca, N., Emery, W.J., 2009. Exploiting SAR and VHR Optical Images to Quantify Damage Caused by The 2003 Bam Earthquake. *IEEE Trans. Geosci. Remote Sens.*, 47(1), 145–152.
- Colesanti, C., Ferretti, A., Novali, F., Prati, C., Rocca, F., 2003. Sar Monitoring of Progressive and Seasonal Ground Deformation Using The Permanent Scatterers Technique. *IEEE Trans. Geosci. Remote Sens.*, 41(7), 1685–1701.
- Costantini, M., 1998. A Novel Phase Unwrapping Method Based on Network Programming. *IEEE Trans. Geosci. Remote Sens.*, 36(3), 813–821.
- Costantini, M., Falco, S., Malvarosa, F., Minati, F., 2008. A New Method for

- Identification and Analysis of Persistent Scatterers in Series of SAR Images, in: 2008 IEEE International Geoscience and Remote Sensing Symposium. IEEE, Boston, United States of America.
- Costantini, M., Rosen, P.A., 1999. A Generalized Phase Unwrapping Approach for Sparse Data, in: IEEE 1999 International Geoscience and Remote Sensing Symposium. IEEE, Hamburg, Germany, pp. 267–269.
- Crosetto, M., Arnaud, A., Duro, J., Biescas, E., Agudo, M., 2003. Deformation Monitoring Using Remotely Sensed Radar Interferometric Data, in: 11th FIG Symposium. Santorini, Greece.
- Crosetto, M., Biescas, E., Duro, J., Closa, J., Arnaud, A., 2008. Generation of Advanced ERS and Envisat Interferometric SAR Products Using The Stable Point Network Technique. *Photogramm. Eng. Remote Sens.*, 74(4), 443–450.
- Crosetto, M., Crippa, B., Biescas, E., 2005. Early Detection and In-depth Analysis of Deformation Phenomena by Radar Interferometry. *Eng. Geol.*, 79(1–2), 81–91.
- Crosetto, M., Monserrat, O., Cuevas-González, M., Devanthery, N., Crippa, B., 2016. Persistent Scatterer Interferometry: A review. *ISPRS J. Photogramm. Remote Sens.*, 115, 78–89.
- Crosetto, M., Monserrat, O., Cuevas-González, M., Devanthery, N., Luzi, G., Crippa, B., 2015. Measuring Thermal Expansion Using X-band Persistent Scatterer Interferometry. *ISPRS J. Photogramm. Remote Sens.*, 100, 84–91.
- Curlander, J.C., McDonough, R.N., 1991. *Synthetic Aperture Radar: Systems and Signal Processing*. Wiley, New York, United States of America.
- Dalla Via, G., Crosetto, M., Crippa, B., 2012. Resolving Vertical and East-west Horizontal Motion from Differential Interferometric Synthetic Aperture Radar: The L'Aquila Earthquake. *J. Geophys. Res.*, 117(B2).
- Dekker, R.J., 2011. High-resolution Radar Damage Assessment after The Earthquake in Haiti on 12 January 2010. *IEEE J. Sel. Top. Appl. Earth Obs. Remote Sens.*, 4(4), 960–970.
- Dell'Acqua, F., Bignami, C., Chini, M., Lisini, G., Polli, D.A., Stramondo, S., 2011. Earthquake Damages Rapid Mapping by Satellite Remote Sensing Data: L'Aquila April 6th, 2009 Event. *IEEE J. Sel. Top. Appl. Earth Obs. Remote Sens.*, 4(4), 935–943.
- Dong, Y., Forster, B., Ticehurst, C., 1997. Radar Backscatter Analysis for Urban Environments. *Int. J. Remote Sens.*, 18(6), 1351–1364.
- Dong, Y., Li, Q., Dou, A., Wang, X., 2011. Extracting Damages Caused by The 2008 Ms 8.0 Wenchuan Earthquake from SAR Remote Sensing Data. *J. Asian Earth Sci.*, 40(4), 907–914.
- Duro, J., Inglada, J., Closa, J., Adam, N., Arnaud, A., 2003. High Resolution

- Differential Interferometry Using Time Series of ERS and ENVISAT SAR Data, in: FRINGE 2003. Frascati, Italy.
- Ehrlich, D., Guo, H.D., Molch, K., Ma, J.W., Pesaresi, M., 2009. Identifying Damage Caused by The 2008 Wenchuan Earthquake from VHR Remote Sensing Data. *Int. J. Digit. Earth*, 2(4), 309–326.
- Esmaeili, M., Motagh, M., 2016. Improved Persistent Scatterer Analysis Using Amplitude Dispersion Index Optimization of Dual Polarimetry Data. *ISPRS J. Photogramm. Remote Sens.*, 117, 108–114.
- Ferretti, A., Colesanti, C., Perissin, D., Prati, C., Rocca, F., 2003. Evaluating The Effect of The Observation Time on The Distribution of SAR Permanent Scatterers, in: FRINGE 2003. Frascati, Italy.
- Ferretti, A., Fumagalli, A., Novali, F., Prati, C., Rocca, F., Rucci, A., 2011. A New Algorithm for Processing Interferometric Data-Stacks: SqueeSAR. *IEEE Trans. Geosci. Remote Sens.*, 49(9), 3460–3470.
- Ferretti, A., Perissin, D., Prati, C., Rocca, F., 2005. On The Physical Nature of SAR Permanent Scatterers, in: URSI Commission Symposium on Microwave Remote Sensing of the Earth, Oceans, Ice, and Atmosphere. Ispra, Italy.
- Ferretti, A., Prati, C., Rocca, F., 2000. Nonlinear Subsidence Rate Estimation Using Permanent Scatterers in Differential SAR Interferometry. *IEEE Trans. Geosci. Remote Sens.*, 38(5), 2202–2212.
- Ferretti, A., Prati, C., Rocca, F., 2001. Permanent Scatterers in SAR Interferometry. *IEEE Trans. Geosci. Remote Sens.*, 39(1), 8–20.
- Ferretti, A., Savio, G., Barzaghi, R., Borghi, A., Musazzi, S., Novali, F., Prati, C., Rocca, F., 2007. Submillimeter Accuracy of InSAR Time Series: Experimental Validation. *IEEE Trans. Geosci. Remote Sens.*, 45(5), 1142–1153.
- Fornaro, G., Pauciuolo, A., Reale, D., 2011. A Null-Space Method for The Phase Unwrapping of Multitemporal SAR Interferometric Stacks. *IEEE Trans. Geosci. Remote Sens.*, 49(6), 2323–2334.
- Franceschetti, G., Iodice, A., Riccio, D., 2002. A Canonical Problem in Electromagnetic Backscattering from Buildings. *IEEE Trans. Geosci. Remote Sens.*, 40(8), 1787–1801.
- Gabriel, A.K., Goldstein, R.M., Zebker, H.A., 1989. Mapping Small Elevation Changes over Large Areas: Differential Radar Interferometry. *J. Geophys. Res.*, 94(B7), 9183–9191.
- Galloway, D.L., Hudnut, K.W., Ingebritsen, S.E., Phillips, S.P., Peltzer, G., Rogez, F., Rosen, P.A., 1998. Detection of Aquifer System Compaction and Lland Subsidence Using Interferometric Synthetic Aperture Radar, Antelope Valley, Mojave Desert, California. *Water Resour. Res.*, 34(10), 2573–2585.

- Gamba, P., 2013. Human Settlements: A Global Challenge for EO Data Processing and Interpretation. *Proc. IEEE*, 101(3), 570–581.
- García-Davalillo, J.C., Herrera, G., Notti, D., Strozzi, T., Álvarez-Fernández, I., 2014. DInSAR Analysis of ALOS PALSAR Images for The Assessment of Very Slow Landslides: The Tena Valley Case Study. *Landslides*, 11(2), 225–246.
- Gens, R., Van Genderen, J.L., 1996. SAR interferometry - Issues, Techniques, Applications. *Int. J. Remote Sens.*, 17(10), 1803–1835.
- Gernhardt, S., Adam, N., Eineder, M., Bamler, R., 2010. Potential of Very High Resolution SAR for Persistent Scatterer Interferometry in Urban Areas. *Ann. GIS*, 16(2), 103–111.
- Gernhardt, S., Auer, S., Eder, K., 2015. Persistent Scatterers at Building Facades – Evaluation of Appearance and Localization Accuracy. *ISPRS J. Photogramm. Remote Sens.*, 100, 92–105.
- Gernhardt, S., Bamler, R., 2012. Deformation Monitoring of Single Buildings Using Meter-resolution SAR Data in PSI. *ISPRS J. Photogramm. Remote Sens.*, 73, 68–79.
- Ghiglia, D.C., Pritt, M.D., 1998. Two-dimensional Phase Unwrapping: Theory, Algorithms, and Software. Wiley, New York, United States of America.
- Gisinger, C., Balss, U., Pail, R., Zhu, X.X., Montazeri, S., Gernhardt, S., Eineder, M., 2015. Precise Three-dimensional Stereo Localization of Corner Reflectors and Persistent Scatterers with TerraSAR-X. *IEEE Trans. Geosci. Remote Sens.*, 53(4), 1782–1802.
- Goel, K., Adam, N., 2014. A Distributed Scatterer Interferometry Approach for Precision Monitoring of Known Surface Deformation Phenomena. *IEEE Trans. Geosci. Remote Sens.*, 52(9), 5454–5468.
- Goldstein, R.M., Engelhardt, H., Kamb, B., Frolich, R.M., 1993. Satellite Radar Interferometry for Monitoring Ice Sheet Motion: Application to An Antarctic Ice Stream. *Science*, 262(5139), 1525–1530.
- Goldstein, R.M., Zebker, H.A., Werner, C.L., 1988. Satellite Radar Interferometry: Two-dimensional Phase Unwrapping. *Radio Sci.*, 23(4), 713–720.
- Golub, G.H., Van Loan, C.F., 1996. *Matrix Computations*. The Johns Hopkins University Press, Baltimore, United States of America.
- Gong, M., Yang, H., Zhang, P., 2017. Feature Learning and Change Feature Classification Based on Deep Learning for Ternary Change Detection in SAR Images. *ISPRS J. Photogramm. Remote Sens.*, 129, 212–225.
- Hall, O., Hay, G.J., 2003. A Multiscale Object-Specific Approach to Digital Change Detection. *Int. J. Appl. Earth Obs. Geoinf.*, 4(4), 311–327.
- Hanssen, R.F., 2001. *Radar Interferometry - Data Interpretation and Error Analysis*,

- Remote Sensing and Digital Image Processing. Springer, Dordrecht, The Netherlands.
- Hetland, E.A., Musé, P., Simons, M., Lin, Y.N., Agram, P.S., DiCaprio, C.J., 2012. Multiscale InSAR Time Series (MInTS) Analysis of Surface Deformation. *J. Geophys. Res.*, 117(B2).
- Hooper, A., 2008. A multi-temporal InSAR Method Incorporating Both Persistent Scatterer and Small Baseline Approaches. *Geophys. Res. Lett.*, 35(16), L16302.
- Hooper, A., Zebker, H., Segall, P., Kampes, B., 2004. A New Method for Measuring Deformation on Volcanoes and Other Natural Terrains Using InSAR Persistent Scatterers. *Geophys. Res. Lett.*, 31(23).
- Hooper, A., Zebker, H.A., 2007. Phase Unwrapping in Three Dimensions with Application to InSAR Time Series. *J. Opt. Soc. Am. A*, 24(9), 2737–2747.
- Huang, Q., Crosetto, M., Monserrat, O., Crippa, B., 2017. Displacement Monitoring and Modelling of a High-speed Railway Bridge Using C-band Sentinel-1 Data. *ISPRS J. Photogramm. Remote Sens.*, 128, 204–211.
- Hülsmeier, C., 1904. Herzian-wave Projecting and Receiving Apparatus Adopted to Indicate or Give Warning of The Presence of a Metallic Body such as A Ship or A Train. *Br. Pat.*, British Patent, 13170.
- Hussain, M., Chen, D., Cheng, A., Wei, H., Stanley, D., 2013. Change Detection from Remotely Sensed Images: from Pixel-based to Object-based Approaches. *ISPRS J. Photogramm. Remote Sens.*, 80, 91–106.
- Judge, T.R., Bryanston-Cross, P.J., 1994. A Review of Phase Unwrapping Techniques in Fringe Analysis. *Opt. Lasers Eng.*, 21(4), 199–239.
- Kampes, B., 2006. *Radar Interferometry - Persistent Scatterer Technique*. Springer, Dordrecht, The Netherlands.
- Koch, K.-R., 1999. *Parameter Estimation and Hypothesis Testing in Linear Models*. Springer, Berlin and Heidelberg, Germany.
- Kvam, P.H., Vidakovic, B., 2007. *Nonparametric Statistics with Applications to Science and Engineering*. Wiley, Hoboken, United States of America.
- Lanari, R., Casu, F., Manzo, M., Zeni, G., Berardino, P., Manunta, M., Pepe, A., 2007. An Overview of The Small Baseline Subset Algorithm: A DInSAR Technique for Surface Deformation Analysis. *Pure Appl. Geophys.*, 164(4), 637–661.
- Lanari, R., Mora, O., Manunta, M., Mallorqui, J.J., Berardino, P., Sansosti, E., 2004. A Small-baseline Approach for Investigating Deformations on Full-resolution Differential SAR Interferograms. *IEEE Trans. Geosci. Remote Sens.*, 42(7), 1377–1386.
- Lee, J.-S., 1981a. Speckle Analysis and Smoothing of Synthetic Aperture Radar Images. *Comput. Graph. Image Process.*, 17(1), 24–32.

- Lee, J.-S., 1981b. Refined Filtering of Image Noise Using Local Statistics. *Comput. Graph. Image Process.*, 15(4), 380–389.
- Lee, J.S., Jurkevich, L., Dewaele, P., Wambacq, P., Oosterlinck, A., 1994. Speckle Filtering of Synthetic Aperture Radar Images: A Review. *Remote Sens. Rev.*, 8(4), 313–340.
- López-Quiroz, P., Doin, M.-P., Tupin, F., Briole, P., Nicolas, J.-M., 2009. Time Series Analysis of Mexico City Subsidence Constrained by Radar Interferometry. *J. Appl. Geophys.*, 69(1), 1–15.
- Lv, X., Yazici, B., Zeghal, M., Bennett, V., Abdoun, T., 2014. Joint-Scatterer Processing for Time-Series InSAR. *IEEE Trans. Geosci. Remote Sens.*, 52(11), 7205–7221.
- Lyons, S., Sandwell, D., 2003. Fault Creep along The Southern San Andreas from Interferometric Synthetic Aperture Radar, Permanent Scatterers, and Stacking. *J. Geophys. Res.*, 108(B1).
- Ma, P., Lin, H., 2016. Robust Detection of Single and Double Persistent Scatterers in Urban Built Environments. *IEEE Trans. Geosci. Remote Sens.*, 54(4), 2124–2139.
- Marin, C., Bovolo, F., Bruzzone, L., 2015. Building Change Detection in Multitemporal Very High Resolution SAR Images. *IEEE Trans. Geosci. Remote Sens.*, 53(5), 2664–2682.
- Massonnet, D., Briole, P., Arnaud, A., 1995. Deflation of Mount Etna Monitored by Spaceborne Radar Interferometry. *Nature*, 375(6532), 567–570.
- Massonnet, D., Feigl, K.L., 1998. Radar Interferometry and Its Application to Changes in The Earth's Surface. *Rev. Geophys.*, 36(4), 441–500.
- Massonnet, D., Holzer, T., Vadon, H., 1997. Land Subsidence Caused by The East Mesa Geothermal Field, California, Observed Using SAR Interferometry. *Geophys. Res. Lett.*, 24(8), 901–904.
- Massonnet, D., Rossi, M., Carmona, C., Adragna, F., Peltzer, G., Feigl, K., Rabaute, T., 1993. The Displacement Field of The Landers Earthquake Mapped by Radar Interferometry. *Nature*, 364(6433), 138–142.
- Massonnet, D., Sigmundsson, F., 2000. Remote Sensing of Volcano Deformation by Radar Interferometry from Various Satellites, in: *Remote Sensing of Active Volcanism*. pp. 207–221.
- Matsuoka, M., Yamazaki, F., 2004. Use of Satellite SAR Intensity Imagery for Detecting Building Areas Damaged due to Earthquakes. *Earthq. Spectra*, 20(3), 975–994.
- Mittermayer, J., Wollstadt, S., Prats-Iraola, P., Scheiber, R., 2014. The TerraSAR-X Staring Spotlight Mode Concept. *IEEE Trans. Geosci. Remote Sens.*, 52(6),

- 3695–3706.
- Monserrat, O., Crosetto, M., Cuevas, M., Crippa, B., 2011. The Thermal Expansion Component of Persistent Scatterer Interferometry Observations. *IEEE Geosci. Remote Sens. Lett.*, 8(5), 864–868.
- Mora, O., Mallorqui, J.J., Broquetas, A., 2003. Linear and Nonlinear Terrain Deformation Maps from A Reduced Set of Interferometric SAR Images. *IEEE Trans. Geosci. Remote Sens.*, 41(10), 2243–2253.
- Morishita, Y., Hanssen, R.F., 2015. Deformation Parameter Estimation in Low Coherence Areas Using A Multisatellite InSAR Approach. *IEEE Trans. Geosci. Remote Sens.*, 53(8), 4275–4283.
- Nico, G., Pappalepore, M., Pasquariello, G., Refice, A., Samarelli, S., 2000. Comparison of SAR Amplitude vs. Coherence Flood Detection Methods - A GIS Application. *Int. J. Remote Sens.*, 21(8), 1619–1631.
- Novali, F., Basilico, M., Ferretti, A., Prati, C., Rocca, F., 2004. Advances in Permanent Scatterer Analysis: Semi and Temporary PS, in: *EUSAR 2004*. Berlin, Germany.
- Ó Ruanaidh, J.J.K., Fitzgerald, W.J., 1996. *Numerical Bayesian Methods Applied to Signal Processing, Statistics and Computing*. Springer, New York, United States of America.
- Otsu, N., 1979. A Threshold Selection Method from Gray-Level Histograms. *IEEE Trans. Syst. Man. Cybern.*, 9(1), 62–66.
- Peltzer, G., Rosen, P., 1995. Surface Displacement of The 17 May 1993 Eureka Valley, California, Earthquake Observed by SAR Interferometry. *Science*, 268(5215), 1333–1336.
- Pepe, A., Euillades, L.D., Manunta, M., Lanari, R., 2011. New Advances of The Extended Minimum Cost Flow Phase Unwrapping Algorithm for SBAS-DInSAR Analysis at Full Spatial Resolution. *IEEE Trans. Geosci. Remote Sens.*, 49(10), 4062–4079.
- Pepe, A., Lanari, R., 2006. On The Extension of The Minimum Cost Flow Algorithm for Phase Unwrapping of Multitemporal Differential SAR Interferograms. *IEEE Trans. Geosci. Remote Sens.*, 44(9), 2374–2383.
- Pepe, A., Yang, Y., Manzo, M., Lanari, R., 2015. Improved EMCF-SBAS Processing Chain Based on Advanced Techniques for The Noise-Filtering and Selection of Small Baseline Multi-Look DInSAR Interferograms. *IEEE Trans. Geosci. Remote Sens.*, 53(8), 4394–4417.
- Perissin, D., Ferretti, A., Piccagli, D., Prati, C., Rocca, F., Rucci, A., De Zan, F., 2007. Repeat-pass SAR Interferometry with Partially Coherent Targets, in: *Proceedings of Fringe*. Frascati, Italy.

- Perissin, D., Wang, T., 2011. Time-series InSAR Applications over Urban Areas in China. *IEEE J. Sel. Top. Appl. Earth Obs. Remote Sens.*, 4(1), 92–100.
- Perissin, D., Wang, T., 2012. Repeat-pass SAR Interferometry with Partially Coherent Targets. *IEEE Trans. Geosci. Remote Sens.*, 50(1), 271–280.
- Porcello, L.J., Massey, N.G., Innes, R.B., Marks, J.M., 1976. Speckle Reduction in Synthetic-aperture Radars. *J. Opt. Soc. Am.*, 66(11), 1305–1311.
- Poulain, V., Inglada, J., Spigai, M., Tourneret, J.-Y., Marthon, P., 2011. High-resolution Optical and SAR Image Fusion for Building Database Updating. *IEEE Trans. Geosci. Remote Sens.*, 49(8), 2900–2910.
- Preiss, M., Stacy, N.J.S., 2006. *Coherent Change Detection: Theoretical Description and Experimental Results*. Edinburgh, Australia.
- Press, W.H., Flannery, B.P., Teukolsky, S.A., Vetterling, W.T., 1988. *Numerical Recipes in C: The Art of Scientific Computing*. Cambridge University Press, Cambridge, United Kingdom.
- Raucoules, D., Maisons, C., Carnec, C., Le Mouelic, S., King, C., Hosford, S., 2003. Monitoring of Slow Ground Deformation by ERS Radar Interferometry on The Vauvert Salt Mine (France): Comparison with Ground-based Measurement. *Remote Sens. Environ.*, 88(4), 468–478.
- Rignot, E.J., Gogineni, S.P., Krabill, W.B., Ekholm, S., 1997. North and Northeast Greenland Ice Discharge from Satellite Radar Interferometry. *Science*, 276(5314), 934–937.
- Rignot, E.J.M., van Zyl, J.J., 1993. Change Detection Techniques for ERS-1 SAR Data. *IEEE Trans. Geosci. Remote Sens.*, 31(4), 896–906.
- Rocca, F., 2007. Modeling Interferogram Stacks. *IEEE Trans. Geosci. Remote Sens.*, 45(10), 3289–3299.
- Rosen, P.A., Hensley, S., Joughin, I.R., Li, F.K., Madsen, S.N., Rodriguez, E., Goldstein, R.M., 2000. *Synthetic Aperture Radar Interferometry*. *Proc. IEEE*, 88(3), 333–382.
- Sansosti, E., Berardino, P., Bonano, M., Calò, F., Castaldo, R., Casu, F., Manunta, M., Manzo, M., Pepe, A., Pepe, S., Solaro, G., Tizzani, P., Zeni, G., Lanari, R., 2014. How Second Generation SAR Systems Are Impacting The Analysis of Ground Deformation. *Int. J. Appl. Earth Obs. Geoinf.*, 28, 1–11.
- Schack, L., Soergel, U., 2014. Exploiting Regular Patterns to Group Persistent Scatterers in Urban Areas. *IEEE J. Sel. Top. Appl. Earth Obs. Remote Sens.*, 7(10), 4177–4183.
- Schmidt, D.A., Bürgmann, R., 2003. Time-dependent Land Uplift and Subsidence in The Santa Clara Valley, California, from a Large Interferometric Synthetic Aperture Radar Data Set. *J. Geophys. Res.*, 108(B9), a.

- Schreier, G., 1993. SAR Geocoding : Data and Systems. Wichmann, Karlsruhe, Germany.
- Schunert, A., Soergel, U., 2012. Grouping of Persistent Scatterers in High-resolution SAR Data of Urban Scenes. *ISPRS J. Photogramm. Remote Sens.*, 73, 80–88.
- Schunert, A., Soergel, U., 2016. Assignment of Persistent Scatterers to Buildings. *IEEE Trans. Geosci. Remote Sens.*, 54(6), 3116–3127.
- Soergel, U., 2010. Radar Remote Sensing of Urban Areas. Springer, The Netherlands.
- Soergel, U., Schulz, K., Thoennessen, U., Stilla, U., 2005. Integration of 3D Data in SAR Mission Planning and Image Interpretation in Urban Areas. *Inf. Fusion*, 6(4), 301–310.
- Soergel, U., Thoennessen, U., Brenner, A., Stilla, U., 2006. High-resolution SAR Data: New Opportunities and Challenges for The Analysis of Urban Areas. *IEE Proc. - Radar, Sonar Navig.*, 153(3), 294–300.
- Stephens, M., 1970. Use of the Kolmogorov-Smirnov, Cramér-Von Mises and Related Statistics without Extensive Tables. *J. R. Stat. Soc. Ser. B*, 32(1), 115–122.
- Stilla, U., Soergel, U., Thoennessen, U., 2003. Potential and Limits of InSAR Data for Building Reconstruction in Built-up Areas. *ISPRS J. Photogramm. Remote Sens.*, 58(1–2), 113–123.
- Tao, J., Auer, S., Reinartz, P., 2012. Detecting Changes between A DSM and A High Resolution SAR image with The Support of Simulation Based Separation of Urban Scenes, in: *EUSAR 2012*. Nuremberg, Germany.
- Taubenböck, H., Esch, T., Felbier, A., Wiesner, M., Roth, A., Dech, S., 2012. Monitoring Urbanization in Mega Cities from Space. *Remote Sens. Environ.*, 117, 162–176.
- Teunissen, P.J.G., 2000. Testing Theory: An Introduction. VSSD, Delft, The Netherlands.
- Touzi, R., Lopes, A., Bousquet, P., 1988. A Statistical and Geometrical Edge Detector for SAR Images. *IEEE Trans. Geosci. Remote Sens.*, 26(6), 764–773.
- Touzi, R., Lopes, A., Bruniquel, J., Vachon, P.W., 1999. Coherence Estimation for SAR Imagery. *IEEE Trans. Geosci. Remote Sens.*, 37(1), 135–149.
- Wang, Y., Zhu, X.X., Bamler, R., 2012. Retrieval of Phase History Parameters from Distributed Scatterers in Urban Areas Using Very High Resolution SAR Data. *ISPRS J. Photogramm. Remote Sens.*, 73, 89–99.
- Wegmuller, U., Walter, D., Spreckels, V., Werner, C.L., 2010. Nonuniform Ground Motion Monitoring with TerraSAR-X Persistent Scatterer Interferometry. *IEEE Trans. Geosci. Remote Sens.*, 48(2), 895–904.
- Werner, C., Wegmuller, U., Strozzi, T., Wiesmann, A., 2003. Interferometric Point Target Analysis for Deformation Mapping, in: *2003 IEEE International*

- Geoscience and Remote Sensing Symposium. IEEE, Toulouse, France, pp. 4362–4364.
- Xia, Z.-G., Henderson, F.M., 1997. Understanding The Relationships between Radar Response Patterns and The Bio- and Geophysical Parameters of Urban Areas. *IEEE Trans. Geosci. Remote Sens.*, 35(1), 93–101.
- Zebker, H.A., Goldstein, R.M., 1986. Topographic Mapping from Interferometric Synthetic Aperture Radar Observations. *J. Geophys. Res.*, 91(B5), 4993–4999.
- Zebker, H.A., Lu, Y., 1998. Phase Unwrapping Algorithms for Radar Interferometry: Residue-cut, Least-squares, and Synthesis Algorithms. *J. Opt. Soc. Am. A*, 15(3), 586–598.
- Zebker, H.A., Rosen, P.A., Goldstein, R.M., Gabriel, A., Werner, C.L., 1994. On The Derivation of Coseismic Displacement Fields Using Differential Radar Interferometry: The Landers Earthquake. *J. Geophys. Res.*, 99(B10), 19617–19634.
- Zebker, H.A., Villasenor, J., 1992. Decorrelation in Interferometric Radar Echoes. *IEEE Trans. Geosci. Remote Sens.*, 30(5), 950–959.
- Zhang, R., Liu, G., Li, T., Huang, L., Yu, B., Chen, Q., Li, Z., 2014. An Integrated Model for Extracting Surface Deformation Components by PSI Time Series. *IEEE Geosci. Remote Sens. Lett.*, 11(2), 544–548.

Acknowledgement

I would like to appreciate Prof. Uwe Sörgel for his support during my Ph.D. program. He has always encouraged and inspired me as a senior mentor. I also express my gratitude to Prof. Xiaoxiang Zhu. With her help, this thesis has been remarkably improved. Of course, many thanks to our IFP team not only for their cooperation but also the joy with their company. During this time I have made lots of good friends, which become parts of my life. Among them, I am grateful especially to Dr. Damian Bargiel and Dr. Lukas Schack for their proofreading and consultation. Finally, there are no words to express my appreciation to my parents and brother. Their loves and supports are all attributed to my achievements.

List of acronyms

APS	Atmospheric Phase Screen
bd	Break Date
DBC	Disappearing Big Change
DEM	Digital Elevation Model
DInSAR	Differential Interferometric Synthetic Aperture Radar
DS	Distributed Scatterers
EBC	Emerging Big Change
EMCF	Extended Minimum Cost Flow
InSAR	Interferometric Synthetic Aperture Radar
LoS	Light-of-Sight
MCF	Minimum Cost Flow
MInTS	Multiscale InSAR Time Series
MLE	Maximum Likelihood Estimation
PS	Persistent Scatterer
PSI	Persistent Scatterer Interferometry
PSP	Persistent Scatterer Pairs
QPS	Quasi-PS
radar	RAdio Detection And Ranging
RAR	Real Aperture Radar
SAR	Synthetic Aperture Radar
SBAS	Small BAseLine Subset
SLR	Side-Looking Radar
SPN	Stable Point Network
StaMPS	Stanford Method for Persistent Scatterers
STUN	SpaioTemporal Unwrapping Network
SVD	Singular Value Decomposition
V	Void

List of symbols

N	number of SAR images
M	number of interferograms
θ	look angle
ρ_a	azimuth resolution
ρ_{sr}	slant-range resolution
ρ_{gr}	ground-range resolution
L_a	antenna length
c	speed of light
τ	pulse length
s	SAR signal
A	amplitude
I	intensity
ϕ	phase
φ	interferometric phase
φ'	differential interferometric phase
H	height
Δh	residual topographic error
v	velocity
R	slant-range
ΔR	slant-range difference
$\Delta R'$	light-of-sight motion
T	time
B	base line
B_T	temporal baseline
B_{\perp}	perpendicular baseline
α	tilt angle
γ	complex coherence
$ \gamma $	coherence
γ_T	temporal coherence
λ	wavelength
x	pixel index
int	interferogram index
CI	change index
D_A	amplitude dispersion
μ	mean

σ standard deviation